Theory and Development of Near-field Plates

by

Seyedmohammadreza Faghih Imani

A dissertation submitted in partial fulfillment
of the requirements for the degree of
Doctor of Philosophy
(Electrical Engineering)
in The University of Michigan
2013

Doctoral Committee:

Associate Professor Anthony Grbic, Chair
Assistant Professor Mona Jarrahi
Professor Roberto D. Merlin
Professor Eric Michielssen

To my parents,

Forough Azam Sadri and Seyed Rasoul Faghih Imani

ACKNOWLEDGEMENTS

I would never have been able to accomplish this work without the help and support of my beloved family, especially my mom and dad, who have been the source of consolation and relief throughout my education.

I would like to thank my advisor, Professor Anthony Grbic, who has guided me through my research endeavors over the last six years. Working with him has been an extremely rewarding experience in both academic and social aspects. As a person starting his research career, I am greatly indebted to Professor Anthony Grbic for what he has taught me over the course of my doctoral studies

I also want to thank my thesis committee, Professor Roberto Merlin, Professor Eric Michielssen, and Professor Mona Jarrahi. It has been an honor and privilege to have you on my committee and discuss my research with you. Our fruitful discussions have been and will be helpful in my future research efforts.

I would like to extend my gratitude to my teachers at the University of Michigan: Professor Kamal Sarabandi, Professor Amir Mortezawi, Professor Ted Norris, and Professor Almantas Galavanaskus. Your training equipped me with the necessary knowledge and skills to pursue my research projects.

I also want to acknowledge University of Michigan staff who provided a friendly and welcoming environment. Especially, Karla Johnson, Michelle Chapman, Karen Liska, and Beth Stalnaker who have been of great assistance over the last six years.

I also want to dedicate special thanks to my precious friends: Amit Patel, Vahed Qazvinian, Ali Besharatian, Kara Moser, Jennifer Klein, Farhad Bayatpur, Ahmad

Beirami, Pooyan Amini, Meisam Razaviyayn, Ali Moayedi, and Pedram Radmanesh. You have been a wonderful source of support and encouragement for me.

Finally, I would like to thank all my friends and former and current colleagues at the University of Michigan: Morteza Nick, Alireza Tabatabayinejad, Danial Ehyayi, Mehrnoush Vahidpur, Shahrzad Naraghi, Javid Moraveji, Mauro Ettorre, Mojtaba Dehmolaeian, Shima Hossein Abadi, Hadi Katebi, Armin Alaghi, Elnaz Ansari, Payam Mirshams, Hassan Ghaed, Siamak Davarani, Hamed Firouzi, Aria Sahebi, Mahmoud Barangi, Farhad Shirani, Hamidreza Tavafoghi, Hamid Nejati, Fikadu Dagefu, Gurkan Gok, Abdulkadir Yucel, Seyit Sis, Onur Baker, Victor Lee, Young Jun Song, Hatim Bokhari, Luis Gomez, Scott Rudolph, Carl Pfeiffer, Brian Tierney, Adam Weiss, Lai Wei, Erin Thomas, Erio Gandini, Lei Jiang, Brett Kuprel, Jason Heeble, Yuri Goykhman, Ruzbeh Akbar, Felipe Valdes, Sergio Doque, Michael Benson, Pelumi Osaba, Adel Elsherbini, Sahar Nouri, Roshan Najafi, Mahta Mousavi, Azadeh Ansari, Parinaz Naghizade, Rahman Sabahi, Mani Kashanian Fard, Meisam Moallem, Armin Jam, Morteza Sheikhsofla, Mohammadreza Hashemi, Ju Seop Lee, Xueyang Duan, Yohan Kim, Momchil Mihnev, Walid Alomar, and Jackie Vitaz.

TABLE OF CONTENTS

LIST OF FIGURES

xiii

LIST OF TABLES

ABSTRACT

Theory and Development of Near-field Plates

by

Mohammadreza F. Imani

Chair: Anthony Grbic

The widespread use of the electromagnetic near field, in applications ranging from high resolution imaging devices to wireless power transfer systems, has called for focusing devices with higher resolutions and larger focal lengths. This demand, however, faces a major obstacle: the diffraction limit. Due to this limit, subwavelength resolutions are only possible at near-field distances.

A novel solution is proposed for overcoming the diffraction limit: near-field plates (NFPs). NFPs are non-periodically patterned surfaces that can form desired subwavelength patterns at specified near-field distances. They are simple to fabricate, robust to inherent losses, and allow the near field pattern to be stipulated. Given these advantages, they show great promise as a simple and effective method for tailoring the electromagnetic near field. In this thesis, the first reported NFP is introduced and its operation is analytically studied. The NFP concept is then advanced through several phases, addressing a major issue in each phase. NFPs suitable for practical applications are introduced, and their design and operation are described. Their ability to tailor the electromagnetic near field is verified through full-wave simulations and experiments. Finally, application areas of NFPs such as near-field probing and

imaging, biomedical devices, and wireless power transfer systems are discussed.

CHAPTER I

Introduction

1.1 Background

Throughout history, humans have relied on their vision to observe the world around them. Early humans drew stories on cave walls to transfer their knowledge to others. In many civilizations, the movement of sun and moon were observed to develop calendars. However, human vision is limited and cannot see very small or very far. As a result, knowledge of our surroundings was limited and even incorrect until imaging systems were developed: apparatuses that enabled us to see beyond the limits of our eyesight. The enhanced vision revolutionized our perception of the world and triggered many momentous scientific breakthroughs. Reliable telescopes put fictions about outer space to rest and paved the way to our current understanding. Microbes and their role in the transmission of disease were not known until the invention of the microscope. Microscopes also led to the discovery of cells, which revolutionized the science of biology. The advancement of science and technology, in return, resulted in demands for imaging systems with higher quality and improved resolutions. Hence, the quest to see smaller details or objects farther away has drawn strong interest from scientists and engineers for centuries.

The primary component of early imaging systems was a curved surface, such as a lens or a mirror. Curved surfaces can converge or diverge electromagnetic waves

radiated by an object to form an image. The "tailoring" capability of lenses and mirrors was utilized to develop devices such as microscopes and telescopes. In fact, lenses and mirrors are still the backbone of many imaging systems. However, the maximum resolution that can be obtained using a lens or mirror was known to be limited. This fundamental limit is referred to as the "diffraction limit", and was first formulated by Abbe:

$$d = \frac{\lambda}{2\text{NA}} \tag{1.1}$$

where d is the resolution, λ is the operating wavelength, and NA is the numerical aperture. This equation describes the maximum resolution of an imaging system at a given wavelength of operation. According to this equation, the only method to achieve higher resolution is either by operating at shorter wavelengths or increasing the numerical aperture. However, shorter wavelengths (higher frequencies) of operation were not always desired or simple to achieve. The numerical aperture is bounded by the refractive index, n, of the medium, which is usually air ($n = 1$). Therefore, the diffraction limit was a major obstacle to visualizing finer details. As a result, methods to overcome the diffraction limit were sought.

The physics behind Abbe's limit is simple and can be explained by examining the configuration of imaging systems. For example, consider the simplified schematic of an imaging system shown in Figure 1.1. In this configuration, a lens collects the radiation of an object to form a magnified image of it. In such imaging schemes, the distance between the imaging component (lens) and the object are large compared to the wavelength. In other words, they are in the far-field region of each other. The object under test emits both propagating and evanescent electromagnetic waves. However, the lens can only collect the propagating spectrum since the evanescent spectrum decays rapidly with the distance. Therefore, the image obtained through a far-field imaging system, such as the one shown in Figure 1.1, only contains the propagating spectrum. However, the subwavelength details of the object are only

carried by the evanescent spectrum. As a result, the maximum resolution possible with conventional imaging systems was limited. On the other hand, this simple explanation suggests that higher resolutions are possible if the imaging device could capture the evanescent spectrum.
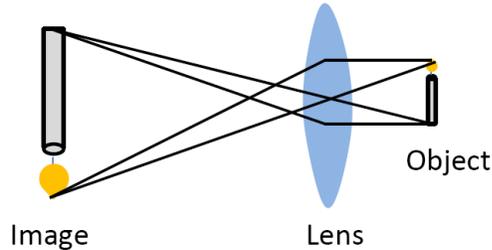
Figure 1.1: A simplified schematic of an imaging system.

The importance of the evanescent spectrum in imaging was first noted by Synge [1], where he proposed detecting the near field to obtain resolutions beyond the diffraction limit. He went on to show that probing the near field (evanescent fields) of an object amounted to tapping into the object's subwavelength details. Nearly fifty years after Synge's proposal, Ash and Nicholls experimentally verified super-resolved near-field imaging in 1972 [2]. Since then, high resolution near-field imaging systems have been a reality (for example, refer to [3] for a detailed review).

Synge proposed a practical method for detecting evanescent spectrum. This proposition paved the way for a myriad of other near-field devices. High density data storage, biomedical targeting instruments, radio frequency identification (RF-ID) devices, and wireless power transfer systems [4] are all examples of devices that rely on the evanescent spectrum. In high density data storage devices, a subwavelength electromagnetic spot is used to store or retrieve data. Similarly, a highly confined electromagnetic field spot is used in biomedical targeting devices to stimulate cells (such as transcranial magnetic stimulation [5]) or create a hyperthermal effect. Such subwavelength beam dimensions are only plausible in the near field, where the evanes-

cent spectrum is comparable to or dominant over propagating spectrum. In RF-ID devices or wireless power transfer devices, the evanescent spectrum is used to couple energy between two devices with high efficiency.

Today, the evanescent spectrum is widely employed in scientific and industrial applications. Its widespread use has in turn created a demand for improvements to existing near-field devices. Increasing the resolution of near-field imaging systems or extending the range of wireless power transfer systems are some obvious examples. Since the evanescent spectrum, which is vital to the performance of near-field devices, decays with distance, the primary strategy to improve performance is to reduce the operating distance. However, such operating schemes can be costly and infeasible in many applications. For example, an imaging probe placed too close to a biomedical sample can be invasive and damaging to the sample and experimental results. Hence, a method to tailor the electromagnetic near field to obtain desired resolutions at specified distances is highly sought after.

1.2 Motivation

In 2000, Pendry introduced the perfect lens, a lens capable of overcoming the diffraction limit, and obtaining subwavelength resolutions at extended near-field focal lengths [6]. Pendry showed that a planar slab of negative refractive index metamaterial can manipulate the near field in such a way that it achieves perfect imaging, i.e., a perfect reconstruction of the source's near and far field. He also went on to show that the P-polarized near field (evanescent field) could be focused with only a negative permittivity slab. Since that time, negative refractive index metamaterials have attracted strong interest. The experimental verification of negative refraction [7] and subwavelength focusing using negative refractive index [8], negative permittivity [9, 10], and negative permeability slabs [11] have demonstrated that near-field lenses are in fact a reality.

Metamaterial superlenses provided a dramatically different approach to overcoming the diffraction limit and achieving subwavelength resolutions. Prior to their introduction, the only option was to go extremely close to the sample being imaged using subwavelength apertures. Metamaterial superlenses enhance the evanescent spectrum to compensate for its fast decay, thus paving a new path for engineering the electromagnetic near field. Unfortunately, the performance of the proposed metamaterial superlenses were limited in practice. They suffered from inherent losses, a narrow operating frequency range, or their dependency on a particular polarization. Most recently, S. Rudolph and A. Grbic experimentally demonstrated a wideband polarization-independent volumetric superlens with robust performance in the presence of practical losses [12]. Despite addressing the practical issues limiting previous metamaterial superlenses, this structure was three dimensional and challenging to fabricate. Therefore, the quest to develop a metamaterial structure suitable for practical applications remained.

Metamaterial superlenses also inspired an alternative method for focusing electromagnetic waves to subwavelength resolutions [13]. In this work, R. Merlin proposed a general class of aperture field distributions which can form a subwavelength focus at a prescribed focal plane in the aperture's reactive near field. This new approach to subwavelength focusing relies on patterned (grating-like) planar structures to produce the aperture fields needed to achieve a desired subwavelength focus. These planar structures have been referred to as near-field plates (NFP) [14–16] and can focus electromagnetic radiation to spots or lines of arbitrarily small subwavelength size. Moreover, they can be tailored to produce focal patterns of various shapes and symmetries.

In [14], specific structures and a systematic design procedure for NFPs was described. It was shown that NFPs could be implemented as completely passive structures composed of inductive and capacitive elements. As an example, a microwave

realization of a NFP that focuses the field of a plane wave to a 1-dimensional (1-D) subwavelength focal pattern was reported in [14]. Full-wave electromagnetic simulations (Method of Moments) were presented that clearly demonstrated the plate's ability to overcome the diffraction limit. The effect of loss on the performance of NFPs was also discussed and it was shown that losses have a minimal effect on NFP performance.

The first experimental NFP was presented in [15, 16]. This plate consisted of an array of interdigitated capacitors designed to produce a subwavelength focal pattern. It was experimentally shown to focus 1.027 GHz microwave radiation emanating from an S-polarized cylindrical source to a focus with full width at half maximum (FWHM) of $\lambda/18$. This experimental demonstration verified the radiationless focusing approach and the NFP design procedure.

While NFPs were originally inspired by metamaterial superlenses, they provided a number of advantages over metamaterial superlenses. Superlenses were periodic bulk structures, while NFPs were non-periodic surfaces or arrays. As a result, NFPs were much simpler to fabricate. Furthermore, NFPs allowed one to stipulate the desired near-field pattern. They were also shown to be robust to practical losses. Given these advantages, NFPs show great promise for tailoring the electromagnetic near field in practice.

In order to employ NFPs in practical applications, several major improvements were still needed. The initial NFP configurations were designed for plane wave or cylindrical illuminations. In many applications, a waveguide excitation is preferred. Furthermore, the existing NFPs were only able to produce one-dimensional focal patterns, while two-dimensional patterns are needed in practice. Finally, the NFP configuration proposed in [14–16] was not simple to integrate with other electronics. Addressing NFPs' practical limitations is the primary topic of this thesis. The ultimate goal is to advance NFPs, so that they can be easily integrated into current

systems such as near-field imaging systems, and improve their performance in terms of resolution, range, or efficiency.

1.3   Outline

In this thesis, NFPs are investigated as practical devices for achieving extreme electromagnetic field confinement. The thesis begins with an introduction of the first NFP and its design and operation. An analytical analysis of NFPs is then presented, which provides an intuitive understanding of their operation. This added insight is utilized to advance the initial NFP to topologies more suitable for practical application. Novel realizations are introduced, and their design and operation are described. The design procedures are verified through full-wave simulations and experiments. Finally, application areas of NFPs are discussed.

The thesis is organized into seven chapters. In Chapter 2, the initial proposal of the NFP concept is briefly reviewed. The procedure for designing NFPs as well as their principle of operation are explained. An analytical description of NFPs is presented that provides insight into their operation [17]. Closed-form expressions for the NFP aperture field, current density, and impedance profile are derived. Characteristic features of a NFP's aperture field and current density are also discussed.

In Chapter 3, an alternative NFP implementation that can be directly fed through a waveguide is developed. This novel NFP, referred to as linearly corrugated NFP, consists of a central slit in a metallic plate surrounded by non-periodic linear corrugations. The structure is fed through its central slit. The non-periodic corrugations are designed to tailor the radiation emanating from the slit to a prescribed subwavelength focus. A design procedure for this structure is presented and verified through full-wave simulation. It is shown that this structure is robust to practical losses and can be impedance matched. Finally, an experimental verification of the linearly corrugated NFP is presented [18].

In Chapter 4, a high resolution near-field probe based on a NFP is explored. The probe consists of non-periodic, concentric corrugations that surround a central coaxial aperture in a metallic surface [19]. This structure, referred to as concentrically corrugated NFP, is fed through the central coaxial aperture and can produce a two-dimensional (2-D) subwavelength focus. A design procedure for this structure is outlined and the structure is thoroughly investigated through full-wave simulation. In addition, experimental results confirming the performance of this NFP are presented [20, 21]. In the experiments, the electric-field focal patterns formed by the NFP are shown to be significantly narrower than those of a conventional probe. In addition, the concentrically corrugated NFP is used as a probe to image two closely spaced dipole sources. The NFP probe achieves images with significantly higher resolution compared to the conventional coaxial probe.

In Chapter 5, the NFPs ability to sculpt the electromagnetic near field is further highlighted by demonstrating a NFP that can generate evanescent Bessel beams [22]. Evanescent Bessel beams are solutions to Maxwell equations which resist diffraction. As a result, they can have a transverse pattern with a subwavelength main beam that is nearly constant over a near-field distance. In this chapter, evanescent Bessel beams and their unique properties are briefly reviewed. A summary of previous methods for generating evanescent Bessel beams and their limitations is presented. A uniform impedance surface is designed and also shown to produce evanescent Bessel beams in full-wave simulation. It is noted that such a structure suffers from edge diffraction and thus has limited performance. In addition, an electrically large uniformly-fed annular slot is theoretically and experimentally shown to produce Bessel beams. However, the proposed structure was relatively large and does not allow for the beamwidth of the Bessel beam to be tailored. In the remainder of this chapter, concentrically corrugated NFPs are investigated as effective, yet simple means for generating evanescent Bessel beams. Their advantages over other methods are also highlighted.

In Chapter 6, a planar NFP that can be fabricated using standard printed circuit board (PCB) technology is presented. Previous NFP realizations were not planar and thus cannot be fabricated using PCB technology. Therefore, planar NFPs are an important step towards our goal to promote NFPs as practical structures that can be integrated with near-field devices to improve their performance. These planar NFPs consist of annular slots on a circular, grounded dielectric slab. They are excited through a coaxial connector. The annular slots are loaded with lumped element impedances, which are chosen to produce a prescribed subwavelength focal pattern. A procedure to design such plates is outlined. The designed plates are studied through full-wave simulation and the generation of desired subwavelength patterns are demonstrated. Several NFPs are fabricated and examined through experiment. It is shown that the experimental near-field patterns are in close agreement with simulation, thereby verifying the proposed design and operation. Furthermore, experimental results confirm the planar NFPs ability to tailor the electromagnetic near field.

In the final chapter, the findings and contributions of this thesis are summarized. Possible application areas of NFPs are described. Finally, future directions of research on NFPs are discussed.

CHAPTER II

Analytical and Numerical Analysis of Near-Field Plates

2.1   Introduction

Using near-field plates (NFPs), or non-periodically modulated surfaces, to obtain subwavelength resolutions is a novel approach to overcoming the diffraction limit. Their principle of operation differs dramatically from earlier methods such as placing small tips in close proximity to a sample [3]. They are also distinct from periodic bulk metamaterial slabs which amplify the evanescent spectrum to overcome the diffraction limit [6]. Given the novelty of NFPs, the goal of this chapter is to provide a detailed introduction to their operation. To do so, we will first review the concept of "radiationless interference" proposed by R. Merlin [13], on which NFPs are based. Subsequently, we will examine the first NFP configuration and its design procedure. In the remainder of the chapter, we will analytical investigate NFPs to gain a more intuitive understanding of their performance.

The design procedure for NFPs, outlined in [14–16], relied on solving an electromagnetic inverse problem through numerical simulation (Method of Moments). Such numerical approaches are sufficient for design purposes, but do not provide insight into the operation of NFPs. Therefore, we opt for an analytical analysis of NFPs

to illustrate their performance. In this analytical treatment, closed-form expressions for the currents excited on a NFP, as well as its impedance profile are derived. In addition, spectral domain representations of the current density and the electric field at the surface of the plate are studied. Both the spatial domain and spectral domain studies are used to highlight the performance of NFPs and their unique features. The analytical investigation also sheds light on the similarities and differences between NFPs and earlier structures such as metamaterial superlenses and antenna arrays.

This chapter is organized as follows. First, radiationless interference as the physical principle behind NFPs is reviewed. The general configuration of NFPs and their design and operation are described. In the remainder of the chapter, a specific near-field configuration is considered. Its step-by-step design procedure is outlined and its performance is analyzed analytically. The plate is assumed to be infinite in width to simplify the analytical treatment. The current density on the plate is found in the spectral domain and inverse Fourier transformed to obtain its spatial dependence, as well as the plate's impedance profile [17]. The analytically derived expressions are then compared to those computed numerically for electrically-wide plates, in order to validate the analytical approach. The results of the analytical investigation are discussed to reveal characteristic features of NFPs.

2.2   Radiationless interference

The idea of focusing electromagnetic fields to dimensions less than the diffraction limit using patterned surfaces was first proposed in [13]. In this work, R. Merlin introduced a general class of aperture fields that converges to a subwavelength focal pattern at a near-field distance away from the aperture. The desired aperture field is realized using a patterned surface. This idea is demonstrated in Figure 2.1 where the aperture is assumed to be at $z = 0$ and the focal plane at $z = L$. The structure is excited from $z < 0$ with an electric field polarized in the x direction. According

to [13], a variety of aperture field distributions ($E_{aper}(y, z = 0)$) can be assigned that result in a subwavelength pattern at $z = L$. For example, consider an aperture distribution of the form:

$$E_{aper}(y, z = 0) = M(y)e^{-jqy} \tag{2.1}$$

where $q \gg k$, k is free space wavenumber, and $M(y)$ is a modulation function. It can be shown that if $M(y)$ has a pole with imaginary part equal to $\pm iL$, then the aperture field given by (2.1) converges to a focus at $z = L$ with resolution given by $2\pi/q$. Since $q \gg k$, the aperture field distribution given by (2.1) is predominantly evanescent (non-radiative). These evanescent components combine constructively and destructively to form the subwavelength focus. As a result, this process of focusing electromagnetic fields, which is based on the interference of evanescent components, has been referred to as "radiationless interference". The required aperture field ($E_{aper}(y, z = 0)$) is realized using an engineered surface which has been referred to as "near-field plate" (NFP).

In radiationless interference, the aperture field interferes in the near field to form a desired subwavelength focal pattern. This process of tailoring the electromagnetic near field is quite unique and distinct from earlier structures. For example, it involves interference of the evanescent components which differs from that of zone plates [23], where traveling waves interfere to form a diffraction-limited focus. It is also distinct from antenna pattern synthesis in which desired patterns are formed in the far-field, where evanescent components are insignificant. Radiationless interference is used to synthesize patterns in the near-field where the evanescent spectrum is dominant. Even though the field exiting a metamaterial superlens, when excited by a subwavelength source, demonstrates properties similar to those of the aperture field in NFPs [13] (for example, both exhibit enhanced evanescent spectrum as shown later in this chapter),
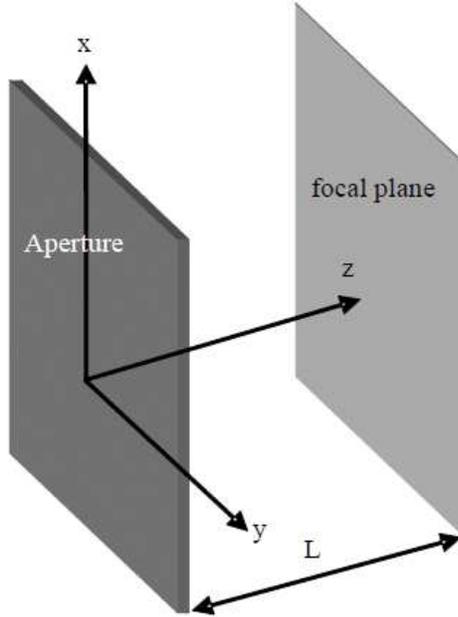
Figure 2.1: A schematic demonstrating "radiationless interference" for overcoming the diffraction limit. The aperture is located at $z = 0$ and the focal plane is at $z = L$. Radiationless interference describe a class of aperture field profile which converges into a subwavelength focal pattern at $z = L$. The aperture field is realized using a patterned surface referred to as near-field plate.

they have notable differences. Metamaterial superlenses are bulky periodic structures that can enhance the evanescent spectrum to overcome its fast decay, while NFPs are non-periodically patterned surfaces or arrays which rely on constructive and destructive interference in the near field to form a desired subwavelength pattern.

A step-by-step procedure for designing NFPs was outlined in [14–16]. This procedure which is based on solving an electromagnetic inverse problem is summarized in Figure 2.2. In the first step, a desired subwavelength focal pattern is selected. The desired focal pattern is then back propagated to the surface of the NFP to obtain the aperture field. In the next step, current densities on the surface of the NFP required to form the aperture field are computed. By taking the ratio of the aperture field and the current densities, the required impedance profile is found. In the last step, this impedance profile is realized using lumped/distributed impedance elements,
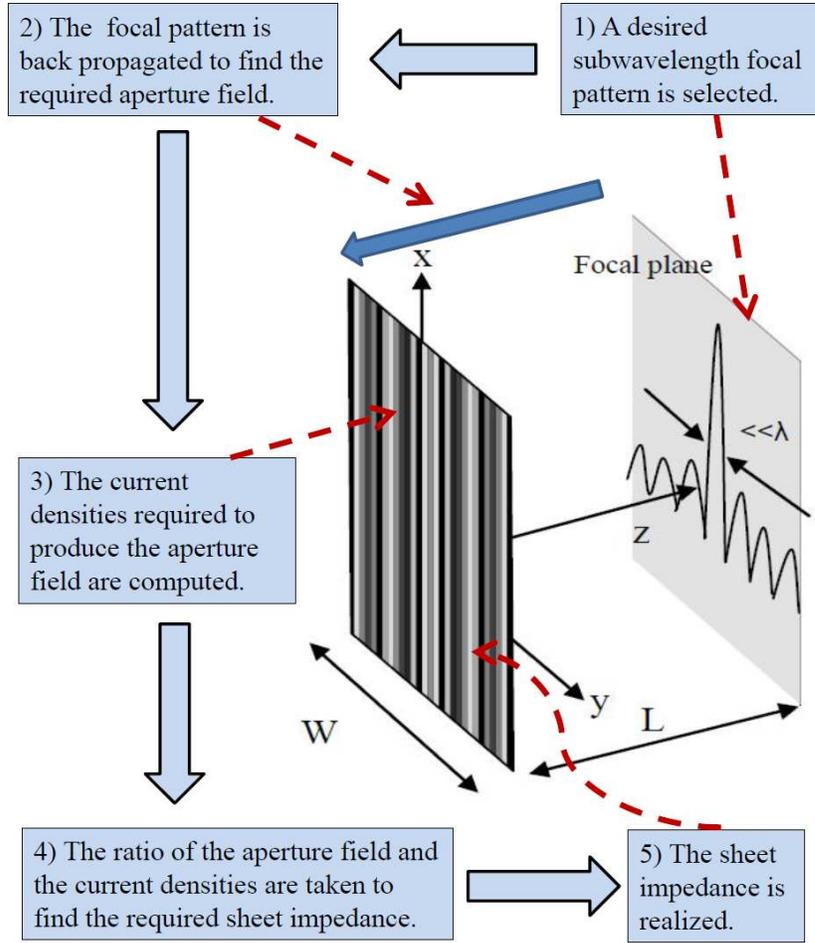
Figure 2.2: A general flowchart for designing NFPs.

corrugated surfaces, or plasmonic nanocircuit elements [24] depending on the NFP configuration and the operating frequency.

Using the outlined procedure, two different NFPs were designed in [14–16]. The plate in [14] was designed to form a subwavelength focus when illuminated by a plane wave while the plate in [15, 16] was designed for a cylindrical (line source) excitation. The later was also fabricated and measured. In the experiment, the fabricated NFP was shown to focus 1.027 GHz microwave radiation, emanating from an x-polarized cylindrical source, to a focus with FWHM $= \lambda/18$, where λ is the free space wavelength. Close agreement between measurement and simulation were demonstrated, thereby verifying the proposed design and operation.

The NFPs presented in [14–16] were designed using a numerical approach. In the next section, we revisit the NFP configurations examined in [14–16]. In contrast to [14–16], we analytically solve for the required current and impedance profile of NFP. The analytical results are then used to explain the operation of the NFP.

2.3   Design Procedure

In this section, we work through the procedure shown in Figure 2.2 to design the NFP configuration in Figure 2.1. Following this procedure, the first step in designing the NFP is to choose a subwavelength focal pattern. In our analytical treatment, we will investigate a NFP that produces a subwavelength focal pattern of the following form,

$$\vec{\mathbf{E}}(y, z = L) = jM|E_{max}|e^{-qL}qL\text{sinc}(qy)\hat{x} \tag{2.2}$$

where $L = \lambda/16$, and $q = 10k$. The operating frequency is $f = 1.0$ GHz. In (2.1), $M = 6$ is a real constant known as the amplification factor, which expresses the focal pattern in terms of the maximum of the incident electric field at the surface of the plate: $|E_{max}| = |E_{inc}(y = 0)|$. These values for L, q, f, and M are assumed throughout this chapter. As explained in [14], the imaginary number j ensures that the plate's surface impedance is primarily reactive. For the assumed parameters, the sinc focal pattern and its spectrum are shown in Figure 2.3. The constant q represents the maximum transverse wavenumber $k_y = q$ that contributes to the focal pattern, and as a result determines its null-to-null beamwidth: $2\pi/q = \lambda/10$. Finally, the plate is assumed to be electrically thin in the z direction ($\lambda \gg$ thickness) so that current densities in the direction normal to the plate can be neglected, and the plate can be modeled as a sheet characterized by a surface impedance $\eta_{sheet}(y)$ [25].

The next step involves finding the currents, $J_x(y)$, on the surface of the plate to generate the desired focal pattern given by (2.2). To do this, we first find the

electric field, $E_{aper}(y)$, that is needed at the surface of the plate to produce the focal pattern [14]. By back-propagating the focal pattern given in (2.2), $E_{aper}(y)$ can be easily obtained through an inverse Fourier transform (IFT):

$$\vec{\mathbf{E}}_{aper}(y) = \mathcal{F}^{-1}\{\vec{\mathbf{E}}_{aper}(k_y)\} = jM|E_{max}|\mathcal{F}^{-1}\{\pi L e^{(-q+jk_z)L}\Pi(k_y, q)\}\hat{x} \qquad (2.3)$$

where the symbol $\mathcal{F}^{-1}$ denotes the IFT with respect to transverse wavenumber k_y; $\Pi(k_y, q)$ is a rectangular function in the spectral domain with amplitude equal to one extending from $k_y = -q$ to $k_y = q$; and k_z is the wavenumber in the z direction defined as:

$$k_z = \begin{cases} \sqrt{k^2 - k_y{}^2} & : \quad k_y{}^2 < k^2 \\ -j\sqrt{k_y{}^2 - k^2} & : \quad k_y{}^2 > k^2. \end{cases} \qquad (2.4)$$

Since the configuration is two dimensional and the electric fields and current densities only have x components, the scalar form of these quantities with a subscript x will be used. Figures 2.4 and 2.5 show the spectral $E_{aper}(k_y)$ and spatial $E_{aper}(y)$ computed in this manner. It should be noted that the numerically computed values for $E_{aper}(y)$ that are used here are different from those in [14], where an approximate analytical expression for $E_{aper}(y)$ was used.

The total electric field, $E_{aper}(y)$, can be related to the current density, $J_x(y)$, using the following integral equation [14]:

$$E_{inc}(y) - \frac{k\eta}{4}\int_{\frac{-W}{2}}^{\frac{W}{2}} J_x(y')H_0^{(2)}(k|y - y'|)dy' = E_{aper}(y) \qquad (2.5)$$

which represents the boundary condition at the plate's surface. The field quantity $E_{inc}(y)$ denotes the electric field incident on the plate from an external source, $H_0^{(2)}$ is the zeroth order Hankel function of the second kind, $\eta = 120\pi\ \Omega$ is the free space wave impedance, and W is the width of the NFP. Substituting (2.3) into (2.5) yields

16

an integral equation which can be solved to find $J_x(y)$.

Once $J_x(y)$ is known, $\eta_{sheet}(y)$ can be computed by simply taking the ratio of $E_{aper}(y)$ to $J_x(y)$:

$$\eta_{sheet}(y) = \frac{E_{aper}(y)}{J_x(y)}. \tag{2.6}$$

In order to find $J_x(y)$ and subsequently $\eta_{sheet}(y)$, (2.5) was solved numerically in [14]. Here, we solve (2.5) analytically, to obtain approximate closed-form expressions for both $J_x(y)$ and $\eta_{sheet}(y)$ [17]. In the analytical treatment, we assume that the plate is infinitely wide, in order to simplify the integral on the left hand side of (2.5) to a convolution:

$$E_{inc}(y) - \frac{k\eta}{4} \int_{-\infty}^{\infty} J_x(y')H_0^{(2)}(k|y-y'|)dy' = jM|E_{max}|\mathcal{F}^{-1}\{\pi Le^{(-q+jk_z)L}\Pi(k_y,q)\}. \tag{2.7}$$

Since the convolution becomes a multiplication in the spectral domain, an expression for $J_x(k_y)$ can be found in the spectral domain, and then inverse Fourier transformed to obtain approximate expressions for $J_x(y)$ and $\eta_{sheet}(y)$. The Fourier transform properties of Hankel and Bessel functions as well as their integral representations [25–27] are utilized in deriving the approximate expressions. Although we consider a NFP under a specific excitation (i.e. cylindrical wave), the analytical approach presented here can be applied to NFPs designed for arbitrary incident waves and desired focal patterns, provided that the Fourier transformation of the incident and desired focal patterns are known.

2.4 Focusing with Infinitely-Wide Near-Field Plates

A NFP is considered that can focus a cylindrical wave to a subwavelength focal pattern given by (2.2). The source of the cylindrical wave will be an x-directed electric line source with current I located at $(y = 0, z = -d)$, as shown in Figure 2.6.

(a) Spectral representation

(b) Spatial representation
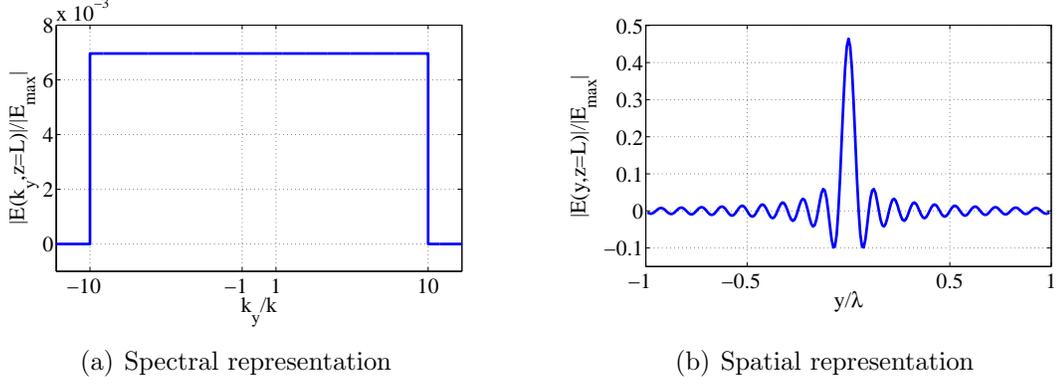
Figure 2.3: Spectral and spatial representation of the electric-field focal pattern ($\vec{\mathbf{E}}$) given by (2.2).

(a) Real part

(b) Imaginary part
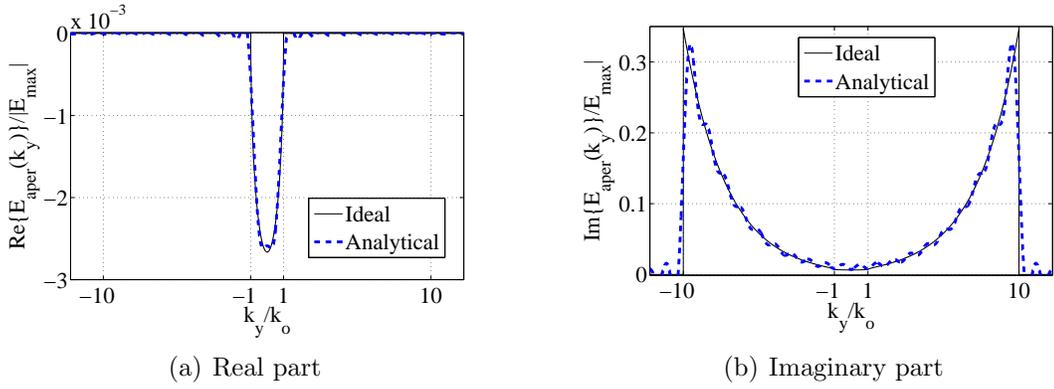
Figure 2.4: Spectral representation of the electric field at the surface of the plate. The solid line represents $E_{aper}(k_y)$ given by (2.3). The dashed line is the spectral domain representation of the approximate $E_{aper}(y)$ given by (2.18). The ripples are due to the truncation of the numerical Fourier transform (Gibb's phenomena).

Throughout this section, it will be assumed that $I = 1$ mA and $d = \lambda/16$. The electric field produced by the line source at the plate's surface is [26]:

$$E_{inc}(y) = -\frac{k\eta I}{4} H_0^{(2)}(k\sqrt{y^2 + d^2}) \tag{2.8}$$
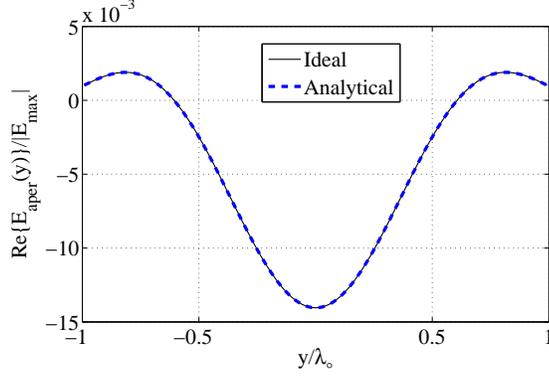
(a) Real part
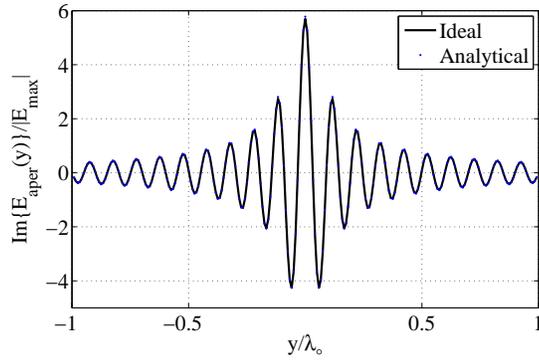
(b) Imaginary part

Figure 2.5: Spatial representation of the electric field at the surface of the plate. The solid line represents $E_{aper}(y)$ given by (2.3) while the dashes in (a) and the dotted line in (b) represents the analytical expression given by (2.18).

Substituting $E_{inc}(y)$ into the integral equation (2.7) yields:

$$-\frac{k\eta I}{4}H_0^{(2)}(k\sqrt{y^2+d^2}) - \frac{k\eta}{4}\int_{-\infty}^{\infty} J_x(y')H_0^{(2)}(k|y-y'|)dy' =$$
$$jM|E_{max}|\mathcal{F}^{-1}\{\pi Le^{(-q+jk_z)L}\Pi(k_y,q)\}. \tag{2.9}$$

This integral equation can be Fourier transformed exactly to obtain its spectral domain counterpart:

$$-\frac{k\eta I}{2}\frac{e^{(-jk_z d)}}{k_z} - \frac{k\eta}{2}\frac{J_x(k_y)}{k_z} = j\pi M|E_{max}|Le^{(-q+jk_z)L}\Pi(k_y,q) \tag{2.10}$$

19
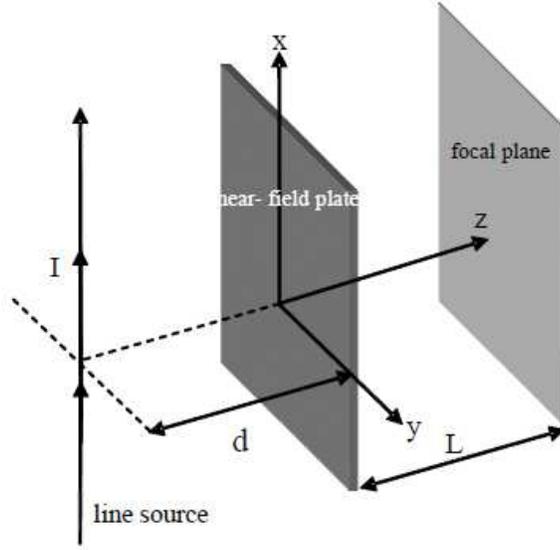
Figure 2.6: A schematic of a near-field plate that is illuminated by a line source at $z = -d$ and forms a desired subwavelength focal pattern at $z = L$.

By rearranging (2.10), the following expression for the spectral domain $J_x(k_y)$ can be obtained:

$$J_x(k_y) = J_x^{inc}(k_y) + J_x^{foc}(k_y) = -Ie^{(-jk_zd)} - \frac{j2\pi LM|E_{max}|e^{(-q+jk_z)L}k_z}{k\eta}\Pi(k_y, q) \quad (2.11)$$

Equation (2.11) reveals that the current density on the NFP consists of two parts. The first term, referred to as $J_x^{inc}(k_y)$, cancels the incident cylindrical wave in the region $z > 0$, while the second term, referred to as $J_x^{foc}(k_y)$, forms the desired focal pattern. The first term, J_x^{inc}, can be inverse Fourier transformed directly:

$$J_x^{inc}(y) = \frac{jkdI}{2\sqrt{d^2 + y^2}}H_1^{(2)}(k\sqrt{d^2 + y^2}) \quad (2.12)$$

The real and imaginary parts of the IFT of $J_x^{foc}(k_y)$ are found separately. The IFT of the imaginary part of $J_x^{foc}(k_y)$ is found exactly, by transforming the propagating

20

spectrum ($|k_y| < k$) of $J_x^{foc}(k_y)$, and retaining its imaginary part:

$$Im\{J_x^{foc}(y)\} = -\frac{\pi ML|E_{max}|ke^{-qL}}{2\eta}[J_0(k\sqrt{y^2 + L^2}) + \frac{y^2 - L^2}{y^2 + L^2}J_2(k\sqrt{y^2 + L^2})]$$

(2.13)

where J_0 and J_2 denote Bessel functions of the first kind. The real part of $J_x^{foc}(y)$ can be derived approximately. Given that the second term of (2.11) increases exponentially as a function of k_y for $|k_y| \gg k$, we apply the following quasi-static approximation,

$$\sqrt{k^2 - k_y^2} \approx -j|k_y|.$$

(2.14)

Under this assumption, the real part of $J_x^{foc}(k_y)$ simplifies to:

$$Re\{J_x^{foc}(k_y)\} \approx \frac{-2\pi LM|E_{max}|e^{(-q+|k_y|)L}|k_y|\Pi(k_y, q)}{k\eta}.$$

(2.15)

The quasi-static approximation is valid when $q \gg k$, in other words for NFPs that focus electromagnetic waves to extremely subwavelength resolutions. It should be noted that the growing nature for $Re\{J_x^{foc}(k_y)\}$ is expected, since it results from restoring/amplifying the evanescent electric field from the focal plane ($z = L$) to the sheet plane ($z = 0$) (see Figure 2.4(b)). Inverse Fourier transforming (2.15), leads to the following approximate expression for the real part of $J_x^{foc}(y)$,

$$Re\{J_x^{foc}(y)\} \approx -\frac{2ML|E_{max}|}{k\eta(L^2 + y^2)}[(Lq - \frac{L^2 - y^2}{L^2 + y^2})\cos(qy) + (yq - \frac{2Ly}{L^2 + y^2})\sin(qy)] \quad (2.16)$$

By combining (2.13) and (2.16), the following expression for $J_x(y)$ is obtained:

$$J_x(y) = \frac{jkdI}{2\sqrt{d^2 + y^2}}H_1^{(2)}(k\sqrt{d^2 + y^2})$$

$$-\frac{j\pi M|E_{max}|Lke^{-qL}}{2\eta}[J_0(k\sqrt{y^2 + L^2}) + \frac{y^2 - L^2}{y^2 + L^2}J_2(k\sqrt{y^2 + L^2})]$$

$$-\frac{2M|E_{max}|L}{k\eta(L^2 + y^2)}[(Lq - \frac{L^2 - y^2}{L^2 + y^2})\cos(qy) + (yq - \frac{2Ly}{L^2 + y^2})\sin(qy)]. \quad (2.17)$$

21

The accuracy of (2.17) can be verified by comparing its numerical Fourier transform, to the exact expression for $J_x(k_y)$ given by (2.11). The two plots are compared in Figure 2.7 and show close agreement. The ripples at the sharp transitions are due to the truncation of the numerical Fourier transform (Gibb's phenomena).

Finally, in order to have a completely analytical expression for η_{sheet}, we must find a closed-form expression for $E_{aper}(y)$. In [14], an analytical expression for $E_{aper}(y)$ was derived which we will use here with a slight modification:

$$E_{aper}(y) = jM|E_{max}|L[\frac{L\cos(qy) + y\sin(qy)}{L^2 + y^2} + 2\pi q e^{(-qL)}(\cos(kL) - 1)\text{sinc}(qy)]$$
$$-\frac{\pi L^2 e^{-qL} kM|E_{max}|}{2\sqrt{L^2 + y^2}} J_1(k\sqrt{L^2 + y^2}). \tag{2.18}$$

The first term is the same as the formula used in [14], and can be derived under the quasi-static approximation (2.14). The second term is a modification factor which is included to match the approximate expression for $E_{aper}(k_y)$ with its exact value at $k_y = 0$. The third term is the real part of $E_{aper}(y)$ resulting from the propagating spectrum ($|k_y| < k$). The analytical expressions for $E_{aper}(k_y)$ and $E_{aper}(y)$ are compared to the numerically computed ones in Figures 2.4 and 2.5, and show close agreement. Now that a closed-form expression for the current density and E_{aper} on the infinitely-wide plate are known, the plate's sheet impedance can be found by substituting (2.17) and (2.18) into (2.6).

Examining (2.17) and (2.18) reveals an interesting feature of the aperture current and field distributions: both equations have the term $(y^2 + L^2)$ in their denominator which translates into a pole at $z = \pm jL$. This is in accordance with the "radiationless interference" concept described earlier.
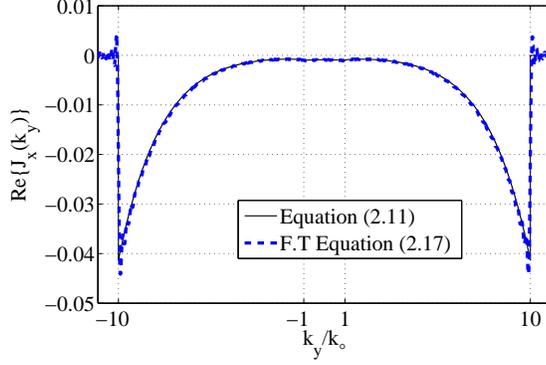
(a) Real part
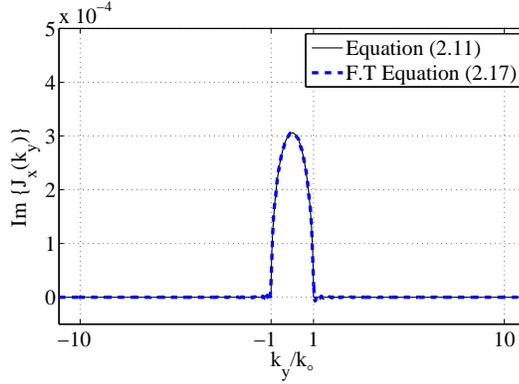
(b) Imaginary part

Figure 2.7: The (a) real and (b) imaginary parts of the spectral representation of the current density $J_x(k_y)$. The solid line represents (2.11) and the dashed line represents the numerical Fourier transform of (2.17).

2.5 Focusing with Finite Near-Field Plates

In the previous section, we derived the current density and impedance for an infinitely-wide NFP that focuses a cylindrical wave to a subwavelength focus (line focus). In this section, we compare the analytical results to numerical results for a finite plate that is $W = 10\lambda$ wide (electrically-wide). The Method of Moments (MoM) is used to simulate the finite-width plate. To be precise, the point matching method [26] is employed with a discretization of $\lambda/40$. The current densities obtained analytically and numerically are depicted in Figure 2.8. They match up well, other than the slight differences near the edges of the finite plate that result from edge
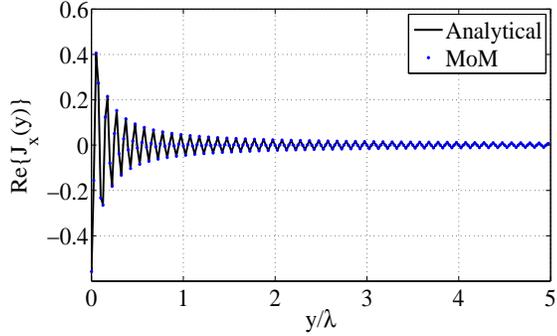
(a) Real part
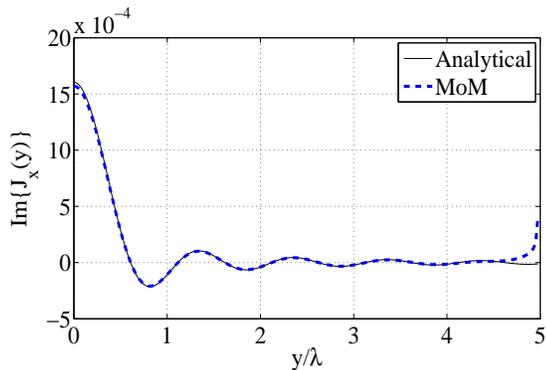
(b) Imaginary part

Figure 2.8: The (a) real and (b) imaginary parts of the current density $J_x(y)$. The solid line represents the analytically derived current density given by (2.17). The dots in (a) and the dashed line in (b) represent the numerically (MoM) computed current density. The current density is only shown on half of the plate since it is symmetric about $y = 0$.

diffraction. It should be noted that the analytical expression for $Re\{J_x(y)\}$ has been derived based on the quasi-static assumption (2.14), which is valid for $q \gg k$. For larger focal spots, or equivalently smaller values of q, it becomes less valid. As a rule of thumb, the quasi-static assumption holds for $q > 3k$.

Figure 2.5 reveals that the aperture field, $E_{aper}(y)$ is predominantly imaginary, while Figure 2.8 shows that the current density, $J_x(y)$, is predominantly real. As a result, the sheet impedance which is the ratio of $E_{aper}(y)$ and $J_x(y)$ is predominantly imaginary (reactive). This fact explains why only the reactive part of sheet impedance, $Im\{\eta_{sheet}(y)\}$, is typically used in the implementation of practical NFPs

24

and the resistive parts are neglected.

Equations (2.17) and (2.18) and Figures 2.4-2.8 illustrate a distinctive feature of the NFPs. The current density and also the electric field on the surface of the NFP exhibits an evanescent spectrum that grows with increasing values of k_y (see Figures 2.4 and 2.7). This evanescent spectrum results in a highly oscillatory spatial domain counterpart (see Figures 2.5 and 2.8 and (2.17)). The evanescent spectrum produced by the NFP is similar to the enhanced evanescent spectrum observed at the exit surface of a negative refractive index metamaterial slab. However, the process by which the evanescent spectrum is enhanced by NFPs is quite different from that for metamaterial slabs. Negative refractive index metamaterials, which are periodic bulk media, enhance the evanescent spectrum through the interaction of surface plasmons, while NFPs are non-periodic planar structures which achieve an enhanced evanescent spectrum through a modulation of their surface reactance. Finally, it should be emphasized that the enhanced evanescent spectrum is required to form the subwavelength focal pattern. The spectrum of the subwavelength focal pattern consists of an extended evanescent spectrum ($|k_y| > |k|$) (see Figure 2.3 (a)). The evanescent spectrum decays as the field propagates to the focal plane with the larger wavenumbers experiencing a higher rate of decay. Therefore, the field at the surface of the NFP must have a growing evanescent spectrum with respect to k_y to compensate for the higher decay rate associated with the larger wavenumbers.

Figure 2.8 reveals another distinctive feature of NFPs: the phase of adjacent elements exhibits rapid variations. This is a characteristic feature of a NFP's current density. It is also reminiscent of the current distribution of superdirective antenna arrays [28]. For both structures, the rapid phase variation between subwavelength-spaced elements increases the ratio of reactive power to that radiated, resulting in a high quality factor, Q [17, 28]. Due to this high Q, both NFPs and superdirective antenna arrays are narrowband (see [28] and [20]). They possess small input

25

resistances and large input reactances, resulting in a significant input impedance mismatch. While NFPs and superdirective antenna arrays share these features, they are also distinct. NFPs produce a prescribed subwavelength near-field pattern, while superdirective antenna arrays produce a far-field pattern that is more directive than that produced by a uniformly excited aperture of the same size. Further, since NFPs operate in the near field and superdirective arrays in the far field, they are designed using entirely different procedures. The NFPs elements are designed through solving an inverse problem step-by-step while in designing superdirective arrays, the elements are optimized to minimize the directivity in the far field [29]. While we demonstrate several different experimental NFPs throughout this thesis, superdirective antenna arrays have remained difficult to realize [30, 31]. One reason is that the tolerances on the magnitude and phase of the element excitations are exceedingly tight, making the feed extremely challenging to implement. Since NFPs operate in the reactive near field, these tolerances are less stringent, simplifying fabrication. Superdirective antennas with passive reflectors or parasitic elements have also been pursued recently. Superdirective reflector arrays and parasitic arrays of electrically-small antennas were designed in [30, 32] and [31], respectively. Much like in NFPs, mutual coupling between elements was exploited to minimize the complexity and loss of the feeding structure. These superdirective arrays, however, are still quite distinct from NFPs. They are composed of resonant elements that generate a superdirective far-field pattern, while the non-periodically varying elements of a NFP are designed to interfere in the near field to produce a desired subwavelength near-field pattern.

The focal patterns, produced by both the analytical and numerical current densities, were computed using the two dimensional free space Green's function [26],

$$E_x(y, z = L) = -\frac{k\eta I}{4} H_0^{(2)}(k\sqrt{y^2 + (d+L)^2}) - \frac{k\eta}{4} \int_{\frac{-W}{2}}^{\frac{W}{2}} J_x(y') H_0^{(2)}(k\sqrt{(y-y')^2 + L^2}) dy'$$

$$(2.19)$$
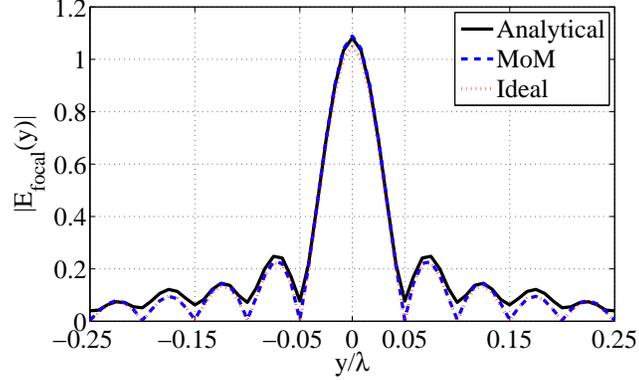
Figure 2.9: Close-up view of the magnitude of electric field at the focal plane. The solid line represents the electric field at the focal plane produced by the analytically derived current density given by (2.17). The dashed line represents the electric field at the focal plane produced by the numerically computed (MoM) current density. The dotted line represents the ideal focal pattern given by (2.2).

and are plotted in Figure 2.9. The focal patterns produced by the analytically derived current density show close agreement with those computed using the MoM. Furthermore, 2-D plots of the vertical electric field computed using the analytically derived and numerically computed current densities (J_x) are shown in Figure 2.10. The incident electric field excites a highly oscillatory field on the surface of the plate ($z = 0$). This highly oscillatory field forms a narrow beam for distances $0 < z < L$ and converges to a subwavelength focus at the focal plane. Beyond the focal plane ($z > L$), the field diverges rapidly. The ability of the NFP to maintain a narrow beam over its focal length ($0 < z < L$) is an intriguing feature, and can be used in many applications to increase operating distance while maintaining resolution. Later in this chapter, and also in chapters 3 and 4, this feature will be demonstrated through experiments and its applications will be discussed in more detail. In Chapters 5 and 6, we will design NFPs that generate evanescent Bessel beams and retain their sunwavelength beamwidth beyond the focal plane. Figure 2.10 also shows reflection from the plate in the region $z < 0$. In the following chapters, methods to decrease reflection from NFPs will be presented.
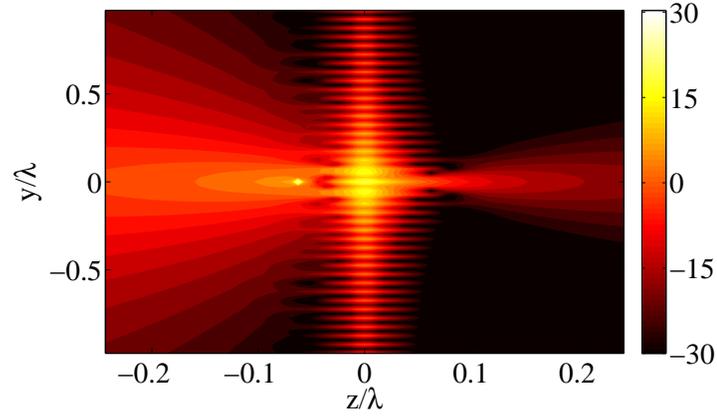
(a) MoM
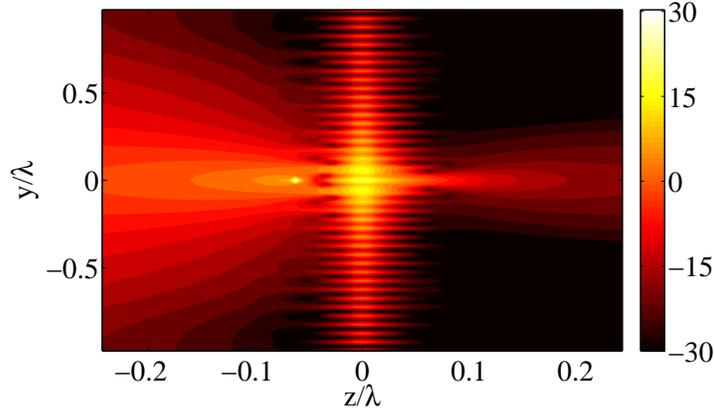
(b) Analytical

Figure 2.10: 2-D plots of the vertical electric field (in dB) surrounding the 10λ NFP. The electric field is computed for the current densities obtained (a) numerically (MoM) and (b) analytically.

Finally, since one of the main goals was to find an expression for the plate's sheet impedance, the reactive sheet impedance resulting from analytical and numerical methods is plotted in Figure 2.11. Impedance values for a 4λ plate are shown, since it is simpler to implement than a plate that is 10λ wide. Given that only the reactive part of the sheet impedance is used in the realization of NFPs [14], the reactive part is only shown. The impedances show good agreement over the majority of the plate with the exception of the plate's edges.
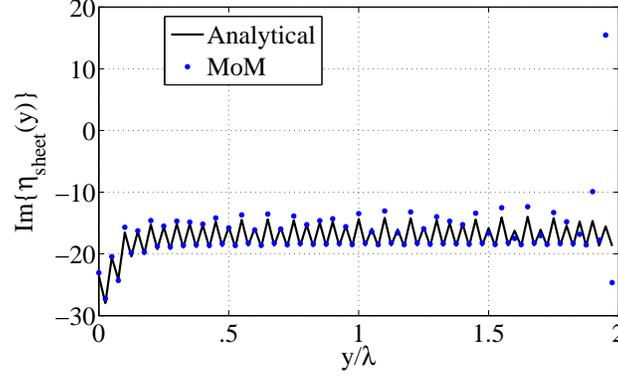
Figure 2.11: The reactive sheet impedance, $Im\{\eta_{sheet}(y)\}$. The solid line represents the analytically derived $Im\{\eta_{sheet}(y)\}$ using (2.17) and (2.18) in (2.6). The dots represent the numerically computed $Im\{\eta_{sheet}(y)\}$ using MoM. The surface impedance is only shown for half of the plate since it is symmetric about $y = 0$.

2.6 Conclusion

In this chapter, we reviewed the concept of "radiationless interference", which forms the basis of operation for NFPs. In addition, a general procedure for designing NFPs was outlined. This procedure was used to design a NFP and its characteristics were described analytically. Closed-form expressions for the induced current density and surface impedance of infinitely-wide NFPs were derived. Further, it was shown that the expressions obtained for infinitely wide plates can be used to approximate the characteristics of finite-width plates. This study revealed that the current density on a NFP can be split into two parts. One part cancels the incident wave on the focus-side of the plate, while the other part produces the desired subwavelength focal pattern. Furthermore, the spatial and spectral representations of the electric field on the NFP were examined and shown to exhibit properties similar to those at the exit face of a metamaterial slab. The intuitive understanding acquired from the analytical discussion in this chapter will be used in the future chapters to further develop the NFP concept and practical NFP designs.

CHAPTER III

Linearly Corrugated Near-Field Plates

3.1 Introduction

In the previous chapter, the concept of "reflectionless interference" on which the operation of near-field plates (NFPs) is based was reviewed. In addition, the design procedure for NFPs and their performance were analytically studied. The NFP of the previous chapter was excited by a cylindrical source and exhibited significant reflection. For many applications, it is more convenient to excite the NFP through a waveguide. A waveguide excitation allows for impedance matching. Therefore, our goal in this chapter is to design a NFP which can be fed through a waveguide.

The NFP described in this chapter is referred to as linearly corrugated NFP. It consists of a slit (parallel plate waveguide) surrounded by equally-spaced grooves with non-periodically varying depths, as shown in Figure 3.1. The grooves act as parasitic elements which shape the radiation from the slit to form a prescribed subwavelength focus. The spacing and the width of the grooves are uniform while the depths of the grooves are varied to shape the desired focal pattern. This non-periodically corrugated NFP should not be confused with periodic, corrugated structures discussed in earlier works [33–44]. In these earlier works, periodic corrugations were used to beam radiation into the far field, in contrast to the non-periodically corrugated NFP presented here which tailors the near field and forms a highly confined electromagnetic

beam. An overview of earlier works and their fundamental differences with corrugated NFPs are presented later in this section.

A linearly corrugated NFP is shown in Figure 3.1. Our goal in this chapter is to demonstrate that such a structure can focus electromagnetic field with subwavelength resolution. A procedure for designing this plate is outlined. Two different examples of corrugated NFPs are developed and their performance is studied in full-wave simulation. In the first example a corrugated NFP is considered that is fed through a central slit in a metallic surface. Full-wave simulation results confirming the plate's ability to form subwavelength focal patterns are reported. It is also demonstrated that the corrugated NFP is robust to practical losses and it can be impedance matched to its waveguide feed.

In the second example, a corrugated NFP with corrugations on both sides is studied. The two sides of the plate are connected by a central slit. One side features a periodic corrugation, which will be referred to as the input corrugation (IC), while the other side features a non-periodic corrugation, which will be referred to as output corrugation (OC). The periodic IC is illuminated by a plane-wave. The IC enhances the transmission of the incident plane wave through the central slit. The non-periodic OC focuses the wave transmitted through the slit to a subwavelength focus. Therefore, the overall function of this corrugated NFP is similar to that of a lens: the IC collects the incident plane-wave radiation, which is then transmitted through the central slit and focused to a subwavelength focus by the non-periodic OC. This corrugated NFP is fabricated and its measurement results are reported. Experimental results confirm that the linearly corrugated NFP produces a focal pattern significantly narrower than that formed by a single slit.

3.1.1 Periodic vs. Non-periodic Corrugations

Over the past few years, there has been growing interest in tailoring far field radiation using periodic corrugations or holes. Much of this interest was initiated by the discovery of extraordinary optical transmission through metallic films perforated with subwavelength holes [33–35]. This work prompted numerous theoretical and experimental studies on light propagation along periodic plasmonic surfaces. It also initiated the investigation of enhanced transmission and beaming through a single subwavelength hole/slit in a metal film surrounded by wavelength-scaled grooves [36–38]. Various geometries were considered including circular holes with concentric grooves and slits flanked by linear arrays of grooves.

From an antenna perspective, the periodic grooves increase the antenna aperture - the area over which the electromagnetic wave is collected or radiated. This enhanced transmission/beaming through a single subwavelength hole was not only observed for periodically patterned plasmonic films, but also patterned conducting surfaces [39–42]. Much like a metallic film at optical frequencies that supports surface plasmons, the patterned conducting surface exhibits an inductive surface impedance that supports bound P-polarized surface waves (spoof surface plasmons) [43]. By periodically perturbing a plasmonic or conventional conducting metal film at a spacing close to guided wavelength, a leaky $n = -1$ spatial harmonic (diffracted beam) can be generated that delocalizes the radiation, in effect creating a leaky-wave antenna that has a directive far-field pattern [42].

The periodically structured surfaces described above enhance transmission and beam radiation into the far field. In contrast, corrugated NFPs possess non-periodic grooves which provide extreme electromagnetic confinement. They manipulate the near field to create a subwavelength focal pattern at a near-field focal distance. It should be noted that, even in [44], where a non-periodic corrugation was considered, the device still operated in the far field and achieved diffraction-limited focusing.
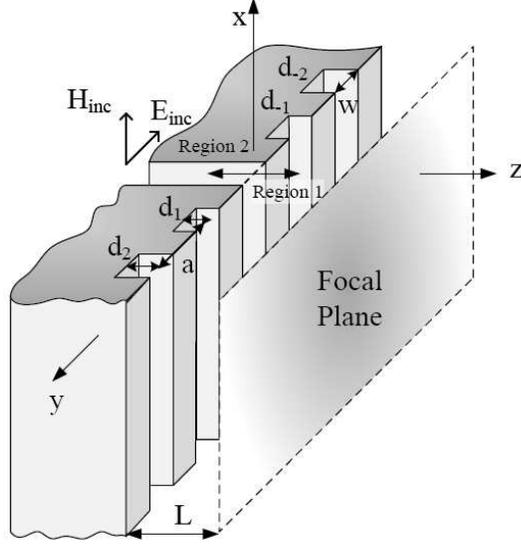
Figure 3.1: A linearly corrugated NFP consisting of a waveguide-fed slit in a non-periodically grooved metallic surface. The grooves have uniform width, w, and are equally spaced at a distance, a, from each other. The depth of each groove is non-periodically varied.

3.2   Design Procedure

We will consider a symmetric linearly corrugated NFP with a finite number of $\pm N$ grooves on each side of the central slit, as shown in Figure 3.1. The grooves have uniform width w and spacing a, while their corresponding depths are non-periodically varied and denoted as d_{-N} to d_N. It is assumed that the grooves are infinite in the x direction and the metallic surface into which the grooves are placed is infinite in the x and y directions. In the design process, the corrugated NFP is first viewed as a waveguide-fed slit in a modulated, non-periodic impedance sheet, as shown in Figure 3.2. In the illustration, the contour plot at the exit face of the slit represents a possible impedance variation realized using non-periodic corrugations. The grooves and central slit (shown in Figure 3.1) are apertures within an infinite metallic surface, and therefore can be modeled as an array of magnetic currents over an infinite ground plane. The magnetic currents are equivalent sources with complex amplitudes equal to the tangential electric field in the central slit and grooves [35,45].
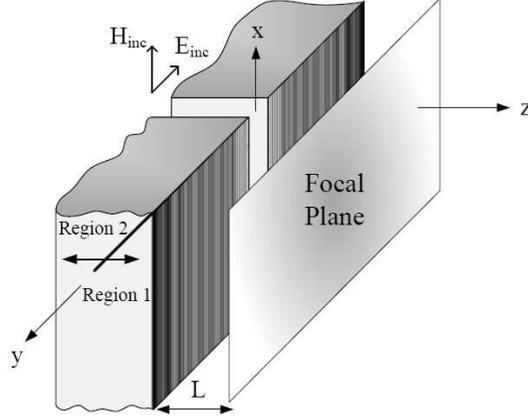
Figure 3.2: A simplified model of the corrugated NFP shown in Figure 3.1. The model consists of a waveguide-fed slit in a non-periodic impedance sheet.

The depicted surface impedance simply represents the ratio of the magnetic current to the tangential magnetic field at $z = 0^+$.

The step-by-step procedure for designing the linearly corrugated NFP is similar to the one described in Figure. 2.2 with few changes. The first step is to find the magnetic current density $M(y)\hat{x}$ on the plate needed to produce the desired focal pattern, in the presence of the excitation (the waveguide-fed slit). The second step involves computing the magnetic field at the surface of the plate, $H_{total} = H(y, z = 0^+)\hat{x}$, resulting from the magnetic current density and the excitation combined. The third step is to calculate the surface impedance required to produce the focal pattern. The surface impedance is calculated by taking the ratio of $M(y)$ to $H(y, z = 0^+)$. The final step is to optimize the depth of the grooves surrounding the central slit, in order to realize this surface impedance profile.

The magnetic current density on the plate needed to produce the desired focal pattern $H_{focal}(y) = H(y, z = L)$ can be found by solving an integral equation that relates the incident magnetic field H_{inc}, $M(y)$, and $H_{focal}(y)$. The electromagnetic boundary value problem can be divided into two regions: region 1 representing the unbounded space $z > 0$, and region 2 representing the region within the waveguide feed. Using the aperture formulation for TM scattering [45], equivalent electromag-

netic problems for the two regions can be written, that are connected through the continuity of tangential magnetic and electric field through the central slit. The equivalent problem for region 1 involves a magnetic current density $2M(y)$ radiating in free space to produce the desired focal pattern $H_{focal}(y)$. It is governed by the following integral equation,

$$\frac{-\omega\epsilon_0}{2}\int_{-W/2}^{W/2}M(y')H_0^{(2)}(k\sqrt{(y-y')^2+L^2})dy' = H_{focal}(y), \tag{3.1}$$

where W is the total width of the corrugated NFP, and $H_0^{(2)}$ is the zeroth order Hankel function of the second kind. It should be emphasized that the required magnetic current densities, $M(y)$, is directly related to the desired focal pattern in 3.1. This is quite different from the approach in Figure 2.2 where the desired focal pattern was back propagated to find the required current densities. By eliminating the need to back propagate the focal pattern, we have further simplified the design procedure. However, it should be noted that the physics behind the operation of NFPs is still similar to the previous chapter and relies on radiationless interference.

Given the desired focal pattern H_{focal}, (3.1) can be solved using the Method of Moments [45]. The magnetic current density is treated as the unknown and discretized into $2N+1$ elements with Δy width. For example, pulse basis functions and the point matching method can be used to convert (3.1) into the following matrix equation:

$$\frac{-\omega\epsilon_0}{2}\sum_{m=-N}^{N}M_m H_0^{(2)}(k\sqrt{(|n-m|\Delta y)^2+L^2})w = H_{focal,n} \tag{3.2}$$

where n is an integer from $-N$ to N, w is the width of the grooves, $M_m = M(y = m\Delta y)$ and $H_{focal,n} = H_{focal}(n\Delta y)$. Since the magnetic current density has a non-zero value only at the groove locations, the width of each element is represented by w in (3.2). It should also be noted that M_0 represents the magnetic current assigned to the central slit. The equivalent problem for region 2 involves a TEM wave incident on

a magnetic current density, M_0. Considering only the dominant TEM mode within the waveguide, the electromagnetic fields in region 2 ($z < 0$) are governed by the following equation,

$$2H_{inc} + \frac{M_0}{\eta} = H_{total,n=0} \tag{3.3}$$

where $H_{total,n} = H_{total}(z = 0, y = n\Delta y)$, H_{inc} is the magnetic field of the incident electromagnetic wave, and η is the characteristic impedance of free space. The magnetic current density M_0, that is common to (3.2) and (3.3), ensures the continuity of the tangential electric field through the central slit. The continuity of the magnetic field is enforced by ensuring that the magnetic field $H_{total}(n\Delta y = 0)$ at the central slit,

$$H_{total,n} = \frac{-\omega\epsilon_0}{2} \sum_{m=-N}^{N} M_m H_0^{(2)}(k|(n-m)\Delta y|)w \tag{3.4}$$

produced by the magnetic currents M_m in (3.2), is the same as the one which appears in (3.3).

By solving (3.2), the magnetic current densities needed to produce the focal pattern H_{focal} can be found. Given the magnetic current densities and the continuity relation given by (3.4), the required incident magnetic field H_{inc} can be computed using (3.3). In the next step, the ratio of the magnetic currents and magnetic field at the surface of the plate is taken to obtain the required surface impedance:

$$Z(y = n\Delta y) = Z_n = \frac{M_n}{H_{total,n}}. \tag{3.5}$$

In the final step of the design process, the surface surrounding the slit is corrugated (see Figure 3.1) in order to realize the impedance profile given by (3.5). Only the imaginary part of the impedance is used given that the real part is negligible (see Chapter 2 and [14]). The width, w, and spacing, a, of all of the grooves are kept the same, while the depth, d_n, of the grooves is varied. Each groove can be considered as a

short-circuited waveguide. By varying the depth d_n of each groove, its input reactance can be changed. Using this short-circuited waveguide model, the input impedance of each groove is $j\eta \tan kd_n$ [35, 46]. This expression for the input impedance pertains to the idealized case where there are no fringing fields, and only the dominant TEM mode is present within the waveguide. To accurately determine the depth of the grooves, a full-wave electromagnetic solver can be used that takes into account all parasitics and higher order waveguide modes that are excited.

3.3 Simulation Results

To demonstrate the utility of the design procedure, we present two different corrugated NFPs. Both plates are designed following the procedure outlined above and full-wave simulation results verifying their operation are presented. Later in this chapter, experimental results verifying the performance of the second example are presented.

3.3.1 Example 1

In the first example, a linearly corrugated NFP is considered with the following parameters: $L = \frac{\lambda}{15}, a = \frac{\lambda}{40}, w = \frac{\lambda}{80}, N = 19$ where $\lambda = 30$ cm corresponds to a 1 GHz frequency of operation. The magnetic-field focal pattern is assumed to be a sinc function with a null-to-null beamwidth of $\lambda/10$,

$$H_{focal}(y) = \frac{\sin(qy)}{qy} = \text{sinc}(qy) \tag{3.6}$$

where $q = 10k$ determines the null-to-null beamwidth. At first, we assume that the metal is a lossless perfect electric conductor (PEC). Following the design procedure above, the required magnetic current densities have been computed and are listed in Table 3.1. The magnetic currents listed in Table 3.1 are normalized to the incident

Groove Index (n)	Normalized Magnetic Current Densities(M_n/E_{inc})
0	$1.9963\angle 176.4247°$
1	$0.4975\angle 176.5339°$
2	$1.5722\angle -3.6577°$
3	$1.0262\angle -3.6804°$
4	$0.8870\angle 176.4664°$
5	$0.9757\angle 176.4556°$
6	$0.5099\angle -3.7405°$
7	$0.8217\angle -3.6830°$
8	$0.3109\angle 176.5874°$
9	$0.6968\angle 176.4547°$
10	$0.2251\angle -3.8885°$
11	$0.5676\angle -3.6546°$
12	$0.1173\angle 177.0418°$
13	$0.5674\angle 176.3452°$
14	$0.2117\angle -4.2414°$
15	$0.2830\angle -3.1021°$
16	$0.1836\angle -5.2499°$
17	$0.8258\angle 175.8882°$
18	$0.6505\angle -4.4743°$
19	$0.1660\angle 173.9888°$

Table 3.1: The magnetic current densities representing the grooves of the linearly corrugated NFP in example 1. The magnetic current densities are normalized to the incident electric field computed using (3.3).

electric field, found using (3.3). Table 3.1 shows that the phase of adjacent magnetic current densities is reversed. As pointed out in the previous chapter, this rapid phase variation is a characteristic feature of NFPs. Given the magnetic current densities in Table 3.1, (3.5) is used to obtain the required surface impedance. Neglecting the real part of the surface impedance, the depths of the grooves needed to produce the focal pattern were found. The computed depths are shown in Figure 3.3.

The focal pattern produced by this corrugated NFP is plotted in Figure 3.4. The plot also shows the ideal focal pattern given by (3.6) (*Theory*), as well as the focal pattern produced by the discretized magnetic currents M_m (given by (3.2)) found using the Method of Moments (*MoM*). The NFP is simulated using a commercial
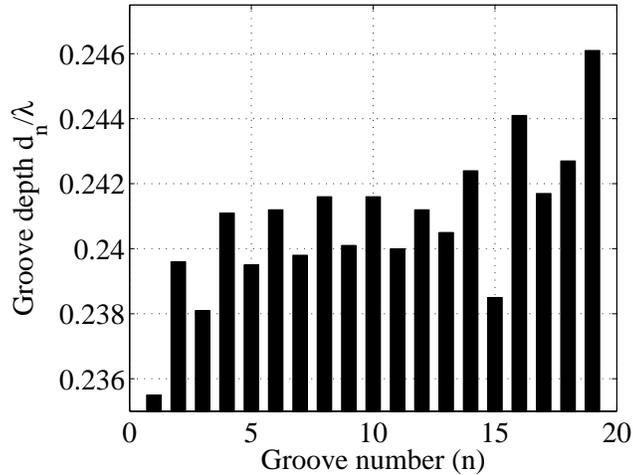
Figure 3.3: The groove depths for the corrugated NFP shown in Figure 3.1, designed to operate at 1.0 GHz. The plot is symmetric: $d_n = d_{-n}$.

finite element electromagnetic solver Comsol Multiphysics (*COMSOL*). The three focal patterns are nearly identical, thereby validating the described design procedure. It should be noted that the *COMSOL* pattern is plotted at 1.0015 GHz, while the other two curves are plotted at 1.0 GHz. This slight frequency shift in center frequency can be attributed to the initial assumption that the electric field is constant across the grooves.

Moreover, the effect of practical losses on the performance of the corrugated NFP is studied using Comsol Multiphysics by replacing the PEC boundaries of the structure with copper. A contour plot of the magnetic field is shown in Figure 3.5 for a plate with copper boundaries. The focal patterns with losses (copper) and without losses (PEC) are compared in Figure 3.6. As can be seen, losses have minimal effect on the performance of the NFP.

Although the designed corrugated NFP maintains a subwavelength focus despite losses, it still suffers from an impedance mismatch at its input. To remedy this, the corrugated surface was impedance matched to its waveguide feed using a single-stub matching network [46], as shown in Figure 3.5. The stub is located at 0.49571λ from the opening of the central slit, and has a length of 0.24017λ. The stub was chosen
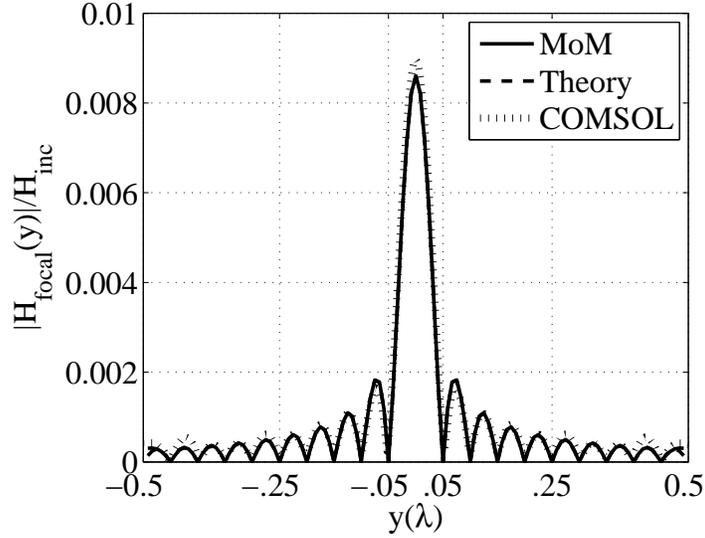
Figure 3.4: Focal patterns at 1.0 GHz formed by the NFP depicted in Figure 3.1. The curve labeled *MoM* represents the focal pattern produced by M_m given by (3.2), *Theory* is a plot of (3.6), and *COMSOL* is the focal pattern produced by the designed corrugated NFP.

to have a width equal to that of the central slit. Using the stub matching network, a return loss of around -15 dB was obtained for the plate. Through impedance matching, the maximum amplitude of the focal pattern ($H_{focal,0}$) was increased from $0.0098H_{inc}$ to $0.0817H_{inc}$. Therefore, impedance matching can clearly enhance the field at the focal plane.

3.3.2 Example 2

The linearly corrugated NFP presented in the previous example was fed through its central slit by a waveguide. The feeding mechanism of the linearly corrugated NFP is modified in this example. The modified structure is shown in Figure 3.7 and consists of two identical metallic slabs placed closely together. The gap between the slabs serves as the central slit. Both sides of each slab feature corrugations which run along the length of the slab (see Figure 3.7). The slabs are illuminated from one side by a plane wave, which is partially transmitted through the central slit. The side of the
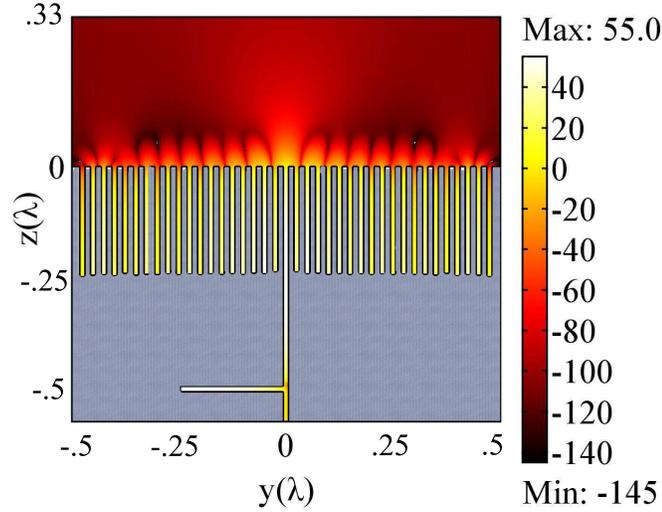
Figure 3.5: A cross-sectional view of the corrugated NFP designed to operate at 1 GHz. A contour plot (in dB) of the x-directed magnetic field formed by the device is shown, given a TEM wave with magnetic field $H_{inc} = 1$ incident from the waveguide feed. The magnetic field contour plot includes the effect of losses. The stub attached to the waveguide feed is used to impedance match the device.

plate illuminated by the plane wave, features a periodic input corrugation, referred to as IC. The other side of the plate features a non-periodic output corrugation, referred to as OC. The periodic IC is similar to the periodic corrugations discussed in subsection 3.1.1. The design and operation of these periodic corrugations have been thoroughly discussed in literature [33–44]. The purpose of the IC is to enhance the transmission of the plane wave through the central slit. On the other hand, the non-periodic OC, which forms the subwavelength focus, is a corrugated NFP, similar to the one of Example 1. Since the roles and operation of IC and OC are independent of each other, they can be designed separately. The OC is designed following the procedure outlined in Example 1. The IC is designed following an established procedure [33–44]. The performance of the entire structure including both IC and OC is studied using full-wave simulation. Finally, the structure is examined through experiment in the next section.
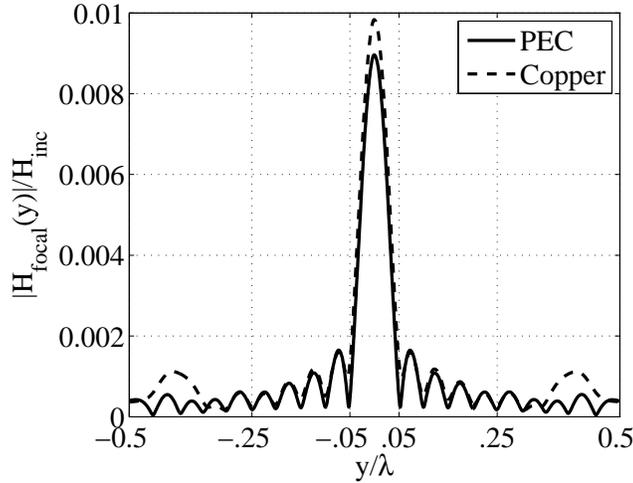
Figure 3.6: The focal pattern produced by the corrugated NFP with PEC (lossless) boundaries (solid line) and with copper (lossy) boundaries (dashed line), computed using Comsol Multiphysics.

In the design process, the slabs are initially assumed to be infinitely wide. Subsequently, the effects of the finite width and edge diffraction are considered. In the previous example, a sinc function magnetic-field focal pattern with null-to-null beamwidth of $\lambda/10$ was selected as the focal pattern (see Figure 3.8 (a)). This choice results in a transverse electric-field (E_y) focal pattern with null-to-null beamwidth of $\lambda/15$ as shown in Figure 3.8 (b). Figure 3.8 (b) reveals that the transverse electric-field (E_y) focal pattern exhibits significantly large side lobes. To remedy this, the magnetic-field focal pattern was chosen to be a zeroth-order Hankel function of the second kind (see Figure 3.8 (c)), with its spatial spectrum truncated to $q = 15k$. The corresponding E_y focal pattern approximates a sinc function with null-to-null beamwidth of $\lambda/15$ with small sidelobes, as shown in Figure 3.8 (d).

The operating frequency is set to 10.0 GHz, corresponding to $\lambda = 3.0$ cm. The other parameters are the same as those in the previous example: $L = \frac{\lambda}{15}, a_{OC} = \frac{\lambda}{40}, w_{OC} = \frac{\lambda}{80}, N_{OC} = 19$. Given these parameters and assuming lossless conditions, the required OC's groove depths, $d_{OC,n}$, were obtained, and are shown in Figure 3.9. With these groove depths, the structure was simulated using Comsol Multiphysics.
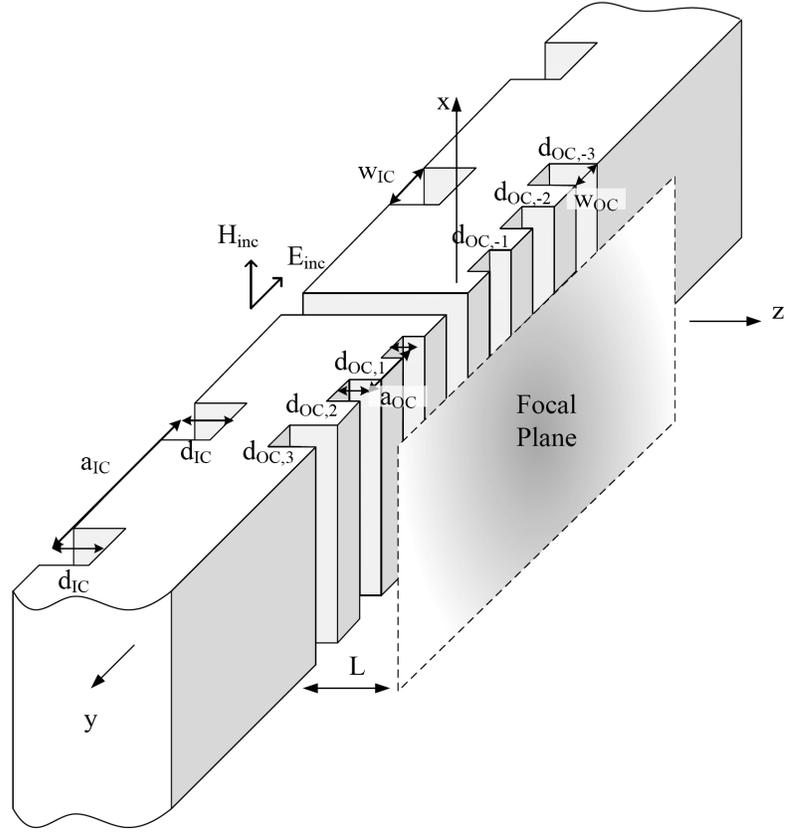
Figure 3.7: The linearly corrugated NFP discussed in section 3.3.2 (Example 2). The plate consists of two identical metallic slabs, placed closely together, to form the central slit. One side is periodically corrugated and is referred to as input corrugation (IC). The other side is non-periodically corrugated and referred to as output corrugation (OC). The IC enhances the transmission through the central slit while the OC forms a subwavelength focus on the other side.

The resulting focal patterns are plotted in Figure 3.10 and denoted as *COMSOL*. For comparison, the ideal focal patterns shown in Figure 3.8 are also plotted and labeled as *Theory*. In addition, the focal patterns computed using the Method of Moments are shown and denoted as *MoM*. To compute the *MoM* plot, the focal pattern produced by the magnetic current density on the OC is found. The induced magnetic current densities are found by substituting the imaginary part of the required surface
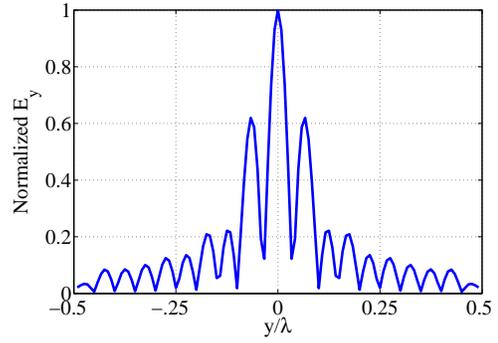
43

(a) Example 1 magnetic-field focal pattern

(b) Example 1 transverse electric-field focal pattern
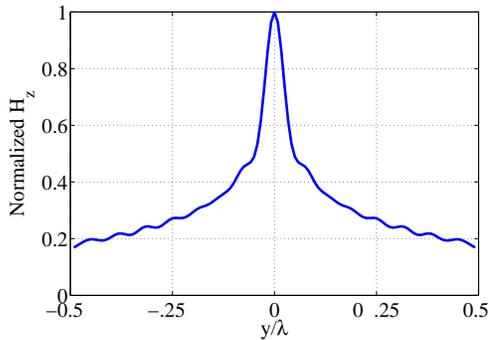
(c) Example 2 magnetic-field focal pattern
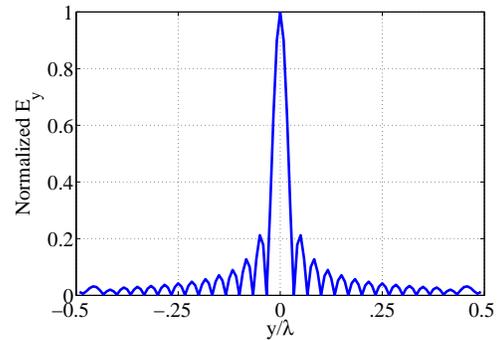
(d) Example 2 transverse electric-field focal pattern

Figure 3.8: Comparison of the desired focal patterns in example 1 and example 2. (a) Example 1 magnetic-field focal pattern: a sinc function with null-to-null beamwidth of $\lambda/10$. (b) Example 1 transverse electric-field focal pattern. (c) Example 2 magnetic-field focal pattern: a zeroth order Hankel function of the second kind with its spatial spectrum truncated to $q = 15k$. (d) Example 2 transverse electric-field focal pattern which approximates a sinc function with null-to-null beamwidth of $\lambda/15$.

44
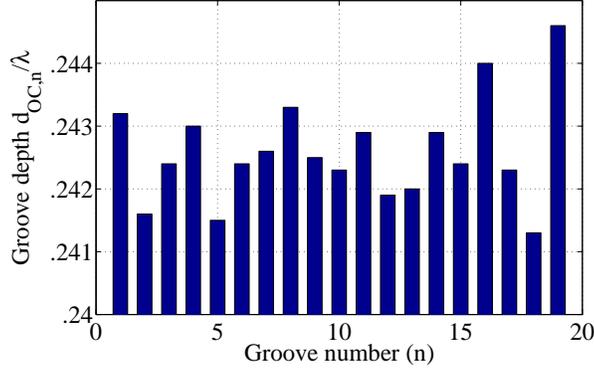
Figure 3.9: The groove depths for the OC of the NFP shown in Figure 3.7. The plate is designed to operate at 10.0 GHz. The NFP is symmetric: $d_{OC,n} = d_{OC,-n}$.

impedance, Z_n, into the equation below:

$$\frac{M_n}{Z_n} = \frac{\omega\epsilon_0}{2} \sum_{m=-N}^{N} M_m H_0^{(2)}(k|(n-m)\Delta y|)w \qquad (3.7)$$

Figure 3.10 shows good agreement between *MoM* and *COMSOL*, and thereby verifies the design procedure. However, both the *MoM* and *COMSOL* plots are different from the ideal pattern. This difference is due to the fact that the real part of the required impedance profile is ignored in the design procedure, when in fact it is not negligible in this particular case. One should note that the real part of the impedance profile cannot be realized by varying the grooves' depths. Finally, it should be emphasized that the simulation results are presented at 10.006 GHz, which differs from the design frequency of 10.0 GHz by 0.6%. As before, this slight frequency shift is attributed to the initial assumption that the electric field is constant across the grooves.

In order to study the effect of practical losses on the performance of the plate, the designed OC was resimulated with the PEC boundaries replaced with copper boundaries. The focal pattern produced by the lossy NFP is depicted in Figure 3.11 and denoted as *Copper*. The pattern produced by the lossless NFP is also depicted
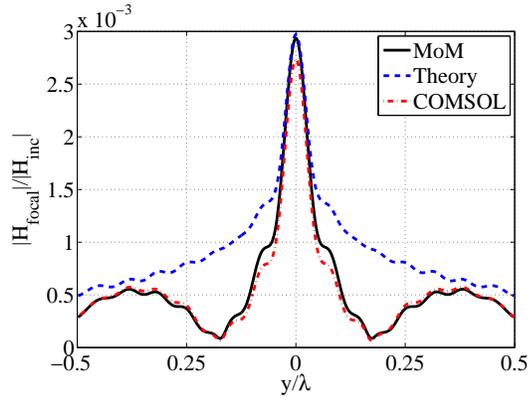
(a) Normalized magnetic-field focal pattern
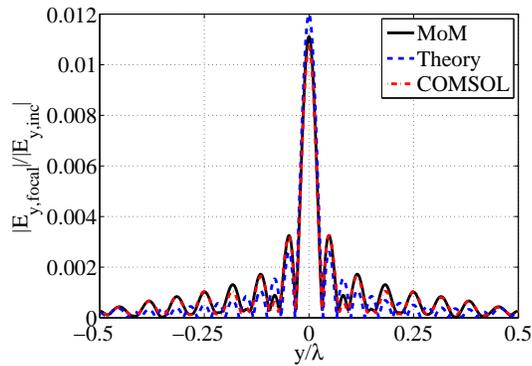
(b) Normalized transverse electric-field focal pattern

Figure 3.10: Normalized (a) magnetic-field and (b) transverse electric-field focal patterns produced by the OC of the NFP shown in Figure 3.7. The curve labeled *Theory* is the plot of the theoretical focal pattern. The curve *MoM* represents the focal pattern produced by the magnetic current densities computed using (3.7), and *COMSOL* is the focal pattern produced by the designed corrugated NFP.
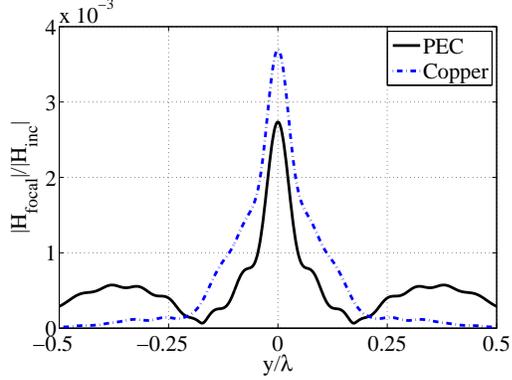
(a) Normalized magnetic-field focal pattern
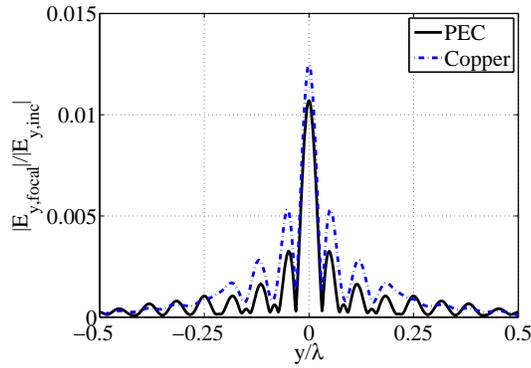
(b) Normalized transverse electric-field focal pattern

Figure 3.11: Normalized (a) magnetic-field and (b) transverse electric-field focal patterns produced by the OC of the corrugated NFP shown in Figure 3.7 with PEC boundaries (solid line) and with copper boundaries (dashed line). The patterns are computed using Comsol Multiphysics.

and denoted as *PEC*. The effect of loss is more pronounced here than in the previous example (see Figure 3.6), since conductor losses are higher due to the ten fold increase in frequency [46].

In the next step, the IC is designed to maximize transmission through the central slit. The IC design procedure has been outlined in literature [33–44]. Following the established procedure, the IC was designed and its parameters are as follows: $N_{IC} = 5$, $a_{IC} = 27.6$ mm $= 0.92\lambda$, $w_{IC} = 2.76$ mm $= 0.092\lambda$, and $d_{IC} = 4.15$ mm $= 0.138\lambda$. It is worth noting that the input corrugation is periodic with the groove separation a_{IC} equal to a guided wavelength of the surface mode supported by the IC at 10.0 GHz.
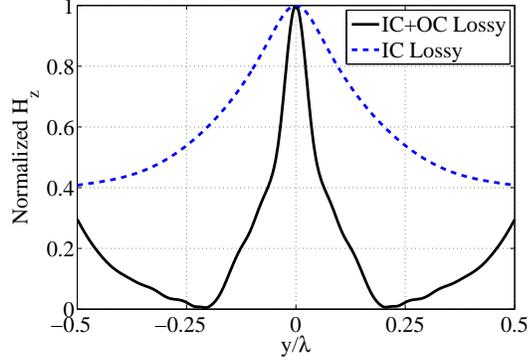
(a) Normalized magnetic-field focal pattern
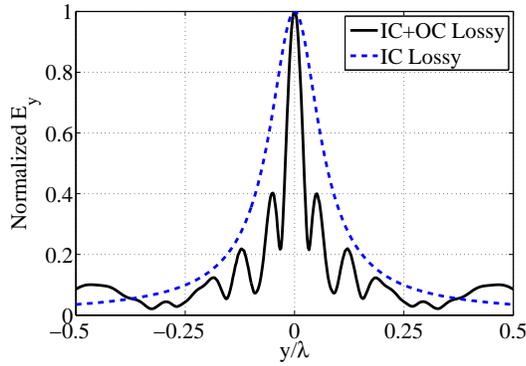
(b) Normalized transverse electric-field focal pattern

Figure 3.12: Normalized (a) magnetic-field and (b) transverse electric-field focal patterns produced by the corrugated NFP shown in Figure 3.7. The *IC+OC Lossy* plot represents the patterns produced by the lossy NFP while the *IC Lossy* plot represents the patterns produced by the lossy plate with the output corrugation (OC) removed.

Also, the depth and width of the input corrugations are subwavelength. Finally, the thickness of the slab is chosen to be $H = 14$ mm, which corresponds to a resonant length $(\lambda/2)$. This choice further enhances transmission through the central slit.

Given the parameters above for the IC and OC, the corrugated NFP shown in Figure 3.7 was simulated in Comsol Multiphysics. Conductor losses were included in the simulation and the results are shown in Figure 3.12, and denoted as *IC+OC Lossy*. For comparison purposes, the focal patterns produced by the plate when the OC is removed are also depicted and denoted as *IC Lossy*. The focal patterns produced by

the plate with the OC are significantly narrower than those produced without the OC.

In order to illustrate the effect of losses and diffraction from the edges separately, the focal patterns produced for different cases are depicted in Figure 3.13. The first graph is the same pattern shown in Figure 3.12 and is labeled as *IC+OC Lossy*. The second graph, labeled as *IC+OC Lossless*, is the pattern produced by the structure when there is no loss. As noted earlier, the effect of conductor loss is noticeable due to the high frequency of operation. The third graph, labeled as *OC Lossy*, is the focal pattern produced by the lossy structure when the IC is removed. When the IC is removed, the diffraction from the edges significantly changes the focal pattern. The last graph is labeled *OC Lossless*. This graph is the focal pattern produced by a lossless plate with the IC removed. These focal patterns significantly differ from the ones plotted in Figure 3.10. This difference clearly demonstrates the effects of the edge diffraction.

In the next section, the corrugated NFP presented in this example is fabricated and tested. The setup used to measure the plate's focal patterns is described in detail. Magnetic field measurements for the fabricated structure are also reported. For comparison purposes, the patterns produced by a single slit are measured. It is shown that the corrugated NFP produces significantly narrower patterns than a single slit in a metallic plate with dimensions equal to that of the IC.

3.4 Measurements

The experimental NFP consisted of two corrugated copper plates fabricated with 25 micron accuracy using wire electrical discharge machining (EDM). The corrugated NFP was measured using the setup shown in Figure 3.14. In this setup, a Gaussian beam telescope system [47, 48] was used to illuminate the IC of the corrugated plate. The magnetic field of the Gaussian beam was oriented along the grooves. The
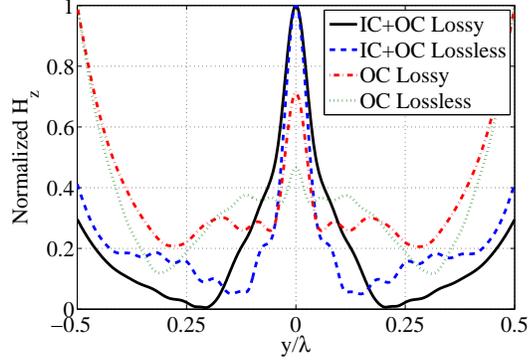
(a) Normalized magnetic-field focal pattern
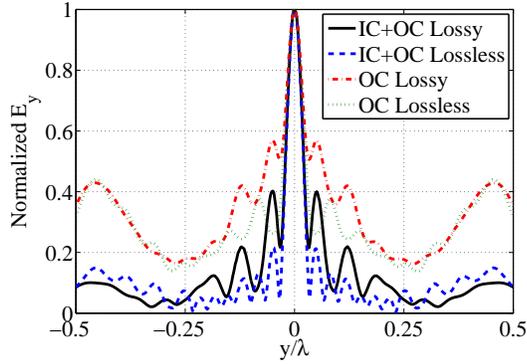
(b) Normalized electric-field focal pattern

Figure 3.13: Normalized (a) magnetic-field and (b) transverse electric-field focal patterns produced by the corrugated NFP shown in Figure 3.7. The *IC+OC Lossy* plot represents the pattern produced by the lossy plate. The *IC+OC Lossless* plot represents the pattern produced by the lossless plate. The *OC Lossy* plot represents the pattern produced by the lossy structure with the IC removed. The *OC Lossless* plot represents the pattern produced by the lossless plate with the IC removed.

Gaussian beam telescope was connected to port 1 of a network analyzer. To detect the magnetic-field focal pattern produced by the plate, a shielded loop antenna was scanned along the y direction at a distance 1 mm from the OC. The shielded loop had a diameter of 4.5 mm, and was made from 0.047 inch semi-rigid coaxial cable. The loop was connected to port 2 of the network analyzer. In this setup, the S_{21} measured by the network analyzer is a measure of the transmitted magnetic field.

The measured magnetic-field focal pattern is shown in Figure 3.15, and is denoted as *Corrugated Measurement*. To emphasize the narrowness of the focal pattern pro-

duced by the OC, we have also plotted a curve showing the measured magnetic-field pattern when the OC was removed (covered by copper tape), and is denoted as *Slit Measurement.* By covering the OC with copper tape, the grooves were short circuited and effectively removed. Therefore, the plate with the OC covered acted like a single slit with enhanced transmission resulting from the IC. The *Corrugated Measurement* exhibits a FWHM of $\lambda/9.23$, which is 3 times narrower than the *Slit Measurement* plot that exhibits a FWHM of $\lambda/3.07$. It should be noted that the simulated focal pattern, denoted as *Corrugated Simulation,* is slightly narrower than the measured one, exhibiting a FWHM of $\lambda/11$. The increased width of the experimental focal pattern can be attributed to the size of the shielded-loop used to probe the magnetic field. The radius of the probe was larger than the groove spacing of the OC, which determines the resolution of the subwavelength focus. Therefore, the size of the shielded-loop limited the spatial resolution that could be detected. Finally, the measurement results are reported at 10.007 GHz, while the simulation results are reported at 10.006 GHz. This negligible frequency shift can be attributed to the 25 micron tolerance of the fabrication process.

In order to investigate the transmission enhancement achieved by the IC, the measured signal levels detected by the loop placed close to the central slit are listed in Table 3.2. The signal levels when the IC is removed (covered by coper tape) are significantly lower than when the IC is present (not covered). These comparisons verify the enhanced transmission through the central slit achieved by the IC.

Finally, the emitted beam from the corrugated NFP with and without OC (single slit with IC) are compared in Figure 3.16. In the plot, the measured magnetic field (H_z) along each $z = z'$ plane has been normalized to its corresponding maximum value: $H_z(y, z = z')/H_z(y = 0, z = z')$. Figure 3.16 (a) shows the beam radiated from the NFP with the OC covered by copper tape, while Figure 3.16 (b) shows the beam radiated from the NFP. These two figures confirm the NFP's superior ability

51
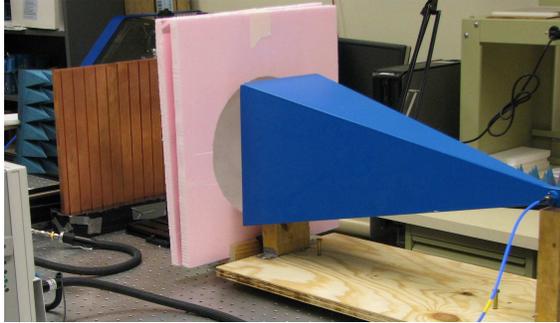
(a) Gaussian beam telescope illuminating IC
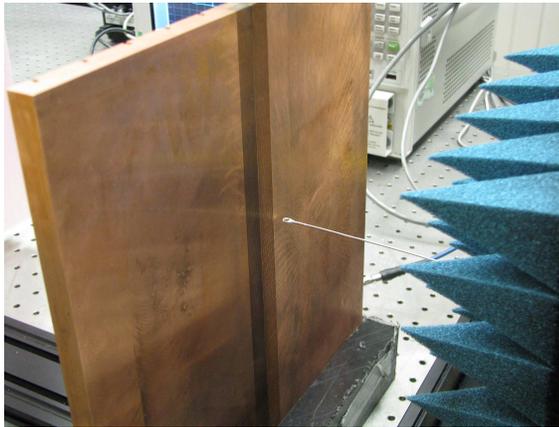
(b) Small loop measuring the pattern created by OC

Figure 3.14: Fabricated corrugated NFP and measurement setup. (a) The Gaussian beam telescope used to illuminate the input corrugation (IC). (b) The photograph depicts the small shielded loop used to measure the magnetic-field pattern created by the output corrugation (OC).

to confine the electromagnetic near field over an extended operating distance.

3.5 Conclusion

We have shown that a linearly corrugated NFP consisting of a waveguide-fed slit surrounded by non-periodic corrugations can focus electromagnetic fields to subwavelength resolutions. A general procedure for designing such a device was outlined. Two different examples of corrugated NFPs were designed and studied in full-wave simulation. The effect of losses was also considered, and two different methods for reducing the reflection from a NFP were demonstrated. In the first example, a single stub was
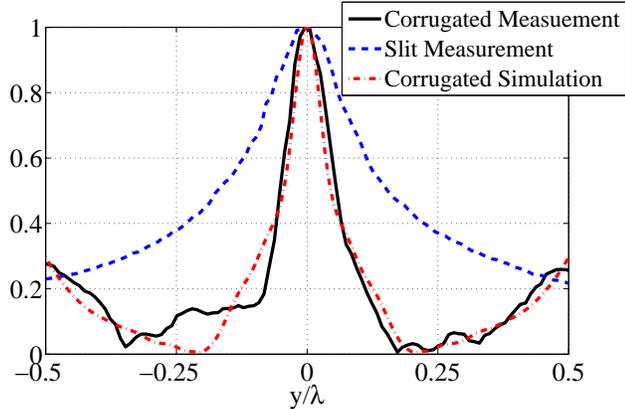
Figure 3.15: Normalized magnetic-field near-field patterns detected using the measurement setup shown in Figure 3.14. The *Corrugated Measurement* plot represents the measured magnetic-field pattern produced by the corrugated NFP while the *Slit Measurement* plot represents the pattern formed by the plate when OC is removed (covered by copper tape). The *Corrugated Simulation* plot is the simulated magnetic-field focal pattern produced by the NFP (computed using Comsol Multiphysics).

used to reduce the reflections while in the second example, periodic input corrugations were used to reduce reflections and enhance transmission. This second example was experimentally studied. The input face of the experimental plate was periodically corrugated to enhance transmission through the slit, while the output face of the plate featured a non-periodic corrugation which formed the subwavelength focus. Simulation and free-space measurements were reported at approximately 10 GHz, confirming the corrugated plate's ability to form a subwavelength focus. The subwavelength focus had a FWHM of $\lambda/9.23$ which was 3 times narrower than the focus produced by the single slit. Linearly corrugated NFP addressed the first limitation of NFPs. Namely, they can be fed directly through a waveguide. Furthermore, it illustrated a method to form desired magnetic-field near-field patterns. This idea has been pursued by others to manipulate magnetic field in the near field and design novel electromechanical actuators and transducers [49, 50].

Measurement	S_{11} (dB)	S_{21} (dB)
IC+OC	-9.7	-33.8
OC	-3.7	-37.12
IC	-7.5	-28.2
single slit	-3.34	-33.3

Table 3.2: The transmitted magnetic field amplitude for the different input/output corrugation configurations. The magnetic field amplitude is measured by placing the shielded loop close to the central slit. The S_{11} and S_{21} values are signals measured by the network analyzer when port 1 is connected to the Gaussian beam telescope and port 2 is connected to the shielded loop. *IC+OC* represents the measured signal when both the input and output corrugations are present. *OC* represents the measured signal when the input corrugation is removed (covered by copper tape). *IC* represents the measured signal when the output corrugation is removed (covered by copper tape). *Single slit* represents the measured signal when both input and output corrugation are removed (covered by copper tape).
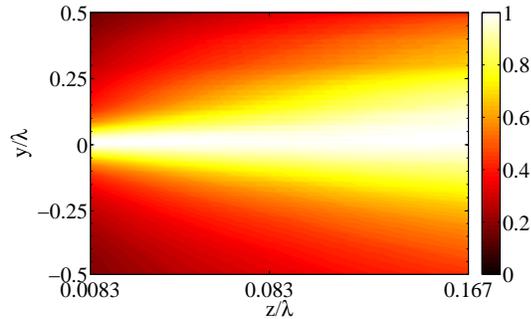
(a) Slit with IC
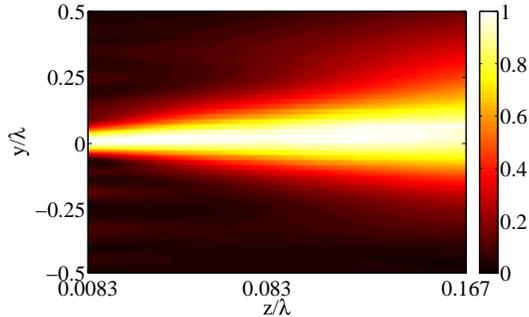
(b) NFP

Figure 3.16: Measured beam emitted from (a) the corrugated NFP with OC removed (covered by copper tape) and (b) the corrugated NFP. In both plots, the measured field along each $z = z'$ plane is normalized to its maximum value: $H_z(y, z = z')/H_z(y = 0, z = z')$.

CHAPTER IV

Concentrically Corrugated Near-Field Plates

4.1 Introduction

In the previous chapter, a corrugated NFP consisting of a waveguide-fed slit surrounded by linear, non-periodic corrugations was studied. It was shown that non-periodic corrugations can form a desired subwavelength magnetic-field focal pattern (line focus). The simulation results were then verified using an experimental, corrugated NFP.

The results of the previous chapter proved that NFPs can be fed through a waveguide. However, the linearly corrugated NFP still required further development to be of practical use in applications. Specifically, the NFP presented in the previous chapter could only produce a 1-D subwavelength focus (line focus), while a 2-D subwavelength focus is needed in most applications. Also, the plate of the previous chapter was excited using a parallel plate waveguide (slit), which may be difficult to feed in practice. Therefore, our goal in this chapter is to design a NFP which forms a 2-D focus, and can be fed through a simple coaxial connector. Such a device can find many applications ranging from near-field probing and sensing systems to biomedical and data storage devices.

The NFP examined in this chapter is referred to as concentrically corrugated NFP. It consists of a coaxially-fed central aperture surrounded by periodically-spaced

concentric grooves, as shown in Figure 4.1 (a). The grooves are spaced uniformly at a subwavelength distance and the depths of the grooves are non-periodically varied. We will show that such a device can localize the electromagnetic field emitted by the central aperture to a 2-D subwavelength spot at a near-field distance (focal length) $z = L$. The near-field focal spot can be designed to be much smaller than that produced by the central aperture alone. Therefore, this coaxially-fed concentrically corrugated NFP can provide extreme 2-D electromagnetic field confinement, and is well suited for applications such as near-field probing.

This chapter is organized into five sections. First, a procedure is outlined for designing a concentrically corrugated NFP. Simulation results are reported which confirm a designed NFP's ability to form a 2-D subwavelength focus. Next, the performance of the concentrically corrugated NFP is studied in experiment. The electric-field patterns produced by an impedance matched, concentrically corrugated NFP are measured at various distances. It is experimentally verified that the NFP produces focal patterns with significantly narrower beamwidths compared to those produced by a coaxial probe of the same dimensions. The measured electric-field patterns are also compared to those numerically computed for the measurement setup. Furthermore, the NFP's experimental frequency response is shown to be consistent with simulation results. Also, 2-D plots of the beams emitted by both the NFP and a coaxial probe are compared. The comparison confirms that the beam emitted from the NFP is confined over a larger operating distance (focal length) compared to a coaxial probe. Finally, the NFP is used to create 1-D and 2-D images of two in-phase dipole (coaxial) sources separated by a subwavelength distance. The images obtained using the NFP exhibit significantly higher resolution than those using a conventional coaxial probe. These results demonstrate the concentric NFP's ability to serve as a coaxially-fed, high resolution near-field probe.

(a) Concentrically corrugated NFP   (b) Magnetic current frills
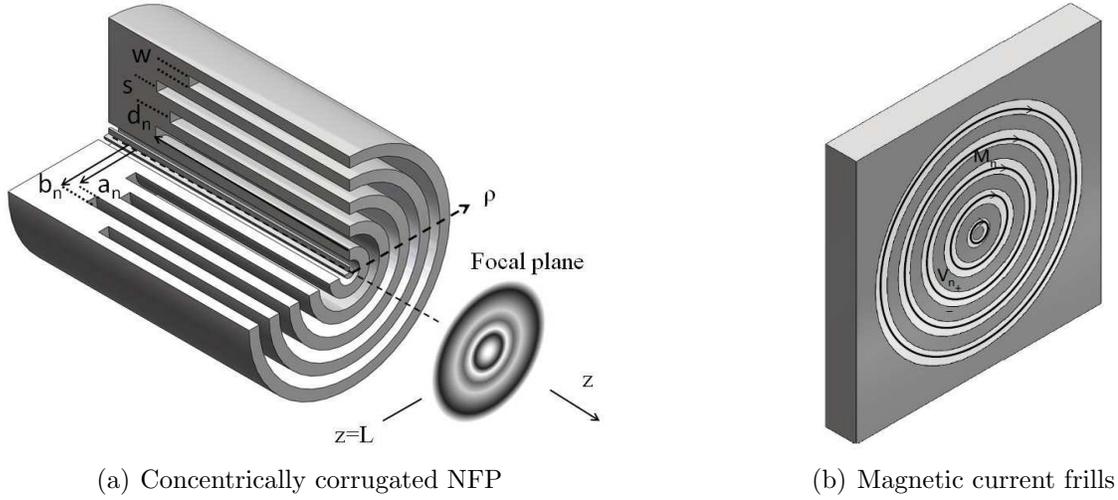
Figure 4.1: (a) A concentrically corrugated NFP. The concentric corrugations have uniform width and spacing, while their depths are varied non-periodically in order to shape the desired focal pattern at $z = L$. (b) The magnetic current frills used to model the concentric grooves in the design process. The n'th frill has a magnetic current density of M_n, and voltage V_n across it.

4.2 Design Procedure

The concentrically corrugated NFP depicted in Figure 4.1 (a) has N concentric circular grooves. The central aperture is coaxially fed. The grooves ($n = 1...N$) have uniform width w, inner radius a_n, and outer radius b_n, but their depths (denoted as d_1 to d_N) are non-periodically varied. For design purposes, the metallic surface into which the grooves are placed is assumed to be infinite in the x and y directions. In addition, each groove (n) is modeled as a magnetic frill (an annular ring of magnetic current) as shown in Figure 4.1 (b) [51]:

$$\vec{M}_n(\rho) = \frac{-V_n}{\rho \ln(\frac{b_n}{a_n})} \hat{\phi} \tag{4.1}$$

that exists between $a_n \leq \rho \leq b_n$, where V_n represents the voltage across each frill. The magnetic frills are equivalent sources with complex amplitudes equal to the tangential electric field across the openings of the coaxially-fed aperture ($n = 0$) and concentric

grooves $(1 \leq n \leq N)$.

The step-by-step procedure for designing the concentrically corrugated NFP is similar to those discussed in the previous chapters. The first step is to find the complex values of V_n needed to produce the desired electric-field focal pattern (E_z^{focal}) at a focal length $z = L$ from the plate. In this chapter, the z-directed electric field at the focal plane is assumed to be a subwavelength Airy pattern of the form:

$$E_z^{focal}(\rho) = E_z(z = L, \rho) = \frac{J_1(k_{max}\rho)}{k_{max}\rho} \tag{4.2}$$

where $k_{max} > k$ is the maximum radial wavenumber that comprises the focal pattern, and $k = 2\pi/\lambda$ is the wavenumber in free space. The wavenumber k_{max} dictates the resolution of the focal spot. By sampling the focal pattern at regular intervals, $\rho_m = 2mw$, E_z^{focal} can be expressed in terms of the magnetic frills as a matrix equation,

$$2\sum_{n=0}^{N} V_n f_{nm}(z = L, \rho = \rho_m) = E_z^{focal}(\rho_m) \tag{4.3}$$

where m is an integer from 0 to N, and $f_{nm}(z = L, \rho = \rho_m)$ is the z component of the electric field at $(z = L, \rho = \rho_m)$ produced by the nth groove. It should be noted that since image theory is used to simplify the problem to magnetic frills radiating in free space, the magnetic frill amplitudes must be doubled. The expression for f_{nm} is given by (A.1) of Appendix A. This Appendix summarizes the expression for near field of a magnetic current frill based on analytical formals derived in [51]. Through matrix inversion, the magnetic frill voltages V_n can be found from (4.3) given a desired E_z^{focal}. These voltages, along with (A.1), (A.2), and (A.3), allow the electric and magnetic field to be found anywhere in space.

The second step in the design process involves finding the azimuthal magnetic

field, H_ϕ, at the center of each magnetic frill $(\rho = \rho_n = (a_n + b_n)/2)$:

$$2 \sum_{p=0}^{N} V_p g_{pn}(z = 0, \rho = \rho_n) = H_\phi(z = 0, \rho = \rho_n) \tag{4.4}$$

where $g_{pn}(z = 0, \rho = \rho_n)$ is the ϕ component of magnetic field produced by p^{th} groove at $(z = 0, \rho = \rho_n)$, computed using (A.3).

The third step estimates the impedance seen at the opening of each groove from the quantities M_n and H_ϕ:

$$\eta_n = \frac{M_n(\rho_n)}{H_\phi(z = 0, \rho_n)} \text{ for } 1 \leq n \leq N \tag{4.5}$$

where the relationship between the computed V_n and M_n values is given by (4.1), and ρ_n is the same as in (4.4).

The final step of the design procedure entails determining the depths d_n of the grooves $(n = 1$ to $N)$ needed to realize the required values of η_n. This is achieved through scattering simulations. In the scattering simulations, the impedance (η_n) of a groove is extracted from normal incidence on an infinite array of linear grooves with identical widths w and depths. It should be noted that corrugations can only realize reactive impedances. However, since the real part of the required surface impedances is small, it can be neglected (see chapter 2).

In the design process, the fields in the space $z > 0$ were of primary concern. This region will be referred to as region 1, and the space inside the coaxial cable as region 2 (see Figure 4.1 (a)). The fields in regions 1 and 2 can be related to each other through the continuity of the tangential electric and magnetic fields across the central $(n = 0)$ coaxial aperture. Specifically, the incident current, I_{inc}, in the coaxial line (region 2) can be related to the field in region 1 through the following approximate expression,

$$2I_{inc} + \frac{V_0}{Z_0} = 2\pi \rho_0 H_\phi(z = 0, \rho_0) \tag{4.6}$$

Groove Index (n)	Normalized Voltage (V_n/V_{inc})	Groove Depth (d_n/λ)
0	$1.9999\angle0.0635°$	NA
1	$0.0830\angle-179.9026°$	0.2412
2	$0.0252\angle0.2079°$	0.241
3	$0.0080\angle-179.4839°$	0.2411
4	$0.0016\angle1.4271°$	0.2425

Table 4.1: The groove voltages and depths for the NFP depicted in Figure 4.1 (a). The voltages are normalized to the incident voltage computed using (4.6), where $V_{inc} = Z_0 I_{inc}$.

which considers only the TEM mode within the coaxial cable. The variable Z_0 represents the characteristic impedance of the cable and $\rho_0 = \rho_n$ in (4.4) when $n = 0$. In summary, Equations (4.3), (4.4) and (4.5) can be used to directly relate the incident current (I_{inc}) in the coaxial cable to E_z^{focal}.

4.3   Simulation Results

As an example, we consider a concentrically corrugated NFP designed to operate at a frequency of 1.0 GHz ($\lambda = 0.3$ m). Throughout this chapter, the dimensions are given in terms of the design wavelength, $\lambda = 0.3$ m. The design parameters were chosen to be: $N = 4$, $L = \lambda/15$, $w = \lambda/80$ and $k_{max} = 8\pi k$. The central coaxial feed dimensions were $a_0 = 0.635$ mm and $b_0 = 2.05$ mm, which correspond to standard semi-rigid coaxial cable dimensions. The design parameters, N, w, L, a_n, and b_n were chosen by taking into account fabrications constraints. The described plate produces a subwavelength Airy pattern at the focal plane with a null-to-null beamwidth of $\lambda/20$. The frill voltages, V_n, and required groove depths, d_n, are found through the design procedure presented in the previous section. They are listed in Table 4.1 [21]. It is worth noting that the signs of the voltage phase for adjacent elements (frills) are reversed. This is a characteristic feature of a NFP's aperture field and was also observed for NFPs of Chapters 2 and 3.

The designed NFP was then simulated in Comsol Multiphysics. In the simulations, the lossless metallic plate into which the grooves are placed is truncated to a radius of $\rho = 0.125\lambda$. The simulated focal pattern (*Corrugated*) produced by the NFP is shown in Figure 4.2 along with the ideal subwavelength Airy pattern (*Ideal*). In addition, the focal pattern generated by the computed magnetic frills (*Frills*) is plotted. The *Frills* and *Ideal* patterns differ since the *Ideal* pattern was slightly undersampled when the frill voltages, V_n, were found using (4.3). The slight difference between the *Corrugated* and *Frills* patterns results from the definition of the groove impedance, which assumes that the magnetic current across each groove is constant. In reality, the magnetic current varies and its variation is given by (4.1). Further, the formulas from Appendix A, used to find the fields due to the magnetic frills, are approximate. This also leads to the differences between the simulated *Corrugated* pattern and the *Frills* pattern. The simulated design operates at a frequency 1.195% higher than that predicted by the approximate formulas. Finally, to emphasize the narrowness of the focal pattern produced by the designed plate, Figure 4.2 shows a plot (*Coaxial*) of the z-directed electric field pattern produced by the isolated coaxial aperture ($n = 0$) in a ground plane without corrugations. Both the *Coaxial* and *Corrugated* patterns are subwavelength, since the focal plane is within the structure's near field. However, at the same focal distance, the concentric corrugations allow for a significantly narrower spot size.

To observe the effect of losses on the NFP's performance, the plate was also resimulated with a finite conductivity equal to that of aluminium. The focal pattern for the lossy plate is shown in Figure 4.3. The simulation results demonstrate that practical losses at microwave frequencies have a minimal effect on the beamwidth of the subwavelength focal pattern formed by the device. The ρ-component and norm of the electric field are also shown in Figure 4.4. Although the goal was to make a narrow E_z focal pattern, the norm of the electric field (Figure 4.4 (b)) is also significantly
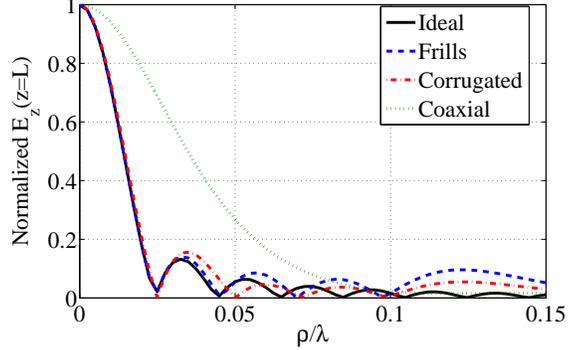
Figure 4.2: A subwavelength Airy function (*Ideal*) and z-directed electric-field focal patterns that approximate it. The *Frills* plot represents the focal pattern produced by the computed magnetic frills, while the *Corrugated* pattern represents the focal pattern formed by the lossless, concentrically corrugated NFP shown in Figure 4.1 (a). The *Corrugated* pattern shows a null-to-null beamwidth of $\lambda/20$ at a focal length $z = L = \lambda/15 = 0.02$ m, where $\lambda = 0.3$ m. The *Corrugated* and *Coaxial* patterns are plotted for a frequency 1.195% above the design frequency (1 GHz).
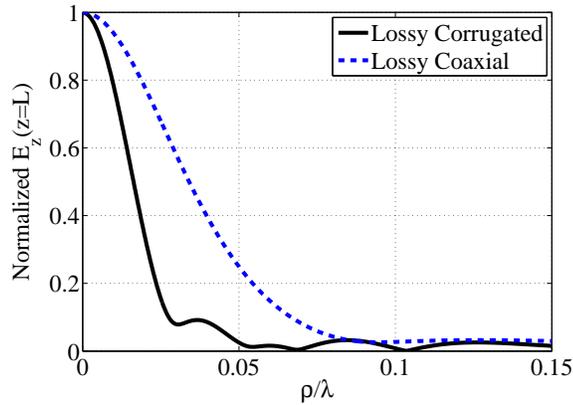
Figure 4.3: The focal pattern produced by the concentrically corrugated NFP with aluminium boundaries (solid line) versus the focal pattern produced by a coaxial aperture in an aluminium ground plane without corrugations. These results were computed using Comsol Multiphysics at a frequency 1.195% above the design frequency (1 GHz).

62
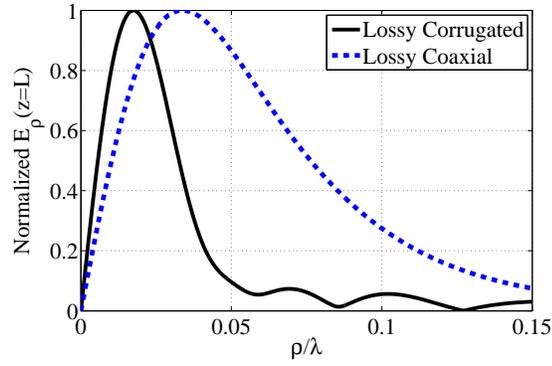
(a) ρ-directed electric-field focal pattern.
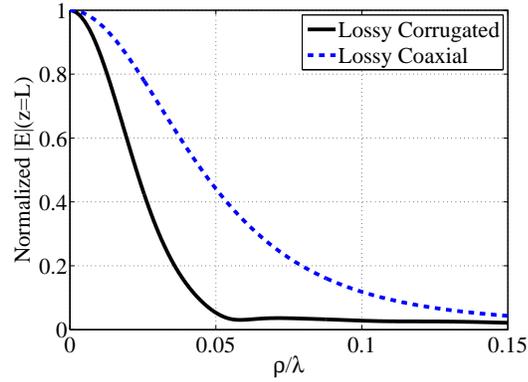
(b) Norm of electric-field focal pattern.

Figure 4.4: Simulated electric field at $z = L = 20$ mm from the concentrically cor-
rugated NFP (denoted as *Corrugated*) and a coaxial probe (denoted as
Coaxial). (a) Normalized ρ component of the electric field. (b) Normal-
ized norm of the electric field.
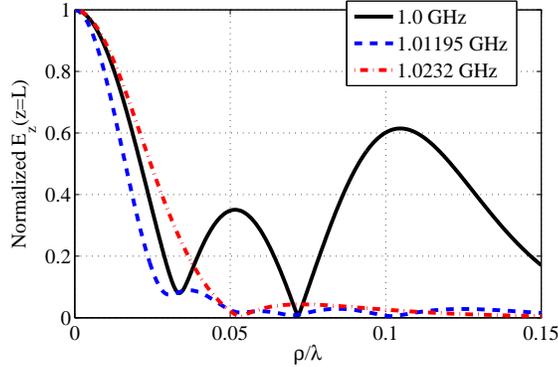
Figure 4.5: The concentrically corrugated NFP's frequency response. The NFP's operating frequency is 1.01195 GHz.

narrower than that of a coaxial probe.

Finally, the frequency response of the NFP is shown in Figure 4.5. Below the operating frequency, the side lobe levels increase significantly. In contrast, above the operating frequency, the side lobes are suppressed and the main beam widens with increasing frequency. The FWHM, which is $\lambda/30.73$ at the operating frequency 1.01195 GHz, increases by 50% as the frequency is increased to 1.0232 GHz (1.11% increase in frequency).

In the next section, fabricated structures and setup used to measure them are described in detail. Electric field measurements for both a simple coaxial probe and the concentrically corrugated NFP of equal dimensions are compared. It is shown that the simulated and experimental results are in close agreement, thereby validating the design procedure of the concentric NFP and its performance.

4.4   Measurements

The experimental setup used to measure the z-directed electric field patterns produced by the concentric NFP is illustrated in Figure 4.6. In the setup, a semi-rigid probe with an inner conductor radius of 0.46 mm and outer conductor radius of 1.8 mm was used to detect the NFP's electric-field patterns. The inner conductor of
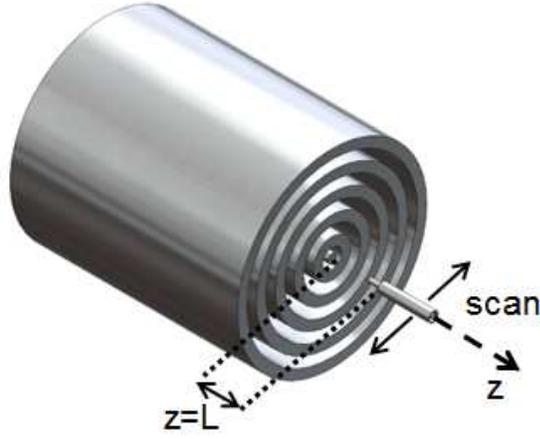
Figure 4.6: A concentrically corrugated NFP and the semirigid probe used to measure the electric patterns.

the semirigid probe was extended 4.5 mm to increase the signal strength received by the probe. The distance between the outer conductor of the semirigid probe and the surface of the corrugated plate was considered the measurement distance. Therefore, to measure a focal pattern at $z = L = \lambda/15 = 20$ mm, the semirigid probe was placed such that its outer conductor was 20 mm from the surface of the NFP. In the experiments, the semirigid probe was moved using an automated xyz translation stage.

The designed NFP was fabricated with 12.5 micron (0.5 mil) accuracy by electric discharge machining (EDM) an aluminium cylinder (see Figure 4.7 (a)). For comparison purposes, a coaxial probe of equal dimensions, consisting of a single coaxial aperture without corrugations, was also fabricated, as shown in Figure 4.7 (b). At the experimental frequency of 1.0105 GHz, the reflection coefficient of the concentrically corrugated NFP was measured to be −0.75 dB. Such a high reflection coefficient is expected, given that the feed of the NFP terminates in an open circuit. However, when the NFP is used as a probe in the following section, a lower reflection coefficient was needed to increase its sensitivity: the received signal strength. Therefore, the NFP was matched using a double stub tuner to obtain a reflection coefficient of

−6.5 dB at 1.0105 GHz. In addition, the semirigid probe used in the measurement setup (shown in Figure 4.6) was also matched using a double stub tuner to a reflection coefficient of −13.3 dB.

The simulated and measured electric-field patterns along the focal plane ($z = L = 20$ mm) of the NFP are shown in Figure 4.8 (a). The experimental focal pattern formed by the NFP is labeled *Corrugated Measurement* and exhibits a FWHM of $\lambda/23.58$. At the same distance, the experimental pattern formed by the coaxial probe (without corrugations) was measured. It is labeled *Coaxial Measurement*. This pattern exhibits a FWHM of $\lambda/13.14$, which is 1.79 times wider than that produced by the NFP. A third pattern is also plotted in Figure 4.8 (a) and labeled *Corrugated Simulation*. It is the simulated focal pattern of the NFP detected by the semirigid probe along the focal plane $z = L = 20$ mm. It is computed using the Ansys HFSS finite element electromagnetic solver. Similarly, *Coaxial Simulation* is the simulated electric-field pattern of the coaxial probe detected by the semirigid probe at the same distance. Both *Corrugated Simulation* and *Coaxial Simulation* show good agreement with the measured patterns, but clearly differ from the E_z patterns plotted in Figure 4.3. The difference is due to the fact that the semirigid probe, used to obtain the simulation and measurement results of Figure 4.8, couples slightly to the ρ component of the electric field in addition to the z component. Furthermore, the finite radius and length of the semirigid probes inner conductor slightly averages the electric field in both the ρ and z directions. The simulation of Figure 4.8 accurately captures the limitations of the semirigid probe used in experiment.

It should be noted that the HFSS simulations are reported at the design frequency of 1.01195 GHz, while the experimental results are reported at 1.0105 GHz: the fabricated plate's operating frequency. This 0.14% frequency shift can be attributed to the 12.5 μm tolerance of the EDM process used to fabricate the NFP. Figures 4.8 (b) and 4.8 (c) show the simulated and measured electric-field patterns at $z =$

(a) Corrugated NFP.
(b) Coaxial probe.

Figure 4.7: (a) A concentrically corrugated NFP fabricated from an aluminum cylinder using sink EDM. The NFP is fed by an SMA connector from the bottom side. (b) A coaxial probe consisting of a coaxial aperture in a cylindrical aluminum cylinder fed by an SMA connector from the bottom side.

$3L/4 = 15$ mm and $z = L/2 = 10$ mm respectively. Once again, the measurement results show excellent agreement with simulation. Finally, it should be pointed out that the measured pattern for the matched NFP and semi-rigid probe is 7 dB higher than the measured pattern for the unmatched case at the same distance.

In Figure 4.9, the electric-field pattern measured at $z = 10$ mm is plotted for different frequencies. Below the operating frequency (1.0105 GHz), the electric-field pattern produced by the corrugated plate shows ripples with no main beam, while above the operating frequency the main beam widens with increasing frequency. This frequency dependance agrees with the simulation results of the previous section.

To demonstrate the NFP's ability to confine the electromagnetic near field to a symmetric narrow spot, the measured 2-D electric field patterns at $z = 15$ mm for both the corrugated NFP and the coaxial probe are depicted in Figure 4.10. Finally, beam emitted from the coaxial probe and the corrugated NFP are compared in Figure 4.11. The measured electric field (E_z) along each $z = z'$ plane has been normalized to its corresponding maximum value: $E_z(\rho, z = z')/E_z(\rho = 0, z = z')$. These two figures confirm the superior ability of the NFP to confine the electromagnetic near field over
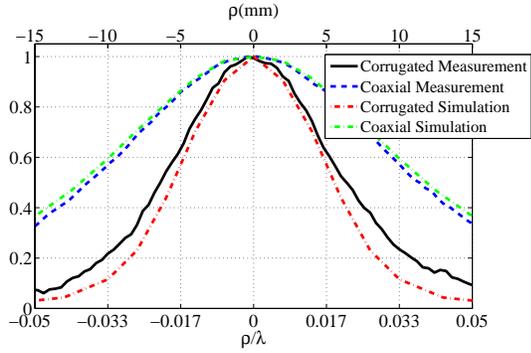
(a) $z = 20$ mm.
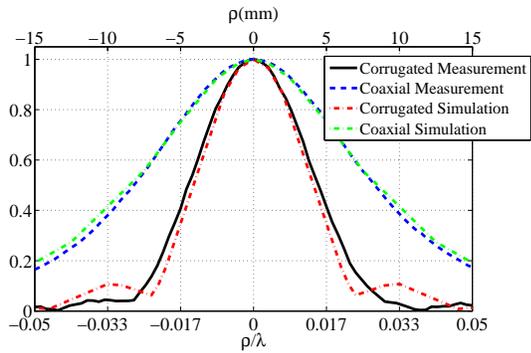
(b) $z = 15$ mm.
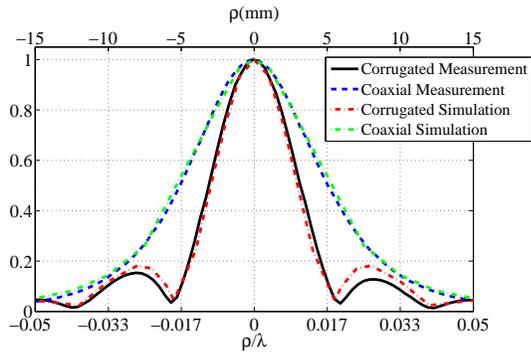
(c) $z = 10$ mm.

Figure 4.8: (a) Electric near-field patterns at $z = 20$ mm formed by the concentric NFP and detected using the measurement set up shown in Figure 4.6. *Corrugated Measurement* and *Coaxial Measurement* are the measured near-field patterns formed by the impedance matched concentrically corrugated plate and coaxial probe, respectively. *Corrugated Simulation* and *Coaxial Simulation* are the corresponding simulated near-field patterns. (b) Electric near-field patterns at $z = 15$ mm. (c) Electric near-field patterns at $z = 10$ mm. The simulation results include dielectric and conductor losses.
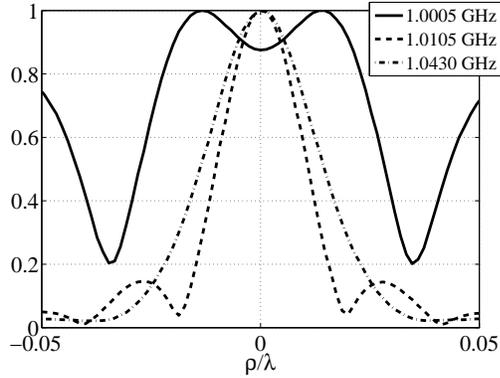
Figure 4.9: Measured near-field patterns generated by the concentrically corrugated NFP at $z = 10$ mm for different frequencies. The NFP's operating frequency is 1.0105 GHz.

an extended operating distance. In the next section, the electromagnetic confinement provided by the NFP is used to resolve two sources separated by a subwavelength distance.

4.5 Detection of Sources

Figure 4.10 demonstrates that the concentrically corrugated NFP produces higher resolution focal spots than a conventional coaxial probe. This also suggests that the NFP can provide higher resolution when imaging sources. To test this, two dipole sources (coaxial) separated by a distance s were placed at distance $z = 15$ mm from the NFP. The distance s is defined as the distance between the centers of the two dipole sources. The concentrically corrugated NFP and the coaxial probe were used to image the two sources by detecting the field emitted by the sources. Figure 4.12 shows the detected patterns for two different separation distances s. The pattern measured by the NFP is denoted as *Corrugated*, while *Coaxial* denotes the pattern measured by the coaxial probe. For comparison purposes, the pattern measured by a simple semi-rigid probe (with inner radius 0.52 mm, outer radius 2.20 mm, and a 5.2 mm extended inner conductor) is also shown in Figure 4.12, and denoted as
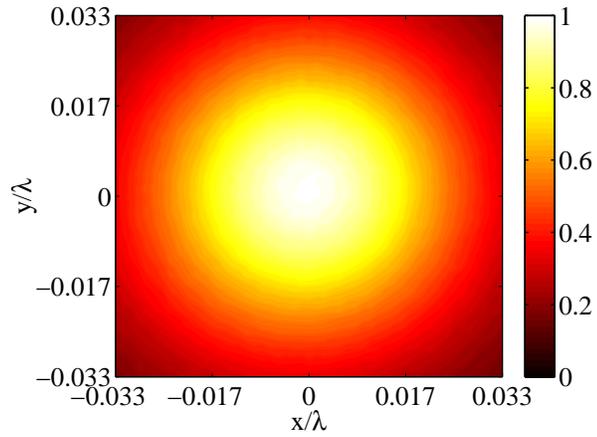
(a) Coaxial probe
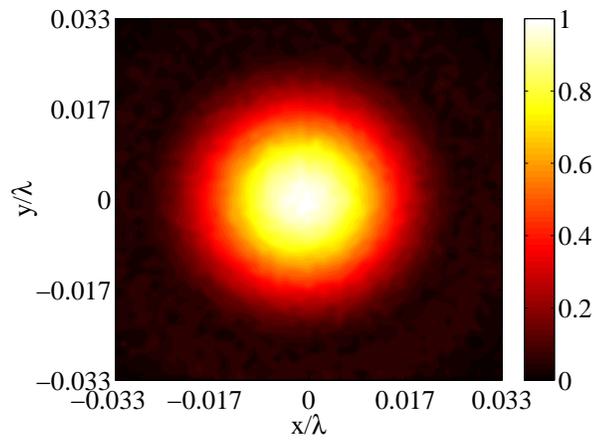
(b) NFP

Figure 4.10: Measured two-dimensional focal patterns ($z = 15$ mm) produced by (a) the coaxial probe and (b) the concentrically corrugated NFP.
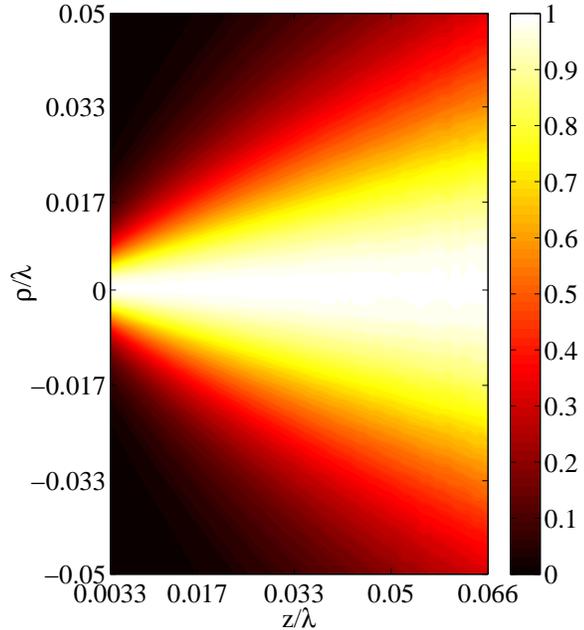
(a) Coaxial probe
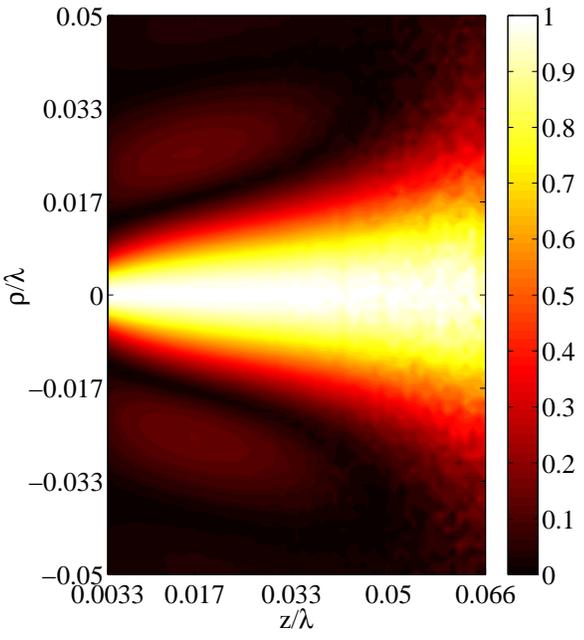
(b) NFP

Figure 4.11: Measured beam emitted from (a) the coaxial probe and (b) the concentrically corrugated NFP. In both plots, the measured field along each $z = z'$ plane is normalized to its maximum value: $E_z(\rho, z = z')/E_z(\rho = 0, z = z')$. The near-field patterns along $z = 0.066\lambda = 20$ mm, $z = 0.05\lambda = 15$ mm, and $z = 0.033\lambda = 10$ mm are plotted in Figure 4.8.

71

Probe.

Figure 4.12 (a) shows the extreme case when the sources cannot be resolved by the coaxial probe. In this figure, the sources have been placed $s = 9.1$ mm $= \lambda/33$ apart. In contrast, the NFP can distinguish between the two sources (see Figure 4.12(a)). The distance between the two peaks measured by the corrugated NFP is 7.9 mm $= \lambda/38$, while the separation between the two sources is $s = 9.1$ mm $= \lambda/33$. The difference is due to the superposition of the field incident from the two sources. The 2-D patterns measured using the NFP and the coaxial probe are shown in Figure 4.13. The two sources are easily distinguishable from the pattern measured by the NFP, while the pattern measured by the coaxial probe shows only one source.

Figure 4.12 (b) shows another extreme case, where the two sources are resolvable by the coaxial probe. In this case, the two sources are placed $s = 13.8$ mm $= \lambda/21.74$ apart. It is evident that the NFP can resolve the two sources completely, while the coaxial probes can only distinguish between them. The separation between the two sources observed using the corrugated NFP is 14.2 mm $= \lambda/21.1$, which is very close to the physical separation distance of $s = 13.8$ mm $= \lambda/21.74$. The higher resolution obtained using the corrugated NFP in resolving the two sources is more pronounced in the 2-D patterns shown in Figure 4.14.

4.6   Conclusion

In this chapter, we addressed two major limitations of initial NFP designs: The initially reported NFPs were excited by cylindrical or plane wave sources and could only produce a one-dimensional subwavelength focus [14–16]. To overcome these limitations, we developed concentrically corrugated NFPs which can be fed through a coaxial connecter and produce a 2-D subwavelength focal pattern. A step-by-step procedure for designing such plates was outlined. In addition, simulation results were presented that confirm the designed NFP's ability to create a 2-D focus. The effect
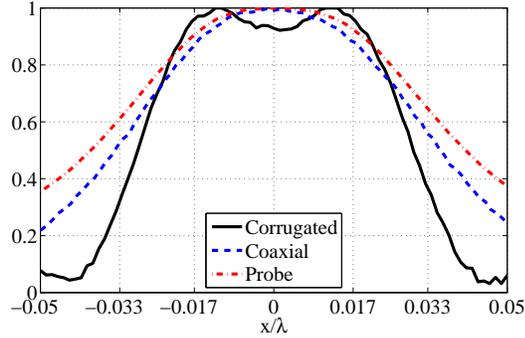
(a) separation distance $s = 9.1$ mm $= \lambda/33$
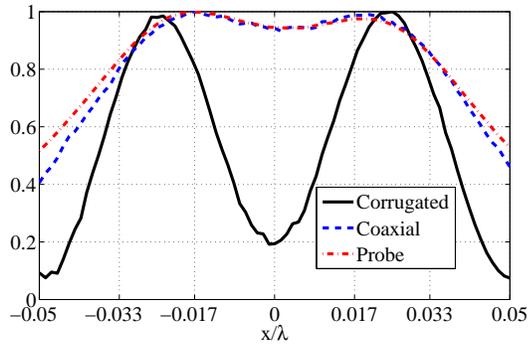
(b) separation distance $s = 13.8$ mm $= \lambda/21.74$

Figure 4.12: Resolving two dipole (coaxial) sources located at $z = 15$ mm and separated by (a) $s = 9.1$ mm $= \lambda/33$ and (b) $s = 13.8$ mm $= \lambda/21.74$ along the x axis ($y = 0$). The plot labeled *Corrugated* denotes the electric near-field pattern measured using the concentrically corrugated NFP. The plot labeled *Coaxial* denotes the pattern measured using the coaxial probe. The plot labeled *Probe* denotes the pattern measured using a semirigid coaxial probe (with inner radius 0.52 mm, outer radius 2.20 mm, and a 5.2 mm extended inner conductor).
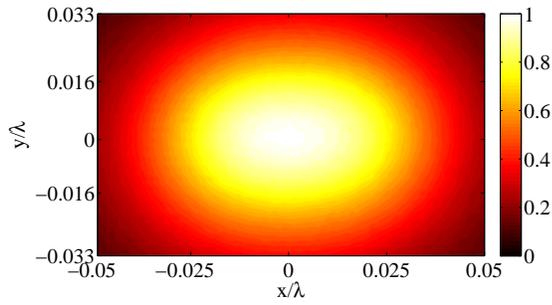
(a) Coaxial probe
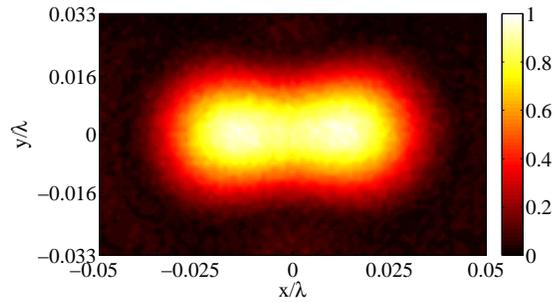
(b) NFP

Figure 4.13: Resolving two dipole sources (coaxial) located at $z = 15$ mm and separated by $s = 9.1$ mm $= \lambda/33$. (a) Two-dimensional electric near-field pattern measured using the coaxial probe. (b) Two-dimensional pattern measured using the corrugated NFP.
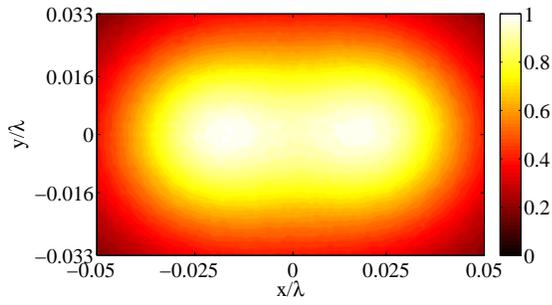
(a) Coaxial probe
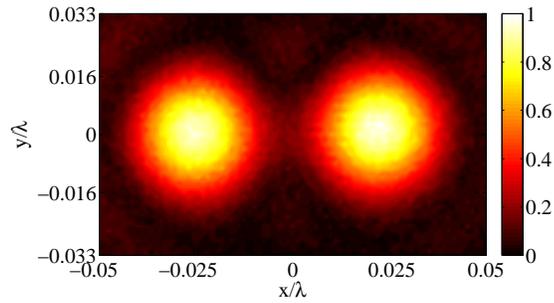
(b) NFP

Figure 4.14: Resolving two dipole sources (coaxial) located at $z = 15$ mm and separated by $s = 13.8$ mm $= \lambda/21.74$. (a) Two-dimensional electric near-field pattern measured using the coaxial probe. (b) Two-dimensional pattern measured using the corrugated NFP.

of practical losses on the performance of the NFP was shown to be minimal, and its frequency response was also studied. Furthermore, the experimental performance of an impedance matched concentrically corrugated NFP was investigated. The electric field patterns produced by the corrugated plate and a simple coaxial probe (without corrugations) of the same dimensions were compared for different focal distances at approximately 1 GHz. The subwavelength electric-field pattern produced by the corrugated NFP at $z = \lambda/15 = 20$ mm was shown to possess a FWHM that is 1.79 times narrower than that of the coaxial probe. Measurement and simulation results were shown to be in close agreement, thus validating the design procedure. In addition, the beam emitted by the corrugated NFP was narrower than that emitted by the coaxial probe, thus confirming the NFP's superior ability to confine electromagnetic field over a focal length (an extended operating distance). Finally, the NFP was used to image two coaxial sources placed a subwavelength distance apart. The images obtained using the NFP exhibited significantly higher resolution than those obtained using the coaxial probe. The results reported in this chapter demonstrate that non-periodic, concentrically corrugated surfaces can provide new opportunities to develop high resolution near-field probes and sensors.

CHAPTER V

Generating Evanescent Bessel Beams Using Near-Field Plates

5.1 Introduction

In the previous chapter, we experimentally demonstrated a concentrically corrugated near-field plate (NFP) that could generate prescribed subwavelength focal spots. This plate also obtained images with higher resolution compared to a conventional coaxial probe. Its coaxial feed as well as its ability to produce a 2-D subwavelength focus addressed the practical limitations of earlier NFP designs.

Now that a NFP more suitable for practical applications has been developed, our goal in this chapter is to apply its tailoring capabilities to a current electromagnetic problem. To this end, we demonstrate a concentrically corrugated NFP that can produce evanescent Bessel beams. Evanescent Bessel beams exhibit limited diffraction and can retain nearly constant subwavelength beamwidth over a near-field distance. While practically appealing, they have been difficult to generate and thus, have not found their role in practice. In this chapter, the tailoring capabilities of NFPs paves the way for a simple, yet effective, method for generating them.

Before developing NFPs that can generate evanescent Bessel beams, we first review the interesting properties of propagating and evanescent Bessel beams, and their
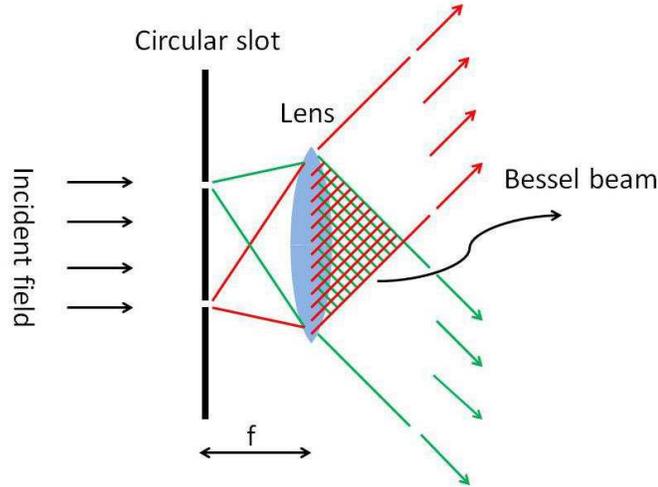
Figure 5.1: Schematic of the device used by Durnin to experimentally demonstrate a propagating Bessel beam.

potential applications. We also briefly survey earlier structures proposed for generating evanescent Bessel beams. Next, we will demonstrate how the tailoring capabilities of NFPs can be used to generate evanescent Bessel beams. In this chapter, we will also propose and examine uniform impedance surfaces and electrically-large annular slots that can generate Bessel beams.

5.1.1 Bessel Beams

Bessel beams propagate in free space without undergoing diffraction and as a result retain their transverse field pattern. They were first proposed by Durnin in [52] and referred to as "diffraction-free beams". Ideal Bessel beams theoretically carry infinite energy and thus cannot be realized in practice. However, they can be approximated. In [53], Durnin verified his theoretical proposal by demonstrating the first experimental approximation of a Bessel beam at optical frequencies. Since then, Bessel beams have been a topic of significant research interest [54–70].

Bessel beams can be decomposed into plane waves with wave vectors forming a cone [52]. This idea has been the basis for approximating Bessel beams in practice. Durnin and colleagues produced the first Bessel beam by illuminating a circular slit

located at the focal plane of a lens as shown in Figure 5.1 [53]. The radiation of the circular slit is transformed by the lens into plane waves with wavevectors forming a cone, resulting in a Bessel beam. Herman and Wiggins used a conically shaped optical element called an axicon to generate Bessel beams [56]. More recently, Pendry proposed using a distributed Bragg reflector with a central cavity [58]. In that configuration, the spatial filtering effect of the Bragg reflector produces plane waves with wave vectors lying on a cone.

Applications of Bessel beams have also received strong interest in the past few years. Much of this interest stems from the ability of Bessel beams to retain their beamwidth and transverse pattern over considerable distances. In [59], this property of Bessel beams was used to develop near-field probes that operate over larger distances than conventional ones, while maintaining the same resolution. In [71,72], this property was employed in micro drilling of metallic objects with high precision and high aspect ratios. In [60], the scattering of a zero-order Bessel beam by a dielectric sphere was formulated. In [61], Bessel beams were shown to be robust to distortion caused by obstacles. This feature was exploited in [62] to develop microscopy schemes with higher image qualities. In [63], two Bessel beams propagating along the same axis, but with different wavevectors, were shown to exhibit a self-imaging property: the longitudinal Poynting vector of the combined beams is periodic with respect to the axial distance. In [64], this property was used to trap and move small particles.

While these works primarily focused on propagating Bessel beams, Leizer and colleagues showed that evanescent Bessel beams can also exist, and are also solutions of Maxwell's equations [65]. They went on to demonstrate in simulation that evanescent Bessel beams can be produced through the total internal reflection of propagating Bessel beams [65]. This method of generating evanescent Bessel beams was later experimentally verified in [59].

Since that time, several other methods of producing evanescent Bessel beams have

been proposed. In [58], Pendry showed how a point source located close to a thin dielectric slab can produce a cylindrical surface wave that generates an evanescent Bessel beam. Zhan and colleagues proposed [66] and experimentally verified [67] that evanescent Bessel beams can be generated by the angular filtering of radially polarized light using a surface plasmon resonance. They also explored the generation of evanescent Bessel beams using highly focused cylindrical vector beams and the gigantic transmission band-edge resonance in one dimensional photonic bandgap structures [68, 69].

Evanescent Bessel beams can have a subwavelength main beam with a transverse pattern that is fixed over a near-field distance. This property is of high practical value in applications such as near-field probing, microscopy, high-density data storage, and medical targeting devices. While evanescent Bessel beams are attractive, they have not been simple to realize, and thus have not found their place in practice. In this chapter, we propose NFPs as effective, yet simple structures for generating evanescent Bessel beams.

In the NFP approach, a concentrically corrugated NFP is designed to form a Bessel focal pattern at a near-field distance. Since a Bessel beam is non-diffracting, the field profile at other near-field distances will be invariant. This approach is different from the earlier methods of generating Bessel beams. Conventionally, a device is used to filter the spectrum of the incident field to approximate the spectrum of a Bessel beam: a ring in the spectral domain. For example, the lens deployed by Durnin (shown in Figure 5.1) yields the Fourier transform of the electromagnetic radiation from the circular slit which is a Bessel function [53]. Similarly, Pendry and Zhan filtered the spectrum of the incoming wave by passing it through a resonator [58, 66–69].

While NFPs can produce evanescent Bessel beams, it will be shown that simpler impedance surfaces are also capable of generating evanescent Bessel beams. For example, a uniform inductive surface impedance can be designed to generate an evanescent

Bessel beam. This can be accomplished by launching a cylindrical TM surface wave on the inductive surface. The design and operation of such a configuration is studied in the next section. Edge diffraction is shown to limit its performance. In the following section, we examine a similar structure consisting of an electrically-large, uniformly-fed annular slot in a metallic surface. It is analytically shown that such a structure produces a Bessel beam close to its axis. However, its does not allow the beamwidth of the generated Bessel beam to be controlled. Hence, we present NFPs which can produce evanescent Bessel beams with tailored properties, and thus, a better method for generating such beams. NFPs allow the truncation of a Bessel beam to be altered, in order to mitigate the diffraction. As a result, NFPs can produce evanescent Bessel beams over a larger range than uniform surface impedances. NFPs can also generate Bessel patterns with various beamwidths, an important advantage over uniformly-fed electrically-large annular slot.

The chapter is organized as follows. In the next section, a uniform inductive surface impedance is designed to generate a desired evanescent Bessel beam. The inductive surface impedance is examined through full-wave simulation and the formation of the evanescent Bessel beam is verified. In the following section, a similar structure consisting of uniformly-fed, electrically-large annular slot in a metallic surface is theoretically and experimentally shown to generate Bessel beams. In the remainder of this chapter, a concentrically corrugated NFP is presented as a more effective and practical method for generating evanescent Bessel beams. The design procedure for such a plate is reviewed. The operation and design of the NFP is also verified through full-wave simulation. In the last section, the performance of a NFP that can generate an evanescent Bessel beam is compared with that of a simple coaxial probe and a NFP that generates a subwavelength Airy focal pattern with the same beamwidth. Finally, the flexibility offered by NFPs in producing evanescent Bessel beams with different properties is demonstrated.

5.2 Generating Evanescent Bessel Beams Using an Impedance Surface

Evanescent Bessel beams retain their transverse pattern as they attenuate in space. As a result, they also retain a constant wave impedance. This property suggests that a surface with a uniform impedance equal to that of the Bessel beam can be used to generate it. Our goal in this section is to find such a configuration. First, we need to compute the wave impedance of an evanescent Bessel beam. To do so, we apply Maxwell equations in cylindrical coordinates to a TM-polarized zeroth order Bessel beam of infinite transverse extent. The Bessel beam is assumed to decay along the z direction. The z component of the electric field of such a beam is then given by [65]:

$$E_z(\rho, z) = Ae^{(-\alpha_\circ z)}J_0(q_\circ \rho) \tag{5.1}$$

where, J_0 is the zero order Bessel function, $q_\circ$ determines the null-to-null beamwidth of the main lobe of the Bessel function, $\alpha_\circ = \sqrt{(q_\circ^2 - k_\circ^2)}$ determines the decay rate $(q_\circ > k_\circ)$, $k_\circ$ is the wavenumber in free space, and A is a normalization factor.

Gauss's law in cylindrical coordinates, $\nabla \cdot \mathbf{E} = 0$, can then be applied to the z component of electric field given by (5.1) to obtain the ρ component of the electric field:

$$E_\rho = A\alpha_\circ/q_\circ e^{(-\alpha_\circ z)}J_1(q_\circ \rho) \tag{5.2}$$

Throughout this chapter, only TM-polarized evanescent Bessel beams are considered $(E_\phi(\rho, z) = 0)$. The proposed procedures can be easily extended to other polarizations and higher orders of the Bessel beam.

By applying Faraday's law, $\mathbf{H} = -\nabla \times \mathbf{E}/j\omega_\circ \mu_\circ$, to the electric field given by
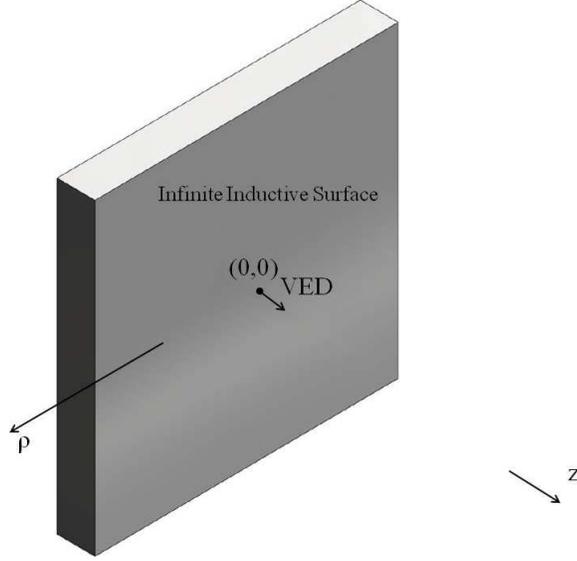
Figure 5.2: An infinitely wide inductive surface impedance excited by a vertical electrical dipole (VED) located at the origin.

(5.1) and (5.2), the magnetic field can be obtained:

$$\mathbf{H} = A j\omega_\circ \epsilon_\circ / q_\circ e^{(-\alpha_\circ z)} J_1(q_\circ \rho) \hat{\boldsymbol{\phi}} \tag{5.3}$$

From (5.2) and (5.3), the wave impedance of the evanescent Bessel beam can be computed:

$$\eta_s = -E_\rho(\rho, z)/H_\phi(\rho, z) = \frac{j\alpha_\circ}{\omega_\circ \epsilon_\circ} \tag{5.4}$$

Now, lets consider an infinite sheet with a surface impedance equal to η_s. In order to produce a TM polarized evanescent Bessel beam using this infinite sheet, the sheet needs to be excited by a TM source with cylindrical symmetry. An infinitely small vertical electric dipole (VED) is chosen for this purpose, as shown in Figure 5.2.

In order to verify that the configuration in Figure 5.2 produces an evanescent Bessel beam, we need to solve for the electromagnetic fields excited. Fortunately, the problem in Figure 5.2 is well-known. It has been a topic of many scientific communications and several numerical and analytical approaches to solving this problem

have been proposed (see [73–83] and references therein). Most of these works have focused on modeling the effect of the earth on communication links [73–76]. However, some works have also investigated the cylindrical surface wave excited in Figure 5.2 [77–81]. Such a surface wave has a Hankel function profile which can be used to form an evanescent Bessel beam.

The surface wave produced by the VED in Figure 5.2 can be found by examining the field scattered from the surface impedance, expressed as follows [83]:

$$E_z^s(\rho, z) = \frac{-Il}{8\pi\omega_\circ\epsilon_\circ} \int_{-\infty}^{+\infty} dk_\rho \frac{k_\rho^3}{k_z} H_0^{(2)}(k_\rho\rho)\Gamma e^{-jk_z z}, \tag{5.5}$$

where $E_z^s(\rho, z)$ is the z component of the scattered field, Il is the current and length of the VED, $H_0^{(2)}$ is the Hankel function of the second kind and zero order, and k_ρ and k_z are the ρ and z components of the wavevector, which are related to each other through the separation relation $k_\rho^2 + k_z^2 = k_\circ^2$. In equation (5.5), Γ is the Fresnel reflection coefficient of the infinite surface impedance:

$$\Gamma = \frac{k_z - j\alpha_\circ}{k_z + j\alpha_\circ}. \tag{5.6}$$

This coefficient exhibits poles at $|k_\rho| = q_\circ$ (when $k_z = -j\alpha_\circ = -j\sqrt{(q_\circ^2 - k_\circ^2)}$).

Equation (5.5) is commonly solved using asymptotic methods [83]. In these methods, the integral is approximated by its value along the steepest descent path in addition to the contribution due to singularities such as poles and branch-cuts [83]. The contribution due to the pole at $k_\rho = +q_\circ$ can be calculated using Cauchy's residue theorem. Using this theorem, the pole contribution is given by:

$$E_z^{s(pole)}(\rho, z) = \frac{-jIl}{2\omega_\circ\epsilon_\circ} q_\circ^3 H_0^{(2)}(q_\circ\rho)e^{-\alpha_\circ z} \tag{5.7}$$

which represents the surface wave supported by the configuration shown in Figure 5.2.

84

This surface wave dominates the near field of the surface impedance. As the distance from the surface impedance increases, the surface wave decays and the additional contributions to the total field given by (5.5) become comparable to the surface wave contribution [79–81]. It should be emphasized that the pole contribution given by (5.7), is an approximation of the total field in the near-field of the impedance surface and is not strictly valid at extremely small values of ρ. At these small radial distances, the fields need to be numerically computed using (5.5).

By comparing E_z of (5.7) and (5.1), one can see that the surface wave would resemble an evanescent Bessel beam if $H_0^{(2)}(q_\circ\rho)$ was replaced by $J_0(q_\circ\rho)$. But $J_0(q_\circ\rho)$ is closely related to $H_0^{(2)}(q_\circ\rho)$: $J_0(q_\circ\rho) = (H_0^{(2)}(q_\circ\rho) + H_0^{(1)}(q_\circ\rho))/2$. Here, $H_0^{(1)}(q_\circ\rho)$ is the zero order Hankel function of the first kind and represents a surface wave traveling towards $\rho = 0$. A surface wave going towards the origin can be generated by reflecting the surface wave given by (5.7) from a circular boundary, such as a perfect electric conductor (PEC) surface, to form a standing wave. If the PEC termination is placed at a distance $\rho = \rho_0$, where ρ_0 is a zero of $J_0(q_\circ\rho)$, the surface wave takes the form of $J_0(q_\circ\rho)$.

Keeping the arguments above in mind, the configuration in Figure 5.3 is proposed for generating a Bessel beam. In this configuration, the VED is replaced by an electrically small magnetic current loop M, whose field is equivalent. Such a loop can be easily realized with a coaxial aperture. The inductive sheet can be realized as a dielectric coated ground plane or corrugated metallic plate. The configuration is similar to that proposed in [78] for a different purpose. In [78], an inductive surface impedance terminated by matched loads was used to study the surface wave given by (5.7). In contrast, we abruptly terminate the inductive surface impedance with a PEC boundary to produce an evanescent Bessel beam.

To verify the ability of the configuration in Figure 5.3 to generate evanescent Bessel beams, the structure is simulated using the commercial electromagnetic finite
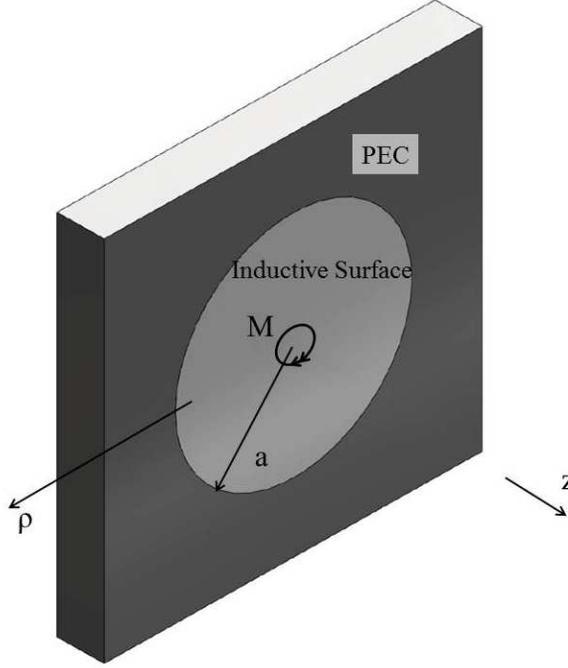
Figure 5.3: A circular inductive surface impedance terminated by a PEC surface. The structure is excited by a small magnetic current loop to form an evanescent Bessel beam.

element solver, Comsol Multiphysics. For this purpose, an evanescent Bessel beam with $q_\circ = 9k_\circ$ and $\alpha_\circ = 8.94k_\circ$ is considered. The operating frequency is set to $f = 1$ GHz, which corresponds to $\lambda_\circ = 0.3$ m. Given the Bessel beam properties above, a plate with reactance of $8.94j\eta_\circ$ is required, where $\eta_\circ$ is the characteristic impedance of free space. This inductive surface is chosen wide enough to ensure that the discontinuity at the edge, has a minimal effect on the main beam. The radius of the plate is chosen to be $a = 2.939\lambda_\circ$, which is very close to the zero of $J_0(q_\circ \rho)$ that occurs at $\rho_0 = 2.930\lambda_\circ$.

The full-wave simulation results are shown in Figure 5.4. In this figure, the E_z pattern produced by the plate at different distances is plotted along with the ideal Bessel beam given by equation (5.1). Throughout this chapter, the near-field pattern at each distance, z, is normalized with respect to its amplitude at $\rho = 0$. The close-up view of Figure 5.4 (a) shows that the pattern produced by the plate retains its shape

over a finite range (up to $z = 40$ mm $= 0.13\lambda_\circ$) and shows close agreement with the ideal evanescent Bessel beam. Beyond $z = 40$ mm $= 0.13\lambda_\circ$, the beam generated by the inductive surface starts to differ. This is expected since the surface wave, which forms the evanescent Bessel beam, dominates only close to the surface and becomes comparable to the additional contributions to the total field given by (5.5) at around $z = 40$ mm $= 0.13\lambda_\circ$.

The PEC surface shown in Figure 5.3 truncates the Bessel beam, and as a result limits its range. The PEC termination also causes edge diffraction which disturbs the near-field pattern close to the PEC termination ($\rho = \rho_0$), as shown in Figure 5.4 (b). The effect of edge diffraction is minimal close to the surface (see the pattern at $z = 10$ mm) and increases with the distance from the surface. At $z = 40$ mm, the edge diffraction is prominent. As a result, the evanescent Bessel beam retains its shape only close to the central axis of the surface impedance.

The results presented in Figure 5.4 verify the fact that the surface impedance shown in Figure 5.3 can generate an evanescent Bessel beam. However, the performance of this device needs to be improved in order for it to be suitable for practical applications. Specifically, it is relatively large and can form the evanescent Bessel beam only near its central axis over a limited range. To address these issues, the surface impedance needs to be redesigned taking its finite extent into account during the design process. The design procedure presented in this section is based on the properties of an ideal infinitely-wide evanescent Bessel beam and cannot be used to find a suitable surface impedance. Later in this chapter, we present NFPs, which can be designed to produce evanescent Bessel beams with a tailored truncation. By tailoring the truncation, one can minimize edge diffraction and improve device performance.
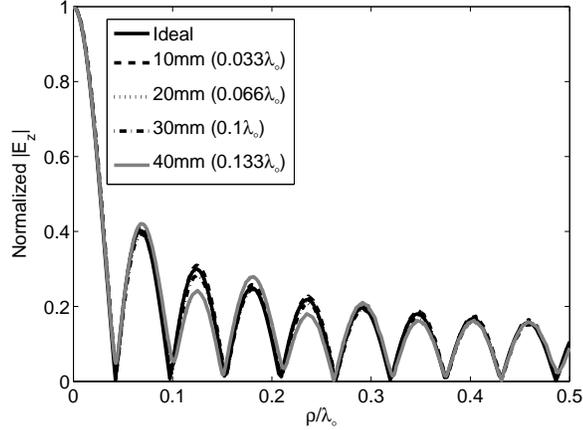
(a) Close-up view
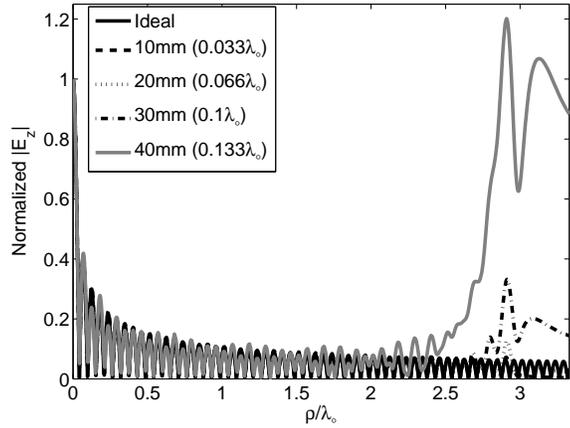
(b) Full-scale view

Figure 5.4: Normalized z-directed electric-field patterns at various axial distances from the inductive surface shown in Figure 5.3 along with the ideal Bessel beam given by (5.1). The close-up view in (a) shows the patterns produced by the inductive surface at different axial distances. The full-scale view in (b) illustrates the effect of edge diffraction on the performance of the inductive surface. The simulations are performed using Comsol Multiphysics.

5.3 Generating Bessel beams using electrically-large uniformly-fed annular slot

Before studying NFPs, it is worth noting that the proposed configuration of Figure 5.3 closely resembles the recently proposed structures that generate Bessel beams in the optical regime [84, 85]. In these works, an annular slot in a metallic plate, illuminated by radially [84] or linearly [85] polarized light, is shown to form Bessel beams. This configuration is analogous to the one studied in the previous section. The annular slot can be modeled as a magnetic current loop and the plasmonic metallic surface at optical frequencies acts as an inductive surface impedance. However, the radius of the annular slot reported in [84] was electrically large (7λ, where λ is at corresponding optical frequency). Such an electrically large radius is in contrast to the structure described in the previous section. In [84], the Bessel profile was attributed to excitation of surface plasmon polaritons on the surface of the metal at optical frequencies. In fact, it can be shown that an annular slot with electrically large radius generates a focal spot with Bessel profile, even at microwave frequencies where surface plasmon polaritons are not present.

To do so, we start with an analytical formulation for the electric field radiated by an annular slot (see Appendix A). The annular slot is then assumed to be large in order to approximate the analytical formulas and derive simple expressions. The approximate analytical formula predicts that a Bessel beam is formed by an electrically large slot. This analytical prediction and the generation of Bessel beam are then verified through full-wave simulation and experiment.

The annular slot configuration is shown in Figure 5.5. The inner and outer radius of the slot is assumed to be a and b, respectively. The annular slot is supported by a circular dielectric slab with radius R. The dielectric slab is terminated by a metallic rim and excited through a coaxial feed as shown in Figure 5.5 inset. This structure
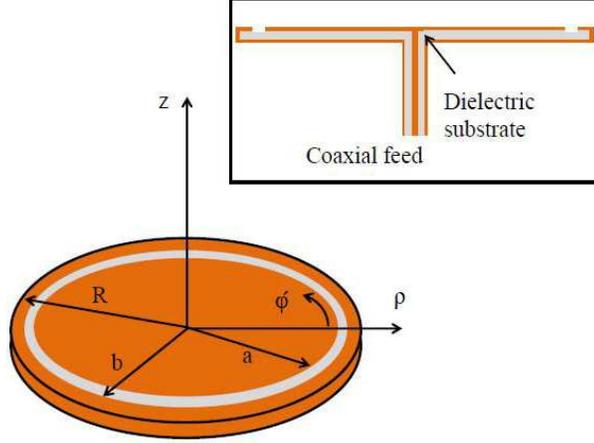
Figure 5.5: Schematic of an annular slot supported by a circular grounded dielectric slab. The inset shows the coaxial excitation.

can be modeled as a magnetic current frill whose z-directed electric field is given by (A.1):

$$E_z = \frac{1}{2\pi \ln(b/a)} \int_0^\pi \frac{e^{-jkr_a}}{r_a} - \frac{e^{-jkr_b}}{r_b} d\phi' \tag{5.8}$$

where k is the free space wavenumber, $r_a = \sqrt{z^2 + \rho^2 + a^2 - 2\rho a \cos(\phi')}$ and $r_b = \sqrt{z^2 + \rho^2 + b^2 - 2\rho b \cos(\phi')}$. Assuming the annular slot is large, or $z \ll a, b$ and $\rho \ll a, b$, (5.8) can be approximated by:

$$E_z \simeq \frac{1}{2\pi \ln(b/a)} \int_0^\pi \frac{e^{-jk(a-\rho\cos(\phi'))}}{a} - \frac{e^{-jk(b-\rho\cos(\phi')}}{b} d\phi' \tag{5.9}$$

The identity $J_0(k\rho) = \frac{1}{\pi} \int_0^\pi e^{jk\rho\cos(\phi')} d\phi'$ is then used to simplify (5.9) and obtain:

$$E_z \simeq \frac{1}{2\ln(b/a)} \{ \frac{e^{-jka}}{a} - \frac{e^{-jkb}}{b} \} J_0(k\rho) \tag{5.10}$$

where J_0 is the zero order Bessel function.

Equation (5.10) states that a large annular slot generates a Bessel field profile in the near field close to its axis ($\rho = 0$). According to the analysis above, the Bessel beam results from the inherent cylindrical symmetry of the large annular slot and, does not rely on excitation of surface plasmon polaritons or surface waves. However,

to generate a Bessel pattern with different beamwidth, the metallic plate should be replaced by a reactive surface impedance. In [86], a propagating Bessel beam was produced using a capacitive surface impedance. In the previous section and in [84], an inductive surface impedance was used to generate an evanescent Bessel beam.

The structure shown in Figure 5.5 is examined through full-wave simulation using Comsol Multiphysics. The simulation frequency is selected to be 17.35 GHz, corresponding to a 17.3 mm wavelength. Here, we consider an annular slot with inner and outer radii of $a = 70$ mm $= 4.05\lambda$ and $b = 70.4$ mm $= 4.07\lambda$. The annular slot is supported by a Rogers RO4003C dielectric substrate with 0.813 mm thickness (32 mil). The radius of the substrate is selected to be $R = 75$ cm.

The simulated electric-field pattern generated by the annular slot at $z = 10$ mm $= 0.58\lambda$ is plotted in Figure 5.6, and denoted as *Simulation*. For comparison, the theoretical near-field patterns predicted by (5.8) and (5.10) are also plotted. The theoretical and simulation results exhibit close agreement, thereby verifying the prediction that a large annular slot produces a Bessel beam.

In Figure 5.7, the simulated near-field patterns generated by the annular slot are plotted at various axial distances. The near-field patterns have an almost fixed shape, especially close to the axis where the assumption $\rho \ll a, b$ is valid. Furthermore, the full-width at half-maximum (FWHM) of the near-field patterns stays nearly constant. Specifically, the FWHM increased by 13.9% from 0.4874λ at $z = 10$ mm $= 0.58\lambda$ to 0.555λ at $z = 40$ mm $= 2.31\lambda$.

The structure was also fabricated and its electric field patterns were measured using a semi-rigid coaxial probe with inner and outer radii of 0.46 mm and 1.8 mm, respectively. The inner conductor of the probe was extended by 4.5 mm, to enhance the received signal. In the experiments, the distance between the outer conductor of the probe and the plate was considered as the axial distance, z. For instance, to measure the pattern at $z = 10$ mm, the probe was placed such that its outer
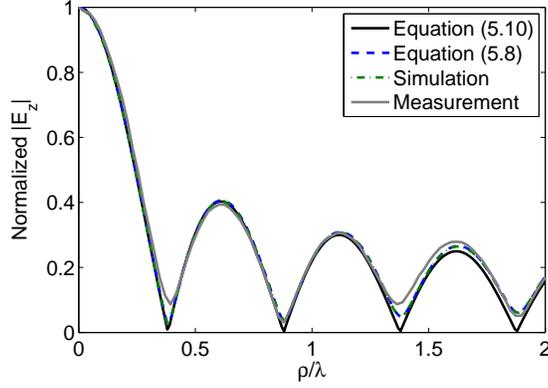
Figure 5.6: The *z*-directed electric-field patterns generated by the annular slot in Figure 5.5. The patterns are plotted at $z = 10$ mm.
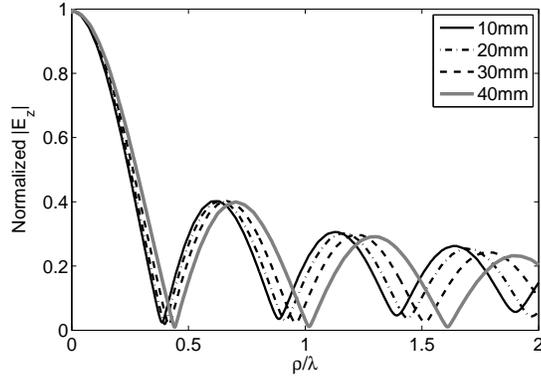
Figure 5.7: The *z*-directed electric-field patterns generated by the annular slot at various axial distances.

conductor was 10 mm away from the surface of the plate. The pattern measured in this manner is plotted in Figure 5.6, and labeled *Measurement*. The measured electric-field pattern exhibits close agreement with simulation and theoretical predictions. The slight difference between measured and simulated patterns can be attributed to the averaging effect of the scanning probe

5.4 Generating Evanescent Bessel beams using Near-field Plates

In the previous sections, a uniform inductive surface impedance was designed to generate evanescent Bessel beams. Such a configuration suffered from pronounced

edge diffraction which limited its performance. We also studied a uniformly-fed, electrically-large annular slot and proved its ability to generate Bessel beams close to its axis. However, this structure did not allow the beamwidth of the generated Bessel beam to be tailored. Furthermore, its dimensions were relatively large. In this section, we exploit the field tailoring capabilities of NFPs to generate evanescent Bessel beams. It is shown that a NFP allows the truncation of the beam to be customized, in order to mitigate the edge effects due to the finite beamwidth. It is also demonstrated that NFPs can be designed to generate evanescent Bessel beams with different beamwidths. These are the practical advantages offered by NFPs over the uniform impedance sheet and the large annular slot considered in the previous sections.

In order to generate evanescent Bessel beams using NFPs, the concentrically corrugated NFP introduced in the previous chapter is considered. This plate is redrawn in Figure 5.8 (a) for convenience. Similar to the previous chapter, the width, w, and the spacing, s, of the grooves are selected to be uniform while their depth, d_n, is varied to generate the desired subwavelength near-field pattern. In the previous chapter, we outlined a design procedure for this plate. Here, we will generalize this procedure so that it can be used for structures other than concentrically corrugated NFPs. For example, the proposed procedure can be used to design a dual configuration which consists of concentric rings of electric currents (current loops).

We can model the concentrically corrugated NFP as an array of annular slots in an infinite ground plane, as shown in Figure 5.8 (b). The slots are treated as ports with voltages V_n across them. In the design process, the voltages needed across the slots to form the desired pattern are found. Once the V_n are known, the wave impedances required to load the slots, η_n, are found [87]. The loaded slot array is then realized as a concentrically corrugated NFP [19]. Different groove depths are used as the loads. It should be noted that other methods such as lumped circuit elements (see next

chapter) or nanocircuit elements [24] at higher frequencies can also be used to realize the necessary loadings.

In the following, we first outline the procedure to find the required V_n and η_n to generate a desired focal pattern $E_z^{focal}(\rho)$. Next, we use this procedure to design two different concentrically corrugated NFPs: one generates a truncated evanescent Bessel focal pattern (Bessel beam NFP) and the other an Airy focal pattern (Airy pattern NFP). The Airy pattern NFP is used to highlight the advantages of Bessel beams over other near-field profiles.

5.4.1   Design Procedure

Let's assume that the array in Figure 5.8 (b) has N concentric slots with inner and outer radii a_n and b_n, respectively. First the complex voltages, V_n, needed to produce the desired focal pattern at $z = L$ are found. The concentric slots are modeled as an array of magnetic current rings (magnetic frills), radiating in free space. As in the previous chapter, the analytical expression for the field radiated by a frill in free space (see Appendix A) is used to relate the frills voltages to the desired near-field pattern:

$$2\sum_{n=1}^{N} V_n f_{nm}(z = L, \rho = \rho_m) = E_z^{focal}(\rho_m) \qquad (5.11)$$

where m is an integer from 1 to N, $E_z^{focal}(\rho)$ is the desired z-directed electric field sampled at $\rho_m = (m-1)s$, and $f_{nm}(z = L, \rho = \rho_m)$ is the z component of the electric field at $(z = L, \rho = \rho_m)$ produced by the nth frill given by (A.1). The amplitudes and voltages of the magnetic frills have been doubled as a result of image theory.

In the next step, the matrix equation (5.11) is solved to find V_n. Once the voltages, V_n, are known, they can be used to obtain the magnetic field at the slot locations. In contrast to the previous chapter, where we used the approximate equations of Appendix A, here we use the impedance matrix, Z_{NN}, of the slot array shown in Figure 5.8 (b) to find the magnetic field on the surface of the plate. The impedance
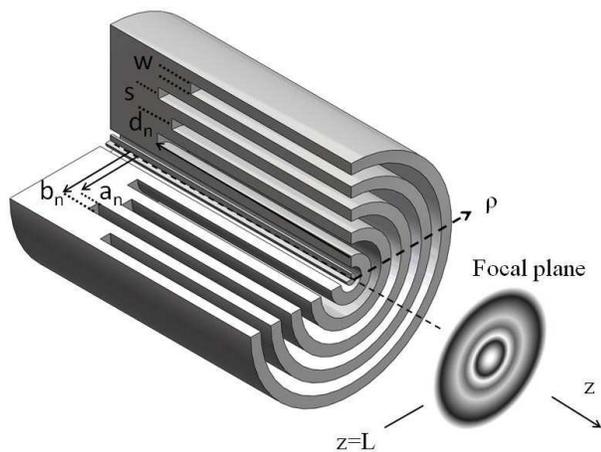
(a) Concentrically corrugated NFP
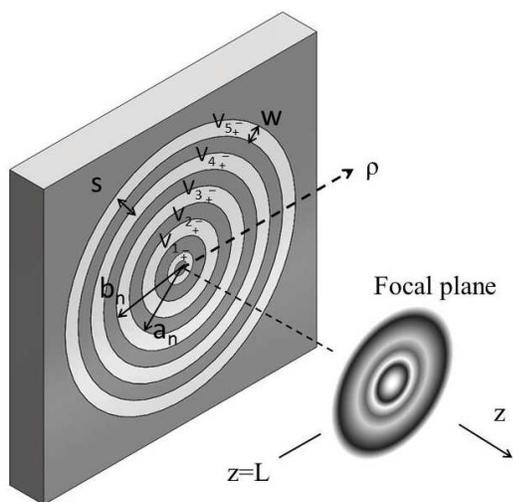
(b) Array of loaded annular slots

Figure 5.8: (a) A concentrically corrugated NFP. The width, w, and the spacing, s, are assumed to be uniform while the depths, d_n, are varied to produce the desired focal pattern. (b) An array of annular slots in an infinite ground plane used to design the concentrically corrugated NFP.

matrix, Z_{NN}, is found using Comsol Multiphysics. It relates the electric current into the slots (ports) to the slot voltages: $I_n = Z_{NN}^{-1}V_n$. The magnetic field at the slots is found from the current using Ampere's law: $H_\phi(z = 0, \rho = \rho) = I_n/(2\pi\rho)$. Combining these equations, we obtain:

$$H_\phi(z = 0, \rho = \rho_n) = Z_{NN}^{-1}V_n/(2\pi\rho_n) \tag{5.12}$$

where $\rho_n = \frac{a_n+b_n}{2}$.

In the last step, the loading wave impedances are found using

$$\eta_n = -E_\rho(z = 0, \rho = \rho_n)/H_\phi(z = 0, \rho = \rho_n) \tag{5.13}$$

where $E_\rho(z = 0, \rho)$ is the transverse electric field across the frills defined as $E_\rho(z = 0, \rho) = \frac{V_n}{\rho\ln(b_n/a_n)}$.

The required loading wave impedances are then realized by varying the groove depths of the concentrically corrugated NFP. In the next subsection, this design procedure is used to design two concentrically corrugated NFPs.

5.4.2 Bessel vs Airy Focal Pattern

We will first use the described procedure to design a concentrically corrugated NFP that generates a truncated evanescent Bessel beam. Bessel beams are commonly truncated using either a circular step function or a Gaussian function [65]. As discussed in [65], the Gaussian function truncates the Bessel beam gradually and the resulting beam more closely approximates an ideal Bessel beam. Therefore, we will consider a z-directed electric-field focal pattern with a Gaussian truncation:

$$E_z^{focal}(\rho) = Ae^{(-\rho^2/2\sigma^2)}J_0(q_\circ\rho) \tag{5.14}$$

96

where σ determines the fullwidth-at-half-maximum (FWHM) of the Gaussian trun-cating function. By changing σ, one can tailor the truncation of the Bessel beam to fit the requirements of an intended application.

In the design process, the slot array is assumed to have $N = 20$ frills (slots), spaced at $s = \lambda_\circ/40 = 7.5$ mm, with widths $w = \lambda_\circ/80 = 3.75$ mm. The inner and outer radii of the slots are selected to be $a_n = (2n-1)w$ and $b_n = (2n)w$, respectively. Given these parameters, an array is designed to produce the evanescent Bessel focal pattern with $q_\circ = 9k_\circ$, and $\sigma = 0.1066\lambda_\circ = 32$ mm at a focal plane $z = \lambda_\circ/10 = 30$ mm.

Following the design procedure, the voltages and loading impedances of the array of Figure 5.8 (b) are found. The loading impedances of the slots ($n = 2, ..., 20$) are realized by varying the depths, d_n, of the grooves. To do this, scattering from a linear, periodic array of grooves is used to compute the groove depths. The computed groove depths are shown in Table 5.1. It should be noted that the central slot ($n = 1$) represents the exciting coaxial aperture and therefore is not listed in Table 5.1. To simplify the notation, the NFP designed here is referred to as, Bessel beam NFP 1. The number 1 is used to distinguish the Bessel beam NFP designed here from the ones discussed in the next section.

For comparison purposes, a second concentrically corrugated NFP is designed to generate an Airy pattern of the following form:

$$E_z^{focal}(\rho) = A' \frac{J_1(q_\circ'\rho)}{q_\circ'\rho}, \tag{5.15}$$

where A' is a normalization constant, and $q_\circ' = 1.5934q_\circ$ is chosen such that a null-to-null beamwidth of $0.085\lambda_\circ$, equal to that of the Bessel beam, is obtained. The required groove depths for such a NFP are also listed in Table 5.1.

Table 5.1: The groove depth $(d_n/\lambda_\circ)$ of the NFPs designed to generate evanescent Bessel beam and Airy pattern.

Groove Index (n)	Bessel beam NFP 1	Airy pattern NFP
2	0.2383	0.2391
3	0.2396	0.2402
4	0.2379	0.2407
5	0.2401	0.2395
6	0.2374	0.2404
7	0.2404	0.2406
8	0.2367	0.2381
9	0.2406	0.2404
10	0.2357	0.2406
11	0.2408	0.2412
12	0.233	0.2403
13	0.2409	0.2405
14	0.2329	0.2406
15	0.241	0.2406
16	0.259	0.2407
17	0.2411	0.2409
18	0.2388	0.2413
19	0.2407	0.2424
20	0.2462	0.2453
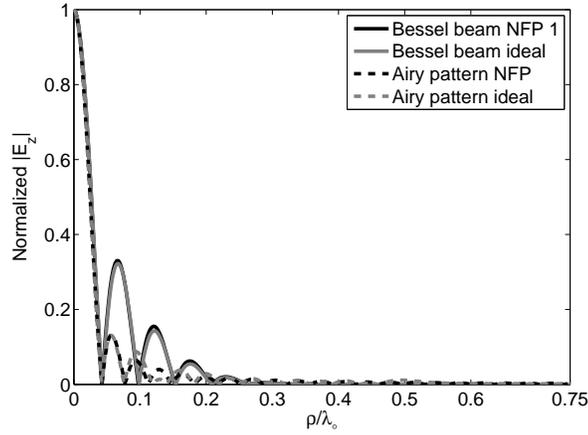
Figure 5.9: Normalized z-directed electric-field focal patterns ($z = L$). The graph *Bessel beam NFP 1* depicts the pattern produced by the Bessel beam NFP 1, while *Bessel beam ideal* shows the theoretical Bessel beam pattern defined by (5.14). The graph denoted as *Airy pattern NFP* depicts the pattern produced by the Airy pattern NFP, while *Airy pattern ideal* is the theoretical Airy pattern defined by (5.15). The simulations are performed using Comsol Multiphysics.

5.5 Full-wave Simulation

In this section, NFP designs are studied through full-wave simulation using Comsol Multiphysics. In the simulations, we initially assume the devices are lossless and made of PEC. Subsequently, the effect of losses is examined.

The focal pattern produced by the Bessel beam NFP 1 is shown in Figure 5.9. For comparison purposes, the pattern defined by (5.14) is also shown, and labeled as *Bessel beam ideal*. The close agreement between the two patterns validates the design procedure. Plotted in the same figure and labeled *Airy pattern NFP*, is the focal pattern produced by the Airy pattern NFP. The ideal Airy pattern defined by equation (5.15) is also plotted and labeled as *Airy pattern ideal*. As shown, the null-to-null beamwidth of the Bessel beam and the Airy pattern are the same.

The simulation results for the Bessel beam NFP 1 are reported at 1.00833 GHz which is 0.833% higher than the design frequency of 1.0 GHz. Similarly, the simulation results for the Airy pattern NFP are reported at 1.007965 GHz. These frequency

shifts can be attributed to the field expressions used to find the frill voltages (see Appendix A). However, the frequency shifts are lower than those reported in the previous chapter (1.195%), which indicates the higher accuracy of the method presented here over the one used in the previous chapter. Specifically, the magnetic field at the surface of NFP was found in the previous chapter using the approximate equations given in [51], while here we used the simulated impedance matrix, Z_{NN} of the slot array, to find the magnetic field. Since the full-wave simulation used to find Z_{NN} includes the fringing fields close to the frills, the magnetic field and the resulting impedances found in this chapter are more accurate than those presented in the previous chapter.

In order to show that the beam produced by the Bessel beam NFP 1 retains its transverse shape, the normalized patterns at various distances produced by it are shown in Figure 5.10. The patterns exhibit nearly the same shape and beamwidth from $z = 0.025\lambda_\circ = 7.5$ mm to $z = 0.25\lambda_\circ = 75$ mm. Closer to the plate, the pattern's shape differs from the desired Bessel profile due to the finite width of the grooves (surface discretization). The pattern also begins to differ from the Bessel profile around $z = 0.25\lambda_\circ = 75$ mm (for example see the pattern at $z = 90$ mm). This difference is due to the small propagating components radiated by the plate, which become comparable to the evanescent field beyond $z = 75$ mm.

For comparison purposes, the patterns produced by the Airy pattern NFP are shown in Figure 5.11 at the same distances from the plate. Neither the shape, nor the beamwidth are preserved in this case.

It is worth noting that the near-field patterns produced by the Bessel beam NFP 1 in Figure 5.10 are almost zero close to the plate's radius ($\rho = 0.5\lambda_\circ$). In other words, the effect of edge diffraction is minimal. This is in contrast to the performance of the uniform surface impedance studied in the previous section (see Figure 5.4). The edge diffraction has been suppressed by using a Gaussian truncation in the design of Bessel beam NFP 1. One should note that this could not be done using the uniform
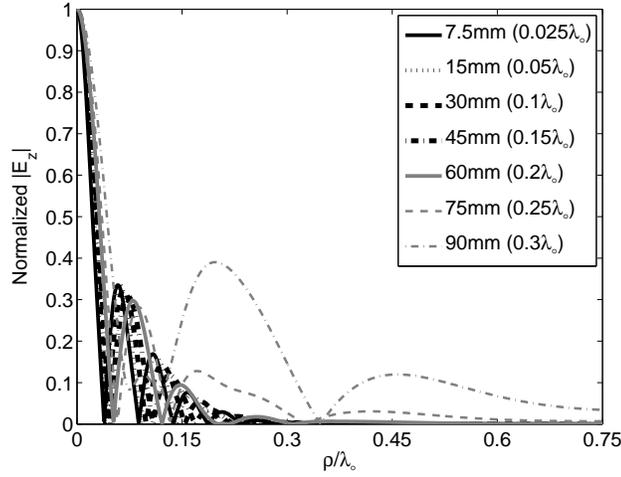
Figure 5.10: Normalized z-directed electric-field patterns at various axial distances from the Bessel beam NFP 1. The simulations are performed using Comsol Multiphysics.

surface impedance.

Figure 5.12 compares the variation of the beamwidth with respect to distance for the Bessel beam NFP 1 (solid black line) and the Airy pattern NFP (dashed black line). Although both plates generate a nearly identical FWHM at the focal plane ($z = 30$ mm), the behavior of their beam with distance differs significantly. The beam produced by Bessel beam NFP 1 has a FWHM which stays nearly constant, while the FWHM of the beam produced by the Airy pattern NFP changes dramatically. Specifically, from $z = 0.025\lambda_\circ = 7.5$ mm to $z = 0.3\lambda_\circ = 90$ mm, the FWHM of the Airy pattern changes by a factor of 10.53, from $0.034\lambda_\circ$ to $0.358\lambda_\circ$. Over the same distance, the FWHM of the Bessel beam changes by a factor of 1.95, from $0.044\lambda_\circ$ to $0.086\lambda_\circ$.

Also plotted in Figure 5.12 is the FWHM variation of the beam produced by a single coaxial aperture without corrugations (black dash dots). The FWHM of this beam changes from $0.037\lambda_\circ$ to $0.383\lambda_\circ$ (10.35 times) as the distance varies from $z = 7.5$ mm to $z = 90$ mm. This rapid variation of the shape and beamwidth of the beam produced by the coaxial probe severely limits its usefullness as a near-

101
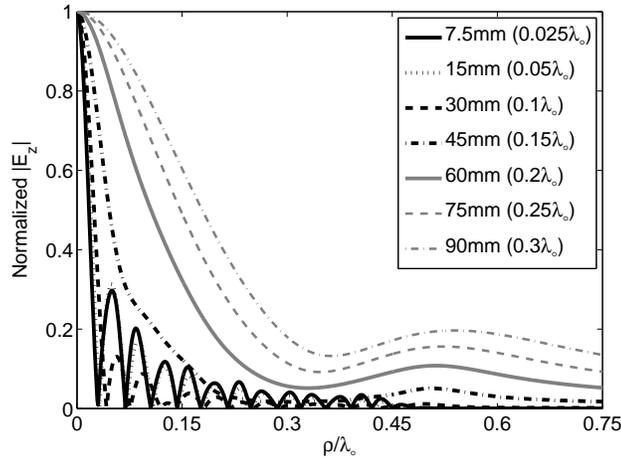
Figure 5.11: Normalized z-directed electric-field patterns at various axial distances from the Airy pattern NFP. The simulations are performed using Comsol Multiphysics.

field probe. The results depicted in Figure 5.12 suggest that a NFP designed to produce evanescent Bessel beams can overcome the shortcomings of conventional coaxial probes.

The ability to maintain a constant beamwidth is better understood by comparing the range of the different devices. Here, we define the range as the distance over which the intended FWHM increases by 50%. The intended FWHM is the beamwidth a NFP forms at its focal plane. For example, the Bessel beam NFP 1 obtains a FWHM = $0.0533\lambda_o$ at its focal plane, which becomes 50% wider over the range of 86.25 mm = $0.287\lambda_o$. The Airy pattern NFP obtains a FWHM = $0.0488\lambda_o$ at its focal plane. This beamwidth is retained over a range of 40.27 mm = $0.134\lambda_o$ which is 45.98 mm less than that of the Bessel beam NFP 1. The coaxial aperture obtains a FWHM = $0.0533\lambda_o$ (the intended resolution of the Bessel beam NFP 1) at $z = 13.27$ mm = $0.044\lambda_o$. This beamwidth becomes 50% larger over a range of 21.14 mm = $0.07\lambda_o$, which is 65.11 mm less than that of the Bessel beam NFP 1.

Figure 5.13 examines the performance of the Bessel beam NFP 1 with frequency. The FWHM at the operating frequency, 1.00833 GHz, is plotted versus axial dis-
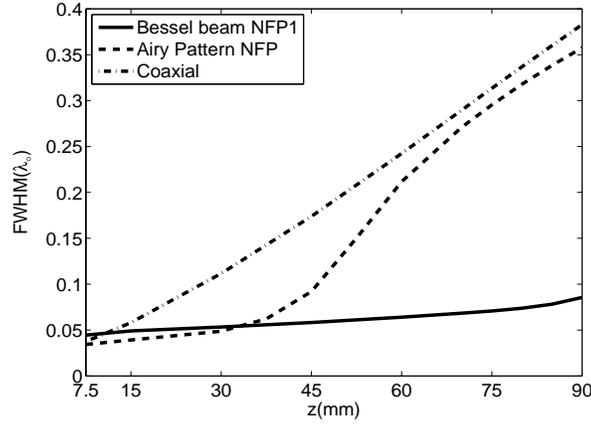
Figure 5.12: Variation of the z-directed electric field pattern beamwidth with distance for different devices.
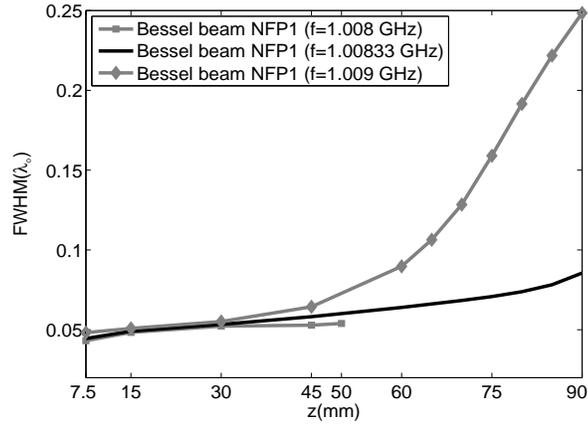
Figure 5.13: Effect of frequency variation on the performance of the Bessel beam NFP 1.

tance along with FWHM at lower and higher frequencies. At the lower frequency (1.008 GHz), the performance follows that at 1.00833 GHz up to approximately $z = 50$ mm. Beyond $z = 50$ mm, the side lobes of the patterns formed by the plate begin to become comparable to the main lobe. At the higher frequency (1.009 GHz), the structure also exhibits a similar performance to that at 1.00833 GHz up to approximately $z = 50$ mm. Beyond $z = 50$ mm, the beamwidth of the pattern formed by the structure starts to widen. Such a frequency response is consistent with the ones reported for the concentrically corrugated NFP in the previous chapter.
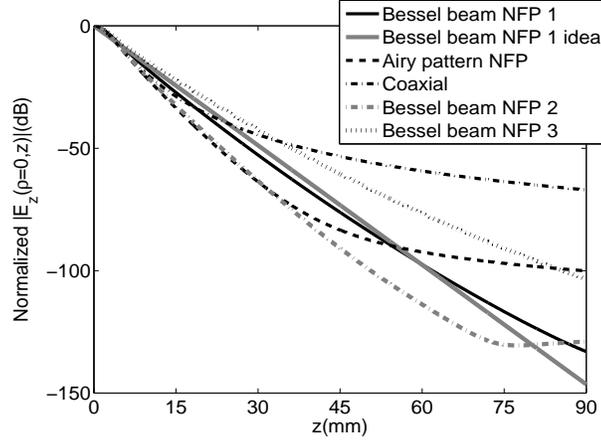
Figure 5.14: The maximum amplitude of the beam's main lobe, $|E_z(\rho = 0, z)|$, generated by different devices versus axial distance. Graphs are normalized to their maximum at $(\rho = 0, z = 0)$ and are shown in dB scale.

Figure 5.14 illustrates the evanescent nature of the beam produced by Bessel beam NFP 1. In this figure, the maximum amplitude of the beam's main lobe, $|E_z(\rho = 0, z)|$, is shown versus axial distance, z. The graph is normalized with respect to its maximum at $(z = 0, \rho = 0)$ and is shown on a dB scale. The beam produced by Bessel beam NFP 1 experiences a nearly exponential decay (see Figure 5.14). This is in close agreement with the exponential decay of an ideal Bessel beam with distance. The slight difference can be attributed to the fact that Bessel beam NFP 1 is truncated by a Gaussian function.

Figure 5.14 also shows the decay rate of the beam produced by the Airy pattern NFP. This beam exhibits a high rate of decay close to the surface which then tapers off with increasing axial distance. For larger distances ($z > 54.48$ mm), the field amplitude of the Airy pattern beam remains higher than that of the Bessel beam. This is because the Airy pattern beam has a dominant propagating spectrum, while the Bessel beam essentially does not have one.

For completeness, the decay rate of the simple coaxial aperture is also shown in Figure 5.14. Again, the field decays rapidly near the aperture but quickly levels off as the axial distance increases. The coaxial aperture does not have an enhanced

Table 5.2: Comparison of the characteristics of different Bessel beam NFPs.

Bessel beam NFP	N	FWHM $(z = L)$	Truncation (σ)	Range
1	20	0.053 λ	0.1066$\lambda_\circ$	86.25 mm
2	20	0.044 λ	0.1066$\lambda_\circ$	61.98 mm
3	20	0.068 λ	0.1066$\lambda_\circ$	81.92 mm
4	15	0.052 λ	0.07$\lambda_\circ$	59.33 mm
1(Lossy)	20	0.054 λ	0.1066$\lambda_\circ$	58.94 mm

evanescent spectrum [17] as do the Bessel beam and Airy pattern NFPs, and as a result its propagating spectrum quickly dominates the field profile.

A useful feature of NFPs is that they can sculpt the near-field. To show this, several other Bessel beam NFPs have also been designed and are listed in Table 5.2. In this table, the number of grooves, N, indicates the size of the plate, FWHM $(z = L)$ represents the intended resolution at the focal plane, σ denotes the width of the Gaussian truncation, and the range is a measure of the NFP's ability to retain its intended resolution. For comparison purposes, we have also included the characteristics of Bessel beam NFP 1 in this table.

The second design listed in Table 5.2 is Bessel beam NFP 2. This plate is designed to produce an evanescent Bessel beam with narrower beamwidth compared to Bessel beam NFP 1. The beamwidth produced by Bessel beam NFPs can be modified by changing $q_\circ$. As an example, Bessel beam NFP 2 is designed with $q_\circ = 11k_\circ$ instead of $q_\circ = 9k_\circ$ for Bessel beam NFP 1. The FWHM of the beam produced by Bessel beam NFP 2 is plotted versus distance in Figure 5.15 with a dash-dot grey line. The beamwidth variation for this NFP is only shown up to $z = 65$ mm. Beyond $z = 65$ mm, the sidelobes become comparable to the main lobe. For comparison purposes, we have also shown the beamwidth variation of Bessel beam NFP 1 (solid black line). It can be seen that Bessel beam NFP 2 generates a narrower beam. However, this
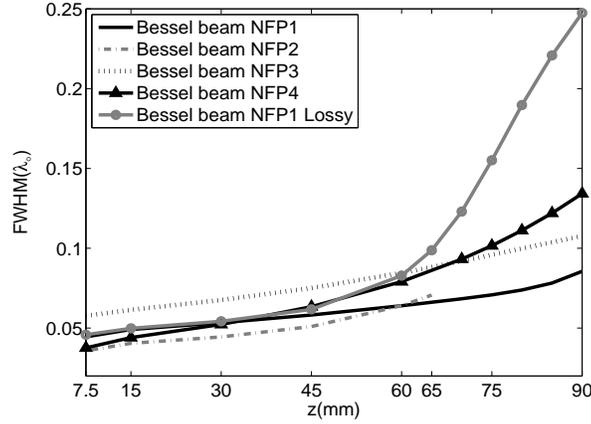
Figure 5.15: Variation of the z-directed electric field pattern beamwidth with distance for different Bessel beam NFPs.

narrow beamwidth is achieved at the cost of a shorter range: 61.98 mm $= 0.207\lambda_\circ$ compared to 86.25 mm $= 0.287\lambda_\circ$ for Bessel beam NFP 1. The beam produced by Bessel beam NFP 2 also exhibits a higher decay rate than Bessel beam NFP 1, as shown in Figure 5.14. This is expected since the decay rate is determined by $\alpha_\circ = \sqrt{(q_\circ^2 - k_\circ^2)}$.

The next example listed in Table 5.2 is Bessel beam NFP 3, which is designed to produce an evanescent Bessel beam with wider beamwidth compared to that of Bessel beam NFP 1. In this design, $q_\circ = 9k_\circ$ of Bessel beam NFP 1 was reduced to $q_\circ = 7k_\circ$. The performance of this plate is plotted in Figure 5.15 with a dotted line. The range for this plate is 81.92 mm $= 0.274\lambda_\circ$ which is comparable to 86.25 mm $= 0.287\lambda_\circ$ for Bessel beam NFP 1. On the other hand, this beam exhibits a lower decay rate, as shown in Figure 5.14.

In the next example, the effect of Gaussian truncation on the performance of Bessel beam NFPs is examined. Bessel beam NFP 4 is designed to produce an evanescent Bessel beam truncated by a narrower Gaussian function than Bessel beam NFP 1. This is done by decreasing $\sigma = 0.1066\lambda_\circ$ of Bessel beam NFP 1 to $\sigma = 0.07\lambda_\circ$. The beamwidth of the desired Bessel function is kept the same: $q_\circ = 9k_\circ$. The beamwidth variation of the beam produced by this plate is shown in Figure 5.15

106

with a solid black line marked with triangles. This beam exhibits larger beamwidth variation than Bessel beam NFP 1. Specifically, the range of Bessel beam NFP 4 is 59.33 mm = $0.198\lambda_\circ$ which is 26.92 mm less than 86.25 mm = $0.287\lambda_\circ$ for Bessel beam NFP 1. This larger variation is expected since an evanescent Bessel beam truncated by a narrower function diffracts more with distance. On the other hand, a lower number of grooves is needed to generate such a beam ($N = 15$ for Bessel beam NFP 4 compared to $N = 20$ for Bessel beam NFPs 1, 2, and 3). Therefore, a trade-off exists between the range, and the size of the NFP.

Finally, to examine the effect of losses on the performance of Bessel beam NFPs, Bessel beam NFP 1 ($q_\circ = 9k_\circ$ and $\sigma = 0.1066\lambda_\circ$) is resimulated in Comsol Multiphysics. The perfect electric conductor boundaries of the earlier examples are replaced with copper. The performance of this plate is plotted in Figure 5.15 with a solid grey line marked with circles. The effect of losses is negligible close to the plate and becomes more pronounced farther from the plate. Nevertheless, its range is 58.94 mm = $0.196\lambda_\circ$, which is still significantly larger than 21.14 mm = $0.07\lambda_\circ$ for the coaxial aperture.

5.6 Conclusion

This chapter highlighted a NFP's ability to tailor the electromagnetic near field by presenting a concentrically corrugated NFP capable of producing evanescent Bessel beams. In addition, a generalized design approach was outlined that can be used for various NFP configurations. The performance of the designed NFPs was studied through full-wave simulation. It was shown that the evanescent Bessel beam produced by the NFP retained a nearly constant shape and beamwidth over a near-field distance. The FWHM of the beam produced by the Bessel beam NFP changed from $0.044\lambda_\circ$ to $0.086\lambda_\circ$ (1.95 times larger) as the distance from the plate was varied from $z = 0.025\lambda_\circ = 7.5$ mm to $z = 0.3\lambda_\circ = 90$ mm. Over the same distance, the FWHM

of the beam produced by the Airy pattern NFP and the one produced by a coaxial aperture increased by 10.53 and 10.35 times, respectively. NFPs capable of producing evanescent Bessel beams, will find application in near-field imaging/probing systems, high-resolution data storage, and medical devices that focus electromagnetic fields.

CHAPTER VI

Planar Near-field Plates

6.1 Introduction

In the previous chapter, concentrically corrugated near-field plates (NFPs) were developed to generate evanescent Bessel beams. Evanescent Bessel beams retain a nearly constant subwavelength beamwidth over a near-field distance and thus, can be beneficial in applications such as high resolution imaging, biomedical devices, and high density data storage. However, they have been difficult to produce, and thus have not found their place in practice. Results from previous chapter proved how a NFP's tailoring capabilities pave the way for an effective, yet simple method for generating evanescent Bessel beams.

While concentrically corrugated NFPs demonstrated promising results in tailoring the electromagnetic near field, they were costly to fabricate. They had to be machined and could not be implemented using low-cost methods such as printed circuit board (PCB) techniques. This drawback hinders their integration with electronic devices. In this chapter, we present planar NFPs that can be fabricated in standard PCB technology.

The planar NFP topology considered in this chapter is shown in Figure 6.1. It consists of annular slots in a metallic surface supported by a circular grounded dielectric substrate. The dielectric substrate is truncated with a metallic rim. The plate
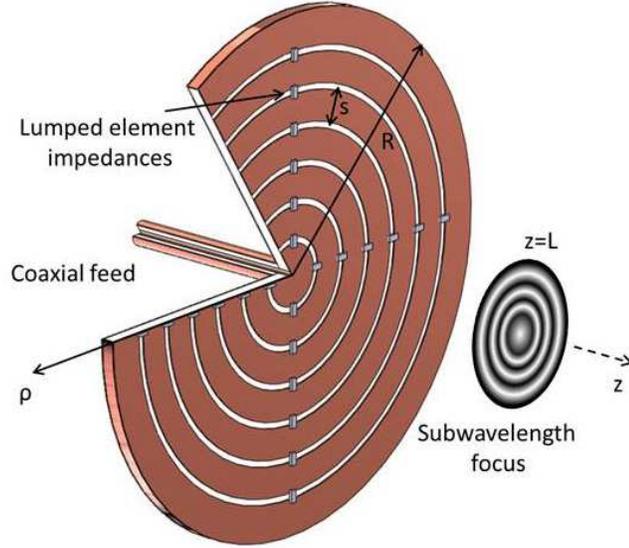
Figure 6.1: A planar NFP which consists of concentric annular slots on a circular grounded dielectric slab. The plate is excited through a coaxial cable and its rim is short circuited. The slots are loaded with lumped element impedances designed to produce a prescribed subwavelength focal pattern.

is excited through a centrally located coaxial connector and the slots are loaded with lumped-element impedances. The impedances are chosen to produce desired focal patterns.

This chapter is organized as follows. In the next section, the design procedure for a planar NFP is detailed. In the subsequent section, planar NFPs are designed and studied through full-wave simulation. In the final section, the designed plates are fabricated and measured. Planar NFPs that can produce both evanescent Bessel beams and subwavelength Airy patterns are experimentally demonstrated. The performance of the plates are also contrasted against an unloaded plate, to highlight their near field tailoring capabilities.

6.2 Design Procedure

The goal of the design procedure is to find the loading impedances needed to produce a desired focal spot. Lets consider a planar NFP with radius $\rho = R$ and

110
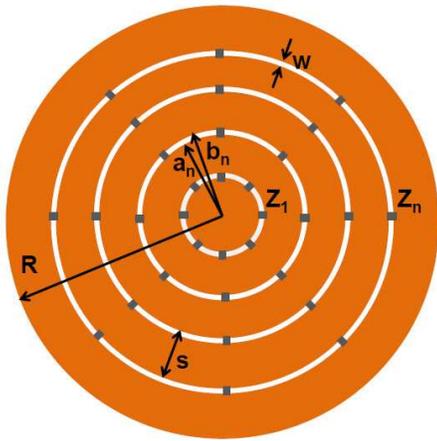
(a) Front view of planar NFPs.
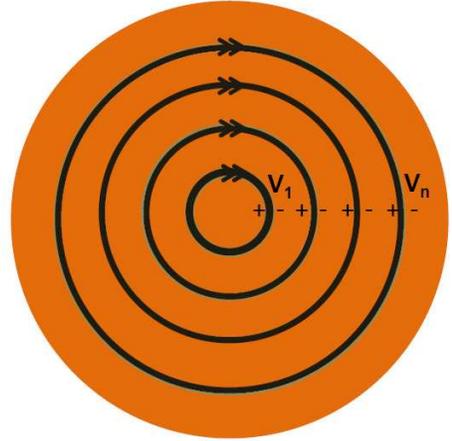
(b) Array of magnetic current frills.

Figure 6.2: (a) Front view of the planar NFP depicted in Figure 6.1. (b) The array of magnetic current frills with voltages V_n across them used to model the planar NFP in the design procedure.

N circular slots, as shown in Figure 6.2 (a). The annular slots have inner and outer radii a_n and b_n, respectively. The width w and spacing s of the slots are assumed to be uniform, and the focal plane is located at $z = L$.

In the first step of the design procedure, the annular slots are modeled as magnetic current frills with voltage, V_n, across them, as shown in Figure 6.2 (b). As in the previous chapters, the analytical formulas derived for the fields radiated by a magnetic current frill are used to relate the voltages V_n to the prescribed z-directed electric-field focal pattern (see Appendix A):

$$2\sum_{n=1}^{N} V_n f_{nm}(z = L, \rho = \rho_m) = E_z^{focal}(\rho_m) \tag{6.1}$$

where $m = 1 \cdots N$ and $n = 1 \cdots N$, $f_{nm}(z = L, \rho = \rho_m)$ is the z component of the electric field at $\rho_m = (m-1)s$ due to the nth magnetic current frill, $E_z^{focal}(\rho_m)$ is the desired z-directed electric-field focal pattern. The matrix equation (6.1) is solved for the voltages V_n, given a prescribed focal pattern.

In the next step, the annular slots are modeled as ports in the finite element

111

commercial electromagnetic solver, Ansys HFSS, to obtain their impedance matrix Z_{N+1N+1}. The $N+1$th row and column of Z_{N+1N+1} represents the exciting coaxial connector. For the time being, we will ignore the $N+1$th row and column of Z_{N+1N+1} and consider only Z_{NN}. Later in subsection 6.3.1, we will use Z_{N+1N+1} to relate voltages on the slots to the the incident voltage on the coaxial connector. Knowing the voltages, V_n, from step 1, the impedance matrix, Z_{NN}, can be used to find the currents, I_n, across the slots:

$$I_n = Z_{NN}^{-1} V_n \qquad (6.2)$$

In the final step, the ratio of voltage to current across each slot is computed to find the required loading impedances, Z_n:

$$Z_n = \frac{V_n}{I_n} \qquad (6.3)$$

The required impedances, Z_n, are predominantly reactive. Hence, their resistive part can be neglected, as in the previous chapters. The required reactance of each slot is then realized by uniformly placing M lumped element inductors/capacitors across each slot, as shown in Figure 6.1. The inductors/capacitors values can be computed by noting that the lumped elements across each slot are in parallel with each other:

$$L_n = \frac{MX_n}{\omega}$$
$$C_n = \frac{1}{\omega MX_n} \qquad (6.4)$$

where $X_n = Im\{Z_n\}$ and ω is the angular frequency. It should be noted that the discontinuities introduced by the lumped impedances cause fringing fields around the elements. These fringing fields slightly change the overall impedance of each slot. To characterize the effect of fringing, a linear slot is considered in a separate scattering simulation. The linear slot is backed by the same grounded dielectric slab and loaded

with the lumped element impedances computed using (6.4). The width of the linear slot is assumed to be w and its length is $2\pi b_n/M$. A plane wave is then used to excite the linear slot. From the reflection coefficient, the overall impedance of the slot, including the effect of the fringing fields, can be computed. Such simulations are used to adjust the values of the calculated lumped element impedances to compensate for the effect of fringing.

6.3 Simulation Results

In this section, planar NFPs designed in the previous section are examined through analytical and numerical analysis. First, we analytically study the planar NFP to obtain expressions for the voltages across its annular slots when they are loaded with the elements computed using (6.4). The voltages are then used to analytically predict the near-field pattern formed by the planar NFP, using the formulas given in Appendix A. Next, we examine the designed plates in full-wave simulation. It will be shown that patterns produced in full-wave simulation are in close agreement with analytical prediction, thereby verifying the design procedure.

6.3.1 Analytical Analysis

When the planar NFP is loaded solely with reactive impedances X_n (neglecting the real parts), the voltages induced across the annular slots, V'_n, slightly differ from the design values, V_n. In order to accurately predict the focal patterns produced by the NFPs with reactive impedances, X_n, we analytically solve for the voltages V'_n. We follow the procedure outlined in [87] and assume the structure is excited by a coaxial connector with voltage $V'_{N+1} = V_{exc}$, where V_{exc} is an arbitrary value, determined by the incident power. Then, we solve for the voltages V'_n as a function of V_{exc}. To do so, we first note that V'_n are related to I'_n through the matrix impedance, Z_{N+1N+1}, as follows:

$$
\begin{bmatrix} I_1' \\ \vdots \\ I_N' \\ I_{exc} \end{bmatrix} = Z_{N+1N+1}^{-1} \begin{bmatrix} V_1' \\ \vdots \\ V_N' \\ V_{exc} \end{bmatrix} \tag{6.5}
$$

The loading reactances, X_n, also relate the voltages, V_n', and currents, I_n'. There-fore,

$$
\begin{bmatrix} V_1'/jX_1 \\ \vdots \\ V_N'/jX_N \end{bmatrix} = \begin{bmatrix} Y_{11} \; Y_{12} \cdots Y_{1N+1} \\ Y_{21} \; Y_{22} \cdots Y_{2N+1} \\ \vdots \quad \ddots \quad \vdots \\ Y_{N1} Y_{N2} \cdots Y_{NN+1} \end{bmatrix} \begin{bmatrix} V_1' \\ \vdots \\ V_N' \\ V_{exc} \end{bmatrix} \tag{6.6}
$$

where Y_{ij} are the elements of $Y_{N+1N+1} = Z_{N+1N+1}^{-1}$. The right hand side of (6.6) can be separated into two parts:

$$
\begin{bmatrix} V_1'/jX_1 \\ \vdots \\ V_N'/jX_N \end{bmatrix} = \begin{bmatrix} Y_{11} \; Y_{12} \cdots Y_{1N} \\ Y_{21} \; Y_{22} \cdots Y_{2N} \\ \vdots \quad \ddots \quad \vdots \\ Y_{N1} Y_{N2} \cdots Y_{NN} \end{bmatrix} \begin{bmatrix} V_1' \\ \vdots \\ V_N' \end{bmatrix} + V_{exc} \begin{bmatrix} Y_{1N+1} \\ \vdots \\ Y_{NN+1} \end{bmatrix} \tag{6.7}
$$

The equation above is then rearranged to find V_n':

$$
\begin{bmatrix} V_1' \\ \vdots \\ V_N' \end{bmatrix} = V_{exc} \begin{bmatrix} 1/jX_1 - Y_{11} \cdots & -Y_{1N} \\ -Y_{21} & \cdots & -Y_{2N} \\ \vdots & \ddots & \vdots \\ -Y_{N1} & \cdots 1/jX_1 - Y_{NN} \end{bmatrix}^{-1} \begin{bmatrix} Y_{1N+1} \\ \vdots \\ Y_{NN+1} \end{bmatrix} \tag{6.8}
$$

Once V_n' are known, fields at all points in space using can be found (12), (20), (21) in [51].

6.3.2 Full-wave Simulation

In this subsection, two different planar NFPs are studied through full-wave simulation. We consider NFPs with $N = 6$ slots, which are terminated by a metallic rim at $R = 42$ mm. Throughout this chapter, the wavelength is assumed to be $\lambda = 300$ mm, corresponding to an operating frequency of 1.0 GHz. The slots are selected to be $w = 0.4$ mm wide and $s = 6$ mm $= 0.02\lambda$ apart. The inner and outer radii of the slots are chosen to be $a_n = ns - w$ and $b_n = ns$. The focal plane is at $L = 20$ mm $= \lambda/15$. The substrate is a 0.813 mm (32 mil) thick Rogers RO4003C. The coaxial excitation has inner and outer radii of 0.635 mm and 2.05 mm respectively, which correspond to the dimensions of a standard SMA connector.

We will consider two different focal patterns. A truncated, subwavelength Bessel focal pattern:

$$E_z^{focal}(\rho) = e^{(-\rho^2/2\sigma^2)} J_0(q\rho), \tag{6.9}$$

where J_0 is the zeroth-order Bessel function, q determines the null-to-null beamwidth of the main lobe of the Bessel function, and σ determines the full width at half-maximum (FWHM) of the Gaussian truncating function. It was shown in the previous chapter that a NFP designed to produce such a focal pattern forms an evanescent Bessel beam that retains its shape and beamwidth over a near-field distance. We will refer to this plate as a Bessel beam NFP. For comparison purposes, we also consider a plate that can produce an Airy focal pattern:

$$E_z^{focal}(\rho) = \frac{J_1(q'\rho)}{q'\rho}, \tag{6.10}$$

where J_1 is the first order Bessel function and q' determines the null-to-null beamwidth of the focal pattern. We will refer to this plate as Airy pattern NFP.

The first NFP is designed to produce a Bessel focal pattern with $q = 7.6k$, where k is the free space wavenumber. This focal pattern is truncated by a Gaussian function

with $\sigma = 23$ mm $= 0.076\lambda$. We will refer to this plate as Bessel beam NFP 1. The plate was designed using the procedure outlined in the previous section, and its loading impedances are listed in Table 6.1. Each loading impedance is realized using $M = 16$ lumped element impedances computed using (6.4). The values of the calculated impedances are adjusted to account for the effect of fringing fields. They are also listed in Table 6.1.

Table 6.1: The impedance values required to load the designed planar NFPs with the corresponding lumped inductors/conductrs used to realize them.

	Bessel beam NFP 1		Airy pattern NFP	
n	$X_n(\Omega)$	Lumped element	$X_n(\Omega)$	Lumped element
1	12.07	30.54nH	14.48	36.65nH
2	7.13	17.83nH	6.89	17.24nH
3	0.9	1.87nH	1.62	3.73nH
4	−6.7	1.44pF	30.64	77.5nH
5	10.57	26.31nH	2.51	5.85nH
6	4.71	11.38nH	0.86	1.54nH

The second plate was designed to produce an Airy pattern with $q' = 12.11k$, resulting in a focal pattern with null-to-null beamwidth of $\lambda/10$, equal to that of Bessel beam NFP 1. The required impedances of this plate as well as the loading inductors/capacitors used to realize them are also listed in Table 6.1.

The Bessel beam NFP 1 was simulated using HFSS. The normalized, z-directed electric-field focal pattern produced by this plate is plotted in Figure 6.3, and labeled *Ideal Bessel beam NFP 1 (simulation)*. The focal pattern produced by this plate was also computed using the voltages obtained using (6.8). The computed focal pattern is also shown in Figure 6.3, and labeled *Ideal Bessel beam NFP 1 (computed)*. The close agreement between the two graphs verifies the design procedure presented in the previous section. Plotted in Figure 6.3 and labeled *Ideal Airy pattern NFP (simulation)* is the focal pattern produced by the Airy pattern NFP using the lumped element impedances listed in Table. 6.1. The focal pattern of this plate has also been com-
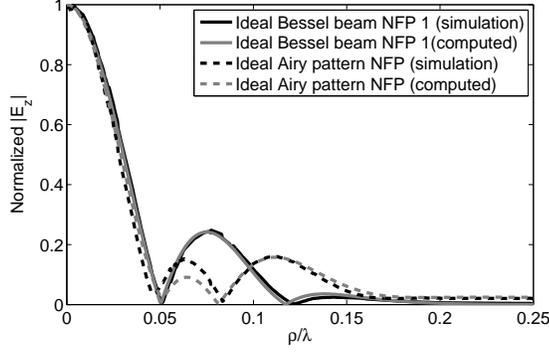
Figure 6.3: Normalized *z*-directed electric-field focal patterns. The focal pattern produced by the Bessel beam NFP 1 with lumped element impedances listed in Table. 6.1 is labeled as *Ideal Bessel beam NFP 1 (simulation)*. The focal pattern computed for this plate using the voltages obtained by (6.8) is labeled as *Ideal Bessel beam NFP 1 (computed)*. The graph *Ideal Airy pattern NFP (simulation)* represents the focal pattern produced by the Airy pattern NFP with lumped element impedances listed in Table. 6.1. The focal pattern computed for this plate using the voltages obtained by (6.8) is labeled as *Ideal Airy pattern NFP (computed)*.

puted using the voltages obtained using (6.8). The computed focal pattern is labeled *Ideal Airy pattern NFP (computed)*. Again, the two graphs exhibit close agreement. As expected, the focal patterns produced by *Bessel beam NFP 1* and *Airy pattern NFP* have approximately the same null-to-null beamwidths. It should be noted that the results for Bessel beam NFP 1 and Airy pattern NFP are reported at 1.004 GHz and 0.996 GHz, respectively. These slight frequency shifts can be attributed to the approximations made in deriving the analytical equations in Appendix A. Similar frequency shifts have also been reported for NFPs studied in the previous chapters.

While the focal patterns in Figure 6.3 verify the design and operation of the planar NFP, it is important to note that the exact impedance values listed in Table 6.1 may not be available in practice. To include fabrication constraints, the NFPs were simulated using practical inductor and capacitor values. Inductors and capacitors were selected from the Coilcraft 0402HP series and the Murata GJM155C series, respectively. Using the *S*-parameters provided by the manufacturers, the inductors

117

and capacitors were simulated in the Agilent ADS Microwave circuit simulator to find their values at 1.0 GHz. The nominal values of the inductors and capacitors as well as their values and quality factors (Q) at 1.0 GHz are listed in Table 6.2.

Using the inductors/capacitors values at 1.0 GHz listed in Table 6.2, the Bessel beam NFP 1 and Airy pattern NFP were resimulated in HFSS. Their focal patterns are shown in Figure 6.4 and labeled *Practical Bessel beam NFP 1 (simulation)* and *Practical Airy pattern NFP (simulation)*, respectively. For comparison purposes, the patterns produced by the plates with ideal inductor and capacitor values listed in Table 6.1 are also shown. It should be noted that the results for practical NFPs are reported at 0.995 GHz and 0.982 GHz, respectively. These small frequency shifts can be attributed to the slight difference between the practical component values listed in Table. 6.2 and the theoretical ones in Table 6.1.

Figure 6.4 demonstrates close agreement between the patterns produced by the plates loaded with ideal and practical impedance values. This close agreement suggests that planar NFPs can be fabricated to produce prescribed focal patterns despite practical tolerances. In the next section, the designed NFPs are fabricated and their performance is examined experimentally. In the rest of this section, the performance of the practical NFPs is studied through full-wave simulation. From this point forward, *Bessel beam NFP 1* and *Airy pattern NFP* refer to plates loaded with practical impedance values (Table 6.2).

As was shown in the previous chapter, a beam with a Bessel pattern given by (6.9) nearly retains its shape and beamwidth over a near-field distance. To examine this property, the electric-field patterns produced by *Bessel beam NFP 1* at various axial distances, z, are shown in Fig 6.5. The plate produces a subwavelength beam with a nearly constant shape and beamwidth from $z = 10$ mm $= \lambda/30$ to $z = 60$ mm $= \lambda/5$. At distances less than $z = 10$ mm, the pattern varies from the desired Bessel pattern because of the plate's discretization. Beyond $z = 60$ mm, the pattern starts to

Table 6.2: The inductors/capacitors used to load the practical planar NFPs with their corresponding values at 1.0 GHz. The inductors are selected from 0402HP Coilcraft collection while the capacitors are selected from Murata GJM155C collection. The only exception is 1.9 nH which is selected from 0402CS Coilcraft collection.

n	Bessel beam NFP 1			Airy pattern NFP		
	nominal	at 1.0 GHz	Q	nominal	at 1.0 GHz	Q
1	30nH	31.31nH	67.1	36nH	37.51nH	62.9
2	18nH	18.53nH	58.2	16nH	16.46nH	63.2
3	2nH	2.01nH	59.3	3.6nH	3.61nH	70.6
4	1.5pF	1.53pF	368	68nH	75.06nH	58.1
5	27nH	27.78nH	69	5.6nH	5.64nH	78.9
6	11nH	11.21nH	77.1	1.9nH	1.91nH	37

differ from the desired Bessel shape due to the truncation of the Bessel focal pattern. The electric-field patterns produced by the *Airy pattern NFP* are shown in Fig 6.6. Neither shape nor the beamwidth are preserved in this case.

The ability of *Bessel beam NFP 1* to retain its beamwidth is evident from a plot of FWHM vs. axial distance, shown in Figure 6.7. The FWHM of the beam produced by the *Airy pattern NFP* as well as a plate with the same dimensions without loading impedances (unloaded plate) are shown. The FWHM of the beam produced by the *Bessel beam NFP 1* stays almost fixed while the beamwidth of the *Airy pattern NFP* and the unloaded plate changes dramatically with axial distance. The *Bessel beam NFP 1* produces an FWHM $= 0.0554\lambda$ at $z = 10$ mm which becomes FWHM $= 0.1044\lambda$ at $z = 60$ mm: 1.88 times wider. Over the same distance, the FWHM of the unloaded plate changes from FWHM $= 0.04492\lambda$ to FWHM $= 0.2128\lambda$: 4.74 times wider. The FWHM of the *Airy pattern NFP* is only shown up to $z = 40$ mm, since its sidelobe becomes comparable to the main lobe around $z = 40$ mm, as shown in Figure 6.6. Its FWHM changes from 0.04788λ to 0.1308λ (2.73 times larger), only over the distance from $z = 10$ mm to $z = 40$ mm.

In order to further illustrate the ability of planar NFPs to produce beams with
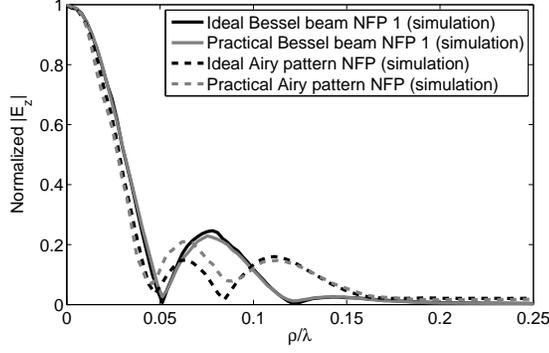
Figure 6.4: Normalized z directed electric-field focal pattern. The graphs *Ideal Bessel beam NFP 1 (simulation)* and *Practical Bessel beam NFP 1 (simulation)* are the focal patterns produced by the Bessel beam NFP 1 loaded respectively with theoretical values (Table 6.1) and practical values (Table 6.2). The graphs *Ideal Airy pattern NFP (simulation)* and *Practical Airy pattern NFP (simulation)* are the focal patterns produced by the Airy pattern NFP loaded respectively with theoretical values (Table 6.1) and practical values (Table 6.2).

desired properties, we also designed a second Bessel beam NFP: *Bessel beam NFP 2*. This plate produces a beam narrower than *Bessel beam NFP 1*. Specifically, $q = 7.6k$ of *Bessel beam NFP 1* has been increased to $q = 9.6k$ for *Bessel beam NFP 2*. The truncating Gaussian function is similar: $\sigma = 0.08\lambda$ for *Bessel beam NFP 2* compared to $\sigma = 0.0767\lambda$ for *Bessel beam NFP 1*. This slight change in σ was introduced to ensure that the required inductors and capacitors can be easily realized using available components. The performance of *Bessel beam NFP 2* is shown in Figure 6.7. *Bessel beam NFP 2* produces a beam with narrower beamwidth compared to that of *Bessel beam NFP 1*. However, its narrower beamwidth has been achieved at the cost of a shorter range: its sidelobes become comparable to the main lobe around $z = 40$ mm, while *Bessel beam NFP 1* could retain its shape up to $z = 60$ mm (see Figure 6.5).

The performance of *Bessel beam NFP 1* with frequency variation is studied in Figure 6.8. At lower frequencies, *Bessel beam NFP 1* produces a beam with FWHM slightly narrower than at the operating frequency. However, the pattern exhibits a larger variation of FWHM with axial distance. At higher frequencies, the plate
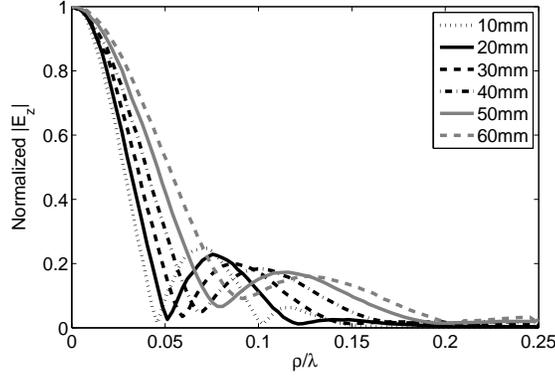
Figure 6.5: The normalized z-directed electric-field patterns produced by the *Bessel beam NFP 1* at various axial distances.
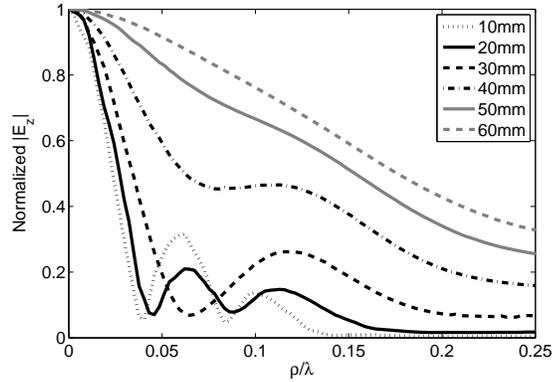
Figure 6.6: The normalized z-directed electric-field patterns produced by the *Airy pattern NFP* at various axial distance.

produces a beam with FWHM wider than at the operating frequency. This frequency response is similar to the one described in the previous chapter for the corrugated NFP.

Finally, the evanescent nature of the beams produced by the plates is examined in Figure 6.9. In this figure, the amplitudes of $E_z(\rho = 0, z)$ are normalized with respect to their values at $(\rho = 0, z = 0)$ and are shown on a dB scale. The decay rate of *Bessel beam NFP 1* is almost exponential. This is theoretically expected since an evanescent Bessel beam decays as $e^{-\sqrt{q^2-k^2}z}$. The decay rates for the *Airy pattern NFP* and the unloaded plate are also shown for comparison. The *Airy pattern NFP* exhibits a high decay rate close to the plate, which tapers off as the axial distance
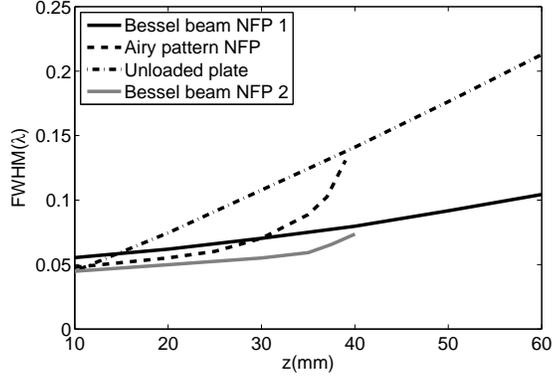
Figure 6.7: The FWHM of the simulated patterns produced by different devices as a function of axial distance.
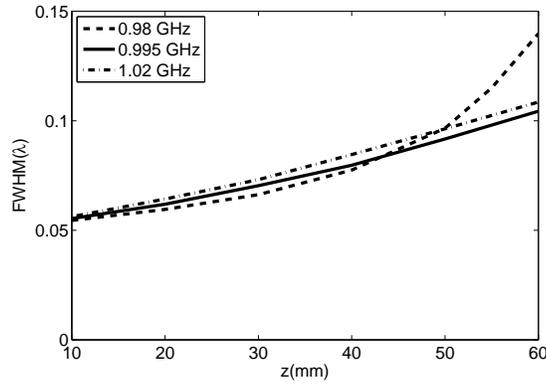
Figure 6.8: The simulated performance of the *Bessel beam NFP 1* with respect to frequency variation. The operating frequency is 0.995 GHz.

increases. This is expected since the propagating spectrum of the beam produced by this plate becomes dominant at larger distances, while the *Bessel beam NFP 1* essentially does not have a propagating spectrum. In the case of the unloaded plate, the evanescent spectrum is not enhanced due to lack of loading impedances. Thus, it exhibits a high decay rate close to the surface. *Bessel beam NFP 2* exhibits a higher decay rate compared to *Bessel beam NFP 1* since it has a larger q value. The decay rates shown in Figure 6.9 are consistent with those reported in the previous chapter for corrugated NFPs.

The full-wave simulation results reported in this section confirm the ability of planar NFPs to engineer the electromagnetic near field. In the next section, planar
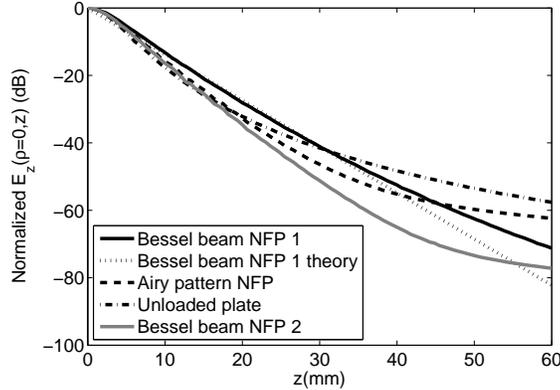
Figure 6.9: The simulated decay rate of the patterns produced by different devices as a function of axial distance.

NFPs are fabricated and measured. Their experimental performance is shown to be in agreement with simulation results. This will be the first experimental demonstration of evanescent Bessel beams at microwave frequencies.

6.4 Measurement Results

In this section, the planar NFPs designs pf the previous section are examined in experiment. The designed plates were fabricated using standard PCB technology. First, six annular slots were milled into a copper-clad 0.813 mm (32 mil) Rogers 4003C substrate. The annular slots dimensions were the same as the ones described in the previous section. A circle with radius $R = 42$ mm containing the annular slots was then cut out of the substrate. Next, the lumped components listed in Table 6.2 were placed on the annular slots using silver epoxy. Finally, the outer rim of the circular slab was short circuited using copper tape and a standard SMA connector was soldered to the plate. A planar NFP fabricated through this process is shown in Figure 6.10.

To test the fabricated plates, the setup shown in Figure 6.11 was used. In this setup, an open-ended semi-rigid coaxial cable (scanning probe) with an inner conductor of radius 0.46 mm and outer conductor of radius 1.8 mm was used to measure
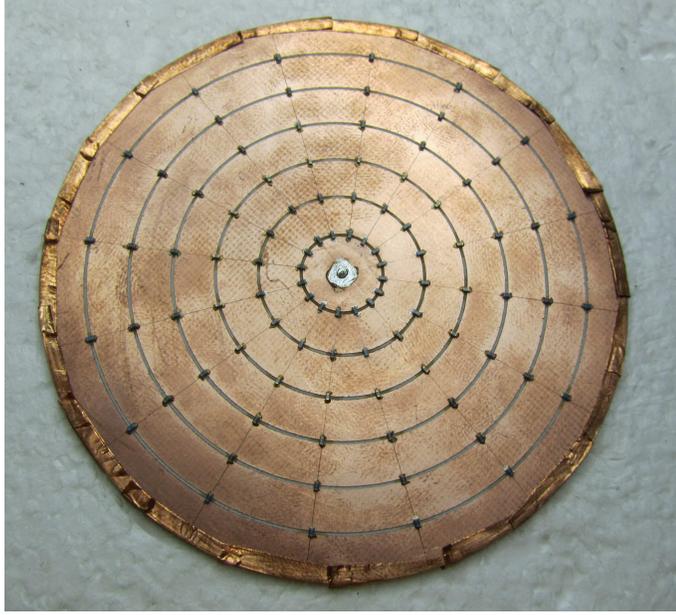
Figure 6.10: A fabricated planar NFP.

the z-directed electric-field patterns formed by the NFPs. To further enhance the received signal, the inner conductor of the semi-rigid probe was extended 4.5 mm. This probe was mounted to an xyz-translation stage to scan the near-field patterns generated by the plates. The fabricated plate was connected to port 1 of the vector network analyzer and its z-directed electric-field patterns were measured by the scanning probe connected to port 2 of the network analyzer. In the measurements, the distance between the outer conductor of the scanning probe and the surface of the plate was considered to be the axial distance, z. For example, the outer conductor of the probe was placed 20 mm away from the surface of the plate when measuring its focal pattern (focal plane is $L = 20$ mm).

The focal patterns measured in this manner are shown in Figure 6.12 (a)-(d) and labeled *Measurement*. Plotted in the same figures and labeled *Simulation*, are the simulated focal patterns using Ansys HFSS. The full-wave simulation captures the effect of the scanning probe. The measured and simulated focal patterns reported in Figure 6.12 exhibit close agreement, thereby verifying the design and operation of the
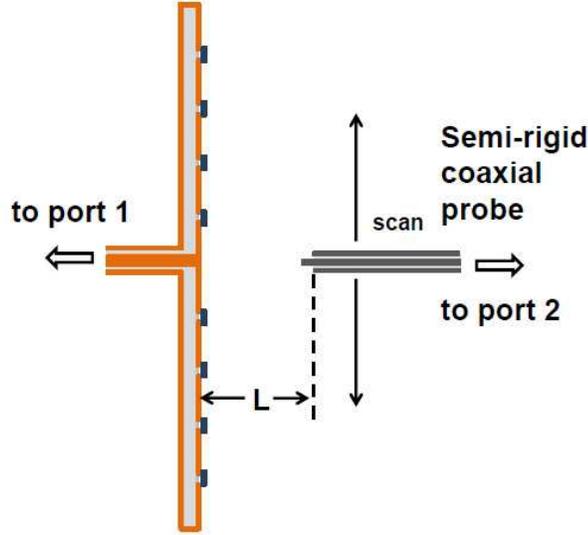
Figure 6.11: Setup for measuring the z-directed electric-field patterns formed by experimental plates.

planar NFPs.

It should be noted that the measurement results shown in Figure 6.12 are reported at 1.012 GHz for *Bessel beam NFP 1* (compared to 0.995 GHz for the simulation results), at 1.007 GHz for *Airy pattern NFP* (compared to 0.982 GHz for the simulation results), and at 1.026 GHz for the *Bessel beam NFP 2* (compared to 1.005 GHz for the simulation results). These slight frequency shifts can be attributed to the $2 - 5\%$ tolerances in the values of the lumped components and the substrate's dielectric constant.

The abilities of the designed NFPs to retain their shape and subwavelength beamwidth with distance varies. This difference can be observed experimentally by examining the beams radiated by the fabricated plates, as shown in Figure 6.13 (a)-(d). In these plots, the measured z-directed electric-field pattern at each axial cross-section, $(x, z = z')$, is normalized to its value at $(x = 0, z = z')$. Figure 6.13 (a) clearly illustrates the ability of *Bessel beam NFP 1* to create a beam with fixed beamwidth and shape. It is further highlighted by examining the beam emitted by the *Airy pattern NFP* (Figure 6.13 (b)). This plate produces a beam as narrow as *Bessel*
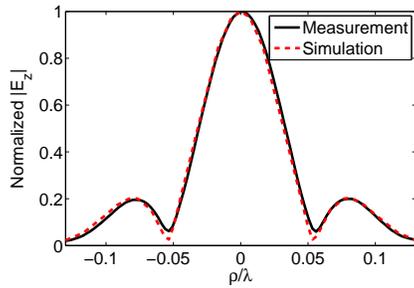
(a) Bessel beam NFP 1.
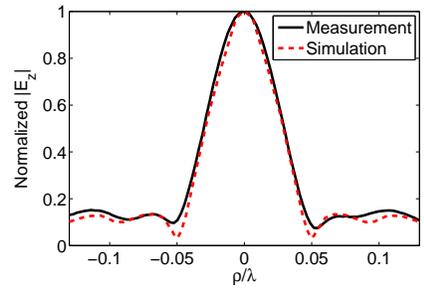
(b) Airy pattern NFP.
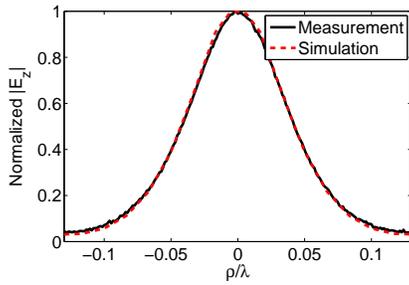
(c) Unloaded plate.
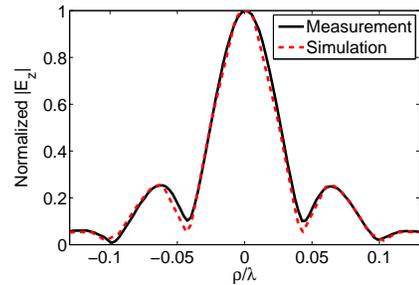
(d) Bessel beam NFP 2.

Figure 6.12: The measured and simulated focal patterns of various plates. The *Measurement* plots are the focal patterns measured using the setup shown in Figure 6.11. The *Simulation* plots are the focal patterns obtained from the full-wave simulation of the measurement setup with the scanning probe present. (a) Bessel beam NFP 1. (b) Airy pattern NFP. (c) Unloaded plate. (d) Bessel beam NFP 2.

(a) Bessel beam NFP 1

(b) Airy pattern NFP

(c) Unloaded plate
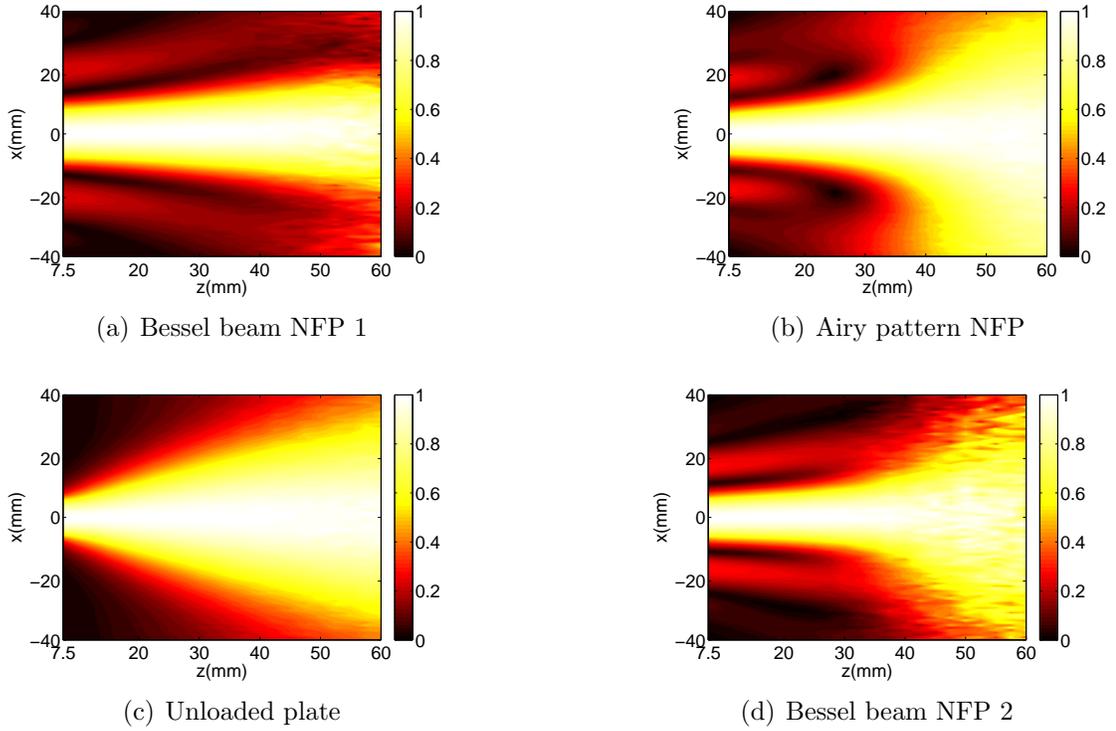
(d) Bessel beam NFP 2

Figure 6.13: The measured beam emitted from various plates. The measured field at each cross-section, $(x, z = z')$, is normalized to its value at $(x = 0, z = z')$. (a) Bessel beam NFP 1. (b) Airy pattern NFP. (c) Unloaded plate. (d) Bessel beam NFP 2.

beam NFP 1 at the focal plane ($z = 20$ mm), but its shape and beamwidth vary rapidly with increasing distance. A rapid variation of shape and beamwidth can also be observed for the unloaded plate shown in Figure 6.13 (c). Figure 6.13 (d) shows that *Bessel beam NFP 2* maintains a beamwidth narrower than the other structures. However, this narrow beamwidth has been obtained at the cost of a shorter range: up to $z = 40$ mm.

A more quantitative measure of *Bessel beam NFP 1*'s ability to retain its beamwidth is depicted in Figure 6.14, which plots its experimental FWHM vs. axial distance. For comparison purposes, we have also plotted the FWHM of the fabricated *Airy pattern NFP*, the unloaded plate, and *Bessel beam NFP 2*. The experimental *Bessel beam NFP 1* exhibits an almost constant FWHM while the FWHM of the *Airy pattern*
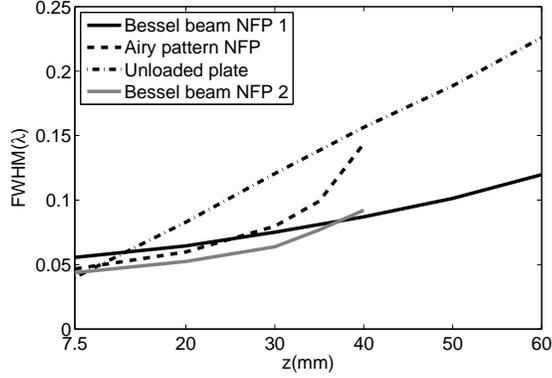
Figure 6.14: The measured FWHM of various devices as a function of the axial distance.

NFP and the unloaded plate changes dramatically with the axial distance. Specifically, the FWHM of the unloaded plate changes from 0.03997λ at $z = 7.5$ mm to 0.226λ at $z = 60$ mm: 5.65 times larger. Over the same distance, the FWHM of the experimental *Bessel beam NFP 1* changes from 0.05555λ to 0.1197λ: only 2.15 times larger. The measured FWHM of the *Airy pattern NFP* and *Bessel beam NFP 2* is plotted only up to $z = 40$ mm, since sidelobes became comparable to the mainlobe beyond $z = 40$ mm. The experimental FWHM graphs in Figure 6.14 exhibit the same trends as the full-wave simulation results of Figure 6.7.

The performance of the fabricated *Bessel beam NFP 1* with frequency variation is examined in Figure 6.15. At the frequency of operation, 1.012 GHz, the plate exhibits an almost constant FWHM. At higher frequencies, the plate exhibits a wider FWHM which varies more with distance than at the operating frequency. At lower frequencies, the plate produces a narrower beamwidth compared to the operating frequency. However, this narrow beamwidth is achieved at the cost of larger beamwidth variation with distance. The experimental frequency response shown in Figure 6.15 is consistent with the simulation results, shown in Figure 6.8 and, those reported for earlier experimental NFPs in previous chapters.

In the last part of our experiments, we examine the evanescent nature of the
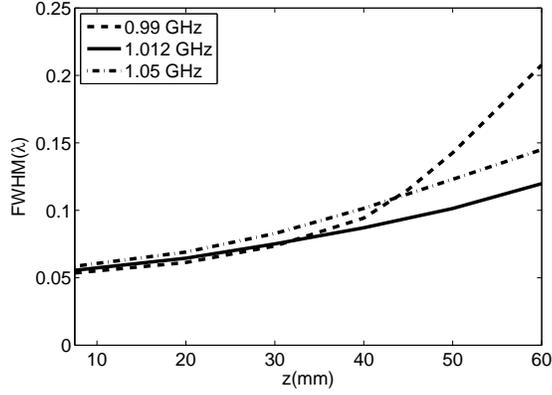
Figure 6.15: The measured frequency response of *Bessel beam NFP 1*. The frequency of operation is 1.012 GHz.
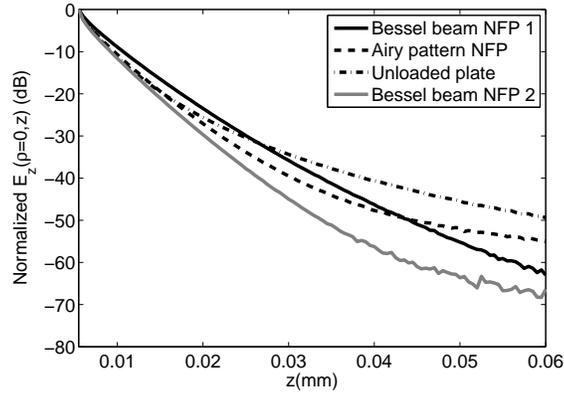
Figure 6.16: The measured decay rate of the patterns produced by different devices as a function of axial distance.

patterns generated by the fabricated structures. To do so, we measured the electric field at $\rho = 0$ as a function of axial distance z. The measurement results for each plate are normalized to their value at $z = 7.5$ mm and are shown on a dB scale in Figure 6.16. As expected, the experimental *Bessel beam NFP 1* exhibits an almost exponential decay rate, while the decay rate of *Airy pattern NFP* is large close to the plate and levels off as the axial distance increases. The decay rate of the unloaded plate is large close to the plate and tapers off with axial distance. *Bessel beam NFP 2* exhibits the largest decay rate since it produces the narrowest beamwidth.

6.5 Conclusion

Planar near-field plates (NFPs) were presented that can be fabricated using standard circuit board technology and produce desired subwavelength focal spots. The proposed planar plates consisted of annular slots on a grounded dielectric slab excited by a coaxial connector. The annular slots were loaded with lumped element impedances to produce desired subwavelength near-field patterns. A step-by-step procedure for designing these plates was outlined. Different NFPs were designed to highlight the ability of NFPs to produce various patterns: *Bessel beam NFP 1* and *2* were designed to generate evanescent Bessel beams with different beamwidths, while *Airy pattern NFP* was designed to generate an Airy pattern with the same beamwidth as *Bessel beam NFP 1*. The designed plates were compared to a plate with the same dimensions but no loading elements. The proposed structures were fabricated using printed circuit board technology. The fabricated plates were shown to produce near-field patterns in close agreement with simulation, thereby verifying the proposed design and operation. Furthermore, the Bessel beam NFPs produced experimental beams with nearly fixed shape and subwavelength beamwidth over near-field distances. Over the same distance, neither the beamwidth nor the shape were preserved by the *Airy pattern NFP* or the unloaded plate. Such planar NFPs will find applications in near-field imaging and probing systems, biomedical targeting devices, and high density data storage. Finally, development of planar NFPs addresses the three major issues of the initial NFP. Namely, planar NFPs can be (1) fed through a waveguide (coaxial connector), (2) generate a desired 2-D subwavelength focal spot, and (3) be easily fabricated and integrated with other hardware.

CHAPTER VII

Summary and Future Work

7.1 Summary

This thesis work arose from the need to produce subwavelength electromagnetic field confinement at extended distances. Such a capability could be crucial for applications such as high resolution imaging and probing, high density data storage, biomedical targeting devices, and wireless power transfer. However, efforts to engineer the electromagnetic near field have faced a major obstacle: the diffraction limit. Due to this limit, subwavelength focal patterns can only be achieved at extremely close distances

Near-field plates (NFPs) have been proposed as a novel solution for overcoming the diffraction limit. NFPs are non-periodically patterned surfaces or arrays which can produce prescribed near-field patterns that overcome the diffraction limit [13–16]. The first experimental NFP was reported in [15, 16] and consisted of an array of interdigitated capacitors. This plate focused microwave radiation emanating from a cylindrical source to a prescribed subwavelength focal pattern, thereby verifying the NFPs' ability to overcome the diffraction limit. However, the NFP configuration of [15, 16] had some major limitations, preventing it from practical use. Namely, it was excited by a line source while a waveguide excitation is preferred in many applications. In addition, it could only produce a one-dimensional focal pattern: a

line focus. Finally, its topology was not simple to integrate with other devices.

Over the course of this thesis, we have advanced the NFP concept through several stages, addressing a major issue in each stage. In the first stage, a fully analytical description of the NFP concept was introduced. This analytical treatment provided an intuitive understanding of NFP designs and their operation. Furthermore, the distinct features of NFPs and their similarities and differences with existing structures (such as metamaterial superlenses and antenna arrays) were explained.

In the next stage, a NFP that could be directly fed through a waveguide was developed. This plate was referred to as linearly corrugated NFP. It consisted of linear non-periodic corrugations that tailored the near field emitted by a central slit. A procedure for designing the plate was outlined. Its design and operation was then verified through simulation and experiment.

The linearly corrugated NFP could only produce a one dimensional subwavelength focus (focal line), while a two dimensional focus is desired in most applications. Also, it was excited using a slit which may be difficult to feed in practice. Therefore, concentrically corrugated NFPs were developed consisting of a coaxially-fed central aperture surrounded by periodically-spaced, concentric grooves. An experimental NFP was demonstrated that produced a prescribed subwavelength focal spot. It was used as a probe to image two closely spaced dipole sources. The NFP probe achieved images with significantly higher resolution compared to a conventional coaxial probe. These promising results were a major step toward establishing NFPs as devices that can achieve significant subwavelength resolution enhancement, opening new opportunities in near-field probing, biomedical targeting devices, and high density data storage systems.

To further highlight the unique ability of NFPs to sculpt the electromagnetic near field, we designed concentrically corrugated NFPs that can generate evanescent Bessel beams. Evanescent Bessel beams resist diffraction and retain their shape and

subwavelength beamwidth over a near-field distance. These beams have been difficult to produce in the past, and therefore, had not found their place in practice. The field tailoring capabilities of NFPs have opened new ways for practical, yet simple, methods for generating them.

While a concentrically corrugated NFP was capable of producing unprecedented near-field patterns, it was costly to fabricate. Furthermore, it could not be implemented using standard printed circuit board (PCB) technology. In many applications, a planar structure implemented using PCB techniques is preferred since it can be easily integrated with other electronics. To address this issue, we designed, fabricated, and experimentally demonstrated a planar NFP that can be fabricated using low-cost PCB technology. This work concluded the thesis by addressing the three major limitations of earlier NFP designs. The developed planar NFP was excited through a waveguide, could generate a desired 2-D subwavelength focus, and was simple to fabricate and integrate with other hardware.

7.2   Future Work

This work on NFPs has opened new opportunities, as well as new challenges. The most important challenge facing NFPs' practical use is their high reflection. As noted in Chapter 2, NFPs are reactive surfaces which might exhibit a pronounced impedance mismatch with free space. Therefore, they suffer from high reflection. For example consider the NFP of Chapter 2. This plate was excited by a line source and formed a subwavelength focal pattern. However, the majority of the electromagnetic field incident from the line source is reflected by the NFP, as shown Figure 2.10. In many practical applications, it is highly desired that the NFP funnels the field by the line source into the desired subwavelength focal pattern, resulting in a unidirectional near field.

For this purpose, we are revisiting the design procedure outlined in Chapter 2.

As in Chapters 3-6, the aperture current densities can be directly related to the focal pattern (without back propagation). Now let us assume that the amplitude of the subwavelength focal pattern is designed to be M times larger than the incident field from the line source. By adjusting the value of M, the field radiated by the NFP and the source are suppressed in the backward direction, but are enhanced in the forward direction. The phenomenon is similar to that observed in Yagi-Uda antennas [88], where the far-field is unidirectional. The NFP acts as a director element. As a result, we will refer to such a NFP that can produce a unidirectional near-field pattern as a "Yagi-Uda NFP". As an example, we have designed a NFP that produces a focal pattern with an amplitude 2.1 times larger than that the line source alone. The focal pattern produced by this NFP, as well as the pattern due to the line source, are shown in Figure 7.1. This new NFP produces a pattern with a significantly narrower beamwidth and higher amplitude compared to the line source alone. In Figure 7.2, a two-dimensional plot of the electric field produced by this new NFP is shown. Comparing Figure 7.2 to Figure 2.10, it is evident that the new NFP design does not suffer from high reflection. In fact, the subwavelength near-field pattern is unidirectional. This Yagi-Uda NFP exhibits promising features for high resolution probing and sensing, as well as wireless power transfer systems that can be explored in future work.

In Chapters 3-6, we used waveguides to feed NFPs. Naturally, a NFP with waveguide feed produces a unidirectional beam. Another advantage of a waveguide feed is that it can be impedance matched to the NFP. Due to the large impedance mismatch between the NFP and the waveguide, the impedance matching scheme will be highly sensitive to the input impedance of a NFP which is a function of its surroundings. This phenomenon can be used in future to develop a highly sensitive probing and sensing device of passive targets with subwavelength resolution. It should be emphasized that the required matching structure will be significantly narrowband and
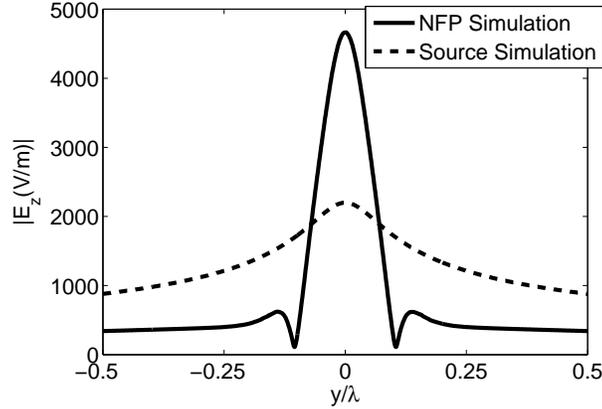
Figure 7.1: The focal pattern produced by a Yagi-Uda NFP. The pattern produced by the line source is also depicted for comparison.
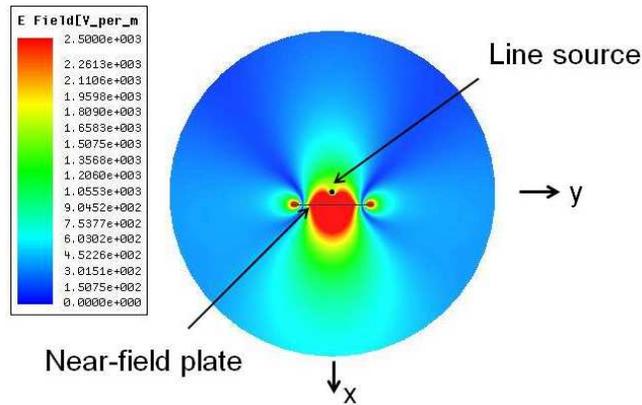
Figure 7.2: A two-dimensional plot of the magnitude of the electric field generated by Yagi-Uda NFP.

sensitive to losses. As a result, a more advanced matching structure compared to the double stub tuner used in Chapter 4 will be required [3].

While most of the work in this thesis has focused on NFPs at microwave frequencies, it should be noted that the NFP design and operation is frequency independent. As a result, NFPs can also be implemented at frequencies other than microwave frequencies. For example, nano-circuit elements proposed in [24] are good candidates for realizing optical NFPs. Nanostructured NFPs that allow one to stipulate the generated near-field pattern will be beneficial in many optical applications. For example, it could lead to near-field scanning optical microscopy (NSOM) with extended operat-

ing distances. It may also be used to develop lithography techniques with arbitrarily high resolutions. Similarly, it can be used to increase the density of data storage devices. As a result, research on optical NFPs constitutes a major future direction with numerous potential applications.

NFPs could also be used to improve targeting capabilities in medical devices such as those used in transcranial magnetic stimulation (TMS). Specifically, the use of NFPs may lead to increased electromagnetic field penetration, while maintaining a small stimulated volume within the brain. In TMS, an electric field is used to induce an electromotive force within brain tissue in order to excite neurons. The super-resolving power of a NFP could perhaps be used to precisely direct neuronal stimulation in TMS. Work on this subject has already begun [89, 90].

NFPs may also find use in wireless non-radiative power transfer systems. Specifically, megahertz receiving and transmitting devices based on NFPs could provide specific advantages over the resonant coils that have been used to date [4]. NFPs could be designed to provide magnetic field illumination to only certain areas of a confined environment, where electronic devices are typically placed. For example, tailored "energy hotspots" could be established on the top of desks or countertops using NFPs. NFPs may also radiate less energy to the far field than the single or multi-turn loops used in wireless non-radiative power transfer systems due to the oscillatory (in and out-of-phase) currents supported by them. Finally, tailoring the magnetic near-field illumination with transmitting and receiving devices based on NFPs may increase the range and efficiency of wireless power systems.

7.3 Publications

The work presented in this thesis has resulted in the following peer-reviewed journal and conference proceedings:

Refereed Journal Publications

M. F. Imani and A. Grbic, "Planar near-field plates", submitted to *IEEE Transactions on Antennas and Propagation*, January 2013.

M. F. Imani and A. Grbic, "Generating evanescent Bessel beams using near-field plates", *IEEE Transactions on Antenna and Propagation*, vol. 60, no.7, pages 3155-3164, Aug. 2012.

A. Grbic, R. Merlin, E. M. Thomas, M. F. Imani, "Near-field plates: Metamaterial surfaces / arrays for subwavelength focusing and probing", *Proceedings of the IEEE*, vol. 99, no. 10, pp 1806-1815, Oct 2011(invited to a Special Issue on Metamaterials: Fundamentals and Applications in the Microwave and Optical Regimes).

M. F. Imani and A. Grbic, "An experimental concentric near-field plate", *IEEE Transactions on Microwave Theory and Techniques*, vol. 58, no. 12, pages 3982-3988, December 2010.

M. F. Imani and A. Grbic, "An analytical investigation of near-field plates", *Metamaterials*, vol 4. pp. 104-111, Aug.-Sept. 2010 (Metamaterials 2009 Congress Special issue).

M. F. Imani and A. Grbic, "Tailoring near-field patterns with concentrically corrugated plates," *Applied Physics Letters*, vol. 95, pp. 111107, September 2009.

M. F. Imani and A. Grbic, "Near-field focusing with a corrugated surface", *IEEE Antennas and Wireless Propagation Letters*, vol. 8, 421-424 pages, May 2009.

Refereed Conference Publications/Presentation

M. F. Imani and A. Grbic, "Generating Bessel beams using an electrically-large annular slot," accepted for presentation at *IEEE International Symposium on Antennas and Propagation*, Lake Buena Vista, Florida, July 7-12, 2013.

A. Grbic, G. Gok, M. F. Imani, A.M. Patel, C. Pfeiffer, and M. Ettorre, "Metamaterial surfaces for near and far-field applications." *EuCAP 2013*, Gothenburg, Sweden, Apr 8-12, 2013. (Invited Paper).

M. F. Imani and A. Grbic, "Design of a planar near-field plate", *Antennas and*

Propagation Society International Symposium, Chicago, July, 2012.

M. F. Imani and A. Grbic, "A concentrically corrugated near-field plate", *Microwave Symposium Digest (MTT)*, 2010 IEEE MTT-S International, pp. 1648-1651, May, 2010.

A. Grbic and M. F. Imani, "Design and implementation of near-field plates", *International Conference on Advanced Electromagnetic Materials in Microwaves and Optics (Metamaterials '09)*, 3 pages, London, England, August 30 - September 4 2009 (invited).

M. F. Imani and A. Grbic, "Subwavelength focusing with a corrugated metallic plate", *Antennas and Propagation Society International Symposiu*m, Charleston, June, 2009.

M. F. Imani and A. Grbic, "An analytical investigation of near-field plates", *XXIX General Assembly of the International Union of Radio Science*, Chicago IL, Aug 7-16, 2008.

APPENDICES

APPENDIX A

Near Field of a Magnetic Current Frill

Analytical formulas for the electric and magnetic fields produced by a magnetic current frill in its near zone have been derived in [51]. These formulas are repeatedly used throughout this thesis. For convenience, they are summarized in this appendix. A magnetic current frill, M, is considered as shown in Figure A.1. The voltage across this frill is V. Its inner and outer radii are a and b. The z component of the electric field due to this magnetic frill is given by:

$$E_z(\rho, z) = \frac{V}{2\pi \ln(b/a)} \int_0^\pi \frac{e^{-jkr_a}}{r_a} - \frac{e^{-jkr_b}}{r_b} d\phi' \qquad (\text{A.1})$$

where k is the free space wavenumber, $r_a = \sqrt{z^2 + \rho^2 + a^2 - 2\rho a \cos(\phi')}$ and $r_b = \sqrt{z^2 + \rho^2 + b^2 - 2\rho b \cos(\phi')}$. In the equation above, (ρ, z, ϕ) refers to the observation point, while (ρ', z', ϕ') refers to a point on the magnetic current frill.

The ρ component of the electric field is given by:

$$E_\rho(\rho, z) = \frac{zV}{2\pi \ln(b/a)} \int_a^b (\alpha_1 K(P) + \alpha_2 E(P)) d\rho' - j\frac{Vk^5(b^2 - a^2)}{120 \ln(b/a)} \rho z \qquad (\text{A.2})$$

140
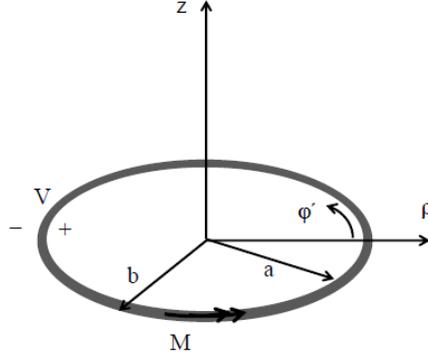
Figure A.1: Schematic of a magnetic current frill.

and its magnetic field is given by:

$$H_\phi(\rho, z) = \frac{\omega \epsilon k^3 (b^2 - a^2) V}{24 \ln(b/a)} \rho + \frac{j\omega \epsilon V}{2\pi \ln(b/a)} \int_a^b (\beta_1 K(P) + \beta_2 E(P)) d\rho' \qquad (A.3)$$

where ω is the angular frequency, ϵ is the free space permittivity, $K(P)$ is the complete elliptical integral of the first kind defined as $\int_0^{\pi/2} \frac{d\theta}{\sqrt{1 - P\sin(\theta)^2}}$, and $E(P)$ is the complete elliptical integral of the second kind defined as $\int_0^{\pi/2} \sqrt{1 - P\sin(\theta)^2} d\theta$. The other unknowns in (A.2) and (A.3) are defined as:

$$\alpha_1 = -\frac{4}{PR^3} + \frac{k^2}{R}\left(\frac{2}{P} - 1\right) - \frac{k^4 RQ}{6P}$$

$$\alpha_2 = \frac{4}{QR^3}\left(\frac{2}{P} - 1\right) - \frac{2k^2}{RP} - \frac{k^4 R}{12}\left(\frac{2}{P} - 1\right)$$

$$\beta_1 = \frac{2}{R}\left(\frac{2}{P} - 1\right) - \frac{2k^2 RQ}{3P}$$

$$\beta_2 = -\frac{4}{PR} + \frac{k^2 R}{3}\left(\frac{2}{P} - 1\right)$$

$$R = \sqrt{z^2 + (\rho + \rho')^2}$$

$$P = \frac{4\rho\rho'}{R^2}$$

$$Q = 1 - P \qquad (A.4)$$

141

BIBLIOGRAPHY

BIBLIOGRAPHY

[1] E. H. Synge, "A suggested method for extending the microscopic resolution into the ultramicroscopic region," *Philosophical Magazine*, vol. 6, pp. 356–362, 1928.

[2] E. A. Ash and G. Nicholls, "Super-resolution aperture scanning microscope," *Nature*, vol. 237, pp. 510–511, 1972.

[3] B. T. Rosner and D. W. van der Weide, "High-frequency near-field microscopy," *Review of Scientific Instruments*, vol. 73, no. 7, pp. 2505–2525, 2002. [Online]. Available: http://link.aip.org/link/?RSI/73/2505/1

[4] A. Kurs, A. Karalis, R. Moffatt, J.D. Joannopoulos, P. Fisher, and M. Soljacic, "Wireless power transfer via strongly coupled magnetic resonances," *Science*, vol. 317, pp. 83–86, July 2007.

[5] L. Hernandez-Garcia, S. Lee, and W. Grissom, "An approach to MRIbased dosimetry for transcranial magnetic stimulation," *NeuroImage*, vol. 36, pp. 1171–1178, July 2007.

[6] J. B. Pendry, "Negative refraction makes a perfect lens," *Physical Review Letters*, vol. 85, pp. 3966–3969, October 2000.

[7] R. A. Shelby, D. R. Smith, and S. Schultz, "Experimental verification of a negative index of refraction," *Science*, vol. 292, pp. 77–79, April 2001.

[8] A. Grbic and G.V. Eleftheriades, "Overcoming the diffraction limit with a planar left-handed transmission-line lens," *Physical Review Letters*, vol. 92, p. 117403, March 2004.

[9] D. Melville and R. Blaikie, "Super-resolution imaging through a planar silver layer," *Optics Express*, vol. 13, pp. 2127–2134, March 2005.

[10] N. Fang and H. Lee and C. Sun and X. Zhang, "Sub-diffraction-limited optical imaging with a silver superlens," *Science*, vol. 308, pp. 534–537, April 2005.

[11] F. Mesa, M.J. Freire, R. Marques, and J.D. Baena, "Three-dimensional super-resolution in metamaterial slab lenses: Experiment and theory," *Physical Review B*, vol. 72, p. 235117, December 2005.

[12] S. M. Rudolph and A. Grbic, "A broadband three-dimensionally isotropic negative-refractive-index medium," *Antennas and Propagation, IEEE Transactions on*, vol. 60, no. 8, pp. 3661–3669, Aug 2012.

[13] R. Merlin, "Radiationless electromagnetic interference: Evanescent-field lenses and perfect focusing," *Science*, vol. 317, pp. 927–929, July 2007.

[14] A. Grbic, R. Merlin, "Near-field focusing plates and their design," *IEEE Transactions on Antennas and Propagation*, vol. 56, pp. 3159–3165, October 2008.

[15] A. Grbic, L. Jiang, and R. Merlin, "Near-field plates: Subdiffraction focusing with patterned surfaces," *Science*, vol. 320, pp. 511–513, April 2008.

[16] ——, "Near-field focusing plates," *IEEE MTT-S International Microwave Symposium (WE1A-02)*, vol. WE1A-02, pp. 209–212, June 2008.

[17] M. F. Imani and A. Grbic, "An analytical investigation of near-field plates," *Metamaterials*, vol. 4, no. 2-3, pp. 104–111, 2010, metamaterials-2009 Congress in London. [Online]. Available: http://www.sciencedirect.com/science/article/B8G3N-4YMY78Y-3/2/c65a30d10b06a30fb31402d006b78378

[18] M. Imani and A. Grbic, "Subwavelength focusing with a corrugated metallic plate," *Antennas and Propagation Society International Symposium, 2009. AP-SURSI '09. IEEE*, pp. 1–4, jun. 2009.

[19] M. F. Imani and A. Grbic, "Tailoring near-field patterns with concentrically corrugated plates," *Applied Physics Letters*, vol. 95, p. 111107, September 2009.

[20] M. Imani and A. Grbic, "A concentrically corrugated near-field plate," *Microwave Symposium Digest (MTT), 2010 IEEE MTT-S International*, pp. 1648–1651, may. 2010.

[21] M. F. Imani and A. Grbic, "An experimental concentric near-field plate," *IEEE Transactions on Microwave Theory and Techniques*, vol. 58, no. 12, pp. 3982–3988, Dec. 2010.

[22] ——, "Generating evanescent bessel beams using near-field plates," *Antennas and Propagation, IEEE Transactions on*, vol. 60, no. 7, pp. 3155–3164, July 2012.

[23] E. Hecht, *Optics*. San Francisco: Addison Wesley, 2002.

[24] N. Engheta, A. Salandrino, and A. Alù, "Circuit elements at optical frequencies: Nanoinductors, nanocapacitors, and nanoresistors," *Phys. Rev. Lett.*, vol. 95, no. 9, p. 095504, Aug 2005.

[25] T. B. A Senior and J. L. Volakis, *Approximate boundary conditions in electromagnetics*. Edison, NJ: Institution of Engineering and Technology, 1995.

[26] C. A. Balanis, *Advanced Engineering Electromagnetics*. New York: John-Wiley and Sons, 1989.

[27] M. Abramovitz, I.A. Stegun, *Handbook of Mathematical Functions with Formulas, Graphs, and Mathematical Tables*. New York: Dover Publications, 1970.

[28] C. A. Balanis, *Antenna Theory: Analysis, and Design*, 2nd ed. New York: John-Wiley and Sons, 1996.

[29] R. C. Hansen, *Electrically Small, Superdirectivity, and Superconducting Antennas*. New York: John-Wiley and Sons, 2006.

[30] S. Bokhari, H. Smith, J. Mosig, J. Zurcher, and F. Gardiol, "Superdirective antenna array of printed parasitic elements," *Electronics Letters*, vol. 28, no. 14, pp. 1332 –1334, jul. 1992.

[31] A. D. Yaghjian, T. H. ODonnell, E. E. Altshuler, and S. R. Best, "Electrically small supergain end-fire arrays," *Radio Science*, vol. 43, RS3002, p. 13, 2008.

[32] V. Veremey, "Superdirective antennas with passive reflectors," *Antennas and Propagation Magazine, IEEE*, vol. 37, no. 2, pp. 16 –27, apr. 1995.

[33] T. W. Ebbesen, H. J. Lezec, H. F. Ghaemi, T. Thio1 and P. A. Wolff, "Extraordinary optical transmission through sub-wavelength hole arrays," *Nature*, vol. 391, pp. 667–669, February 1998.

[34] J. A. Porto, F. J. Garcia-Vidal, J. B. Pendry, "Transmission resonances on metallic gratings with very narrow slits," *Physical Review Letters*, vol. 83, pp. 2845–2848, October 1999.

[35] L. Martn-Moreno, F. J. Garca-Vidal, H. J. Lezec, K. M. Pellerin, T. Thio, J. B. Pendry, and T.W. Ebbesen, "Theory of extraordinary optical transmission through subwavelength hole arrays," *Physical Review Letters*, vol. 86, pp. 1114–1117, February 2001.

[36] H. J. Lezec, A. Degiron, E. Devaux, R. A. Linke, L. Martin-Moreno, F. J. Garcia-Vidal, T. W. Ebbesen, "Beaming light from a subwavelength aperture," *Science*, vol. 297, pp. 820–822, August 2002.

[37] L. Martn-Moreno, F. J. Garca-Vidal, H. J. Lezec, A. Degiron, and T. W. Ebbesen, "Theory of highly directional emission from a single subwavelength aperture surrounded by surface corrugations," *Physical Review Letters*, vol. 90, p. 167401, April 2003.

[38] F. J. Garcia-Vidal, H. J. Lezec, T. W. Ebbesen, and L. Martin-Moreno, "Multiple paths to enhance optical transmission through a single subwavelength slit," *Physical Review Letters*, vol. 90, p. 213901, May 2003.

[39] F. J. Garcia-Vidal, L. Martin-Moreno, H. J. Lezec, and T. W. Ebbesen, "Focusing light with a single subwavelength aperture flanked by surface corrugations," *Applied Physics Letters*, vol. 83, pp. 4500–4502, December 2003.

[40] M. J. Lockyear, A. P. Hibbins, J. R. Sambles, C. R. Lawrence, "Surface-topography-induced enhanced transmission and directivity of microwave radiation through a subwavelength circular metal aperture," *Applied Physics Letters*, vol. 84, pp. 2040–2042, March 2004.

[41] S. S. Akarca-Biyikli, I. Bulu, E. Ozbay, "Enhanced transmission of microwave radiation in one-dimensional metallic gratings with subwavelength aperture," *Applied Physics Letters*, vol. 85, pp. 1098–1100, August 2004.

[42] D.R. Jackson, A.A. Oliner, T. Zhao, and J.T. Williams, "The beaming of light at broadside through a subwavelength hole: Leaky-wave model and open stopband effect," *Radio Science*, vol. 40, p. RS6S10, 2005.

[43] J. B. Pendry, L. Martin-Moreno, F. J. Garcia-Vidal, "Mimicking surface plasmons with structured surfaces," *Science*, vol. 305, pp. 847–848, August 2004.

[44] X. Luo, C. Wang. C. Du, H. Shi, H. Gao, J. Ma, Y. Fu, H. Li, "Beaming light from a subwavelength slit surrounded by an array of grooves with different depth," *Proc. SPIE*, vol. 5927, 2005.

[45] S. L. R. A. F. Peterson and R. Mittra, *Computational Methods for Electromagnetics.* Piscataway, NJ: IEEE Press, 1998.

[46] D. M. Pozar, *Microwave Engineering.* New York: John Wiley and Sons, Inc, 2005.

[47] P. F. Goldsmith, *Quasioptical Systems: Gaussian Beam Quasioptical Propagation and Applications.* Piscataway, NJ: IEEE Press, 1998.

[48] S. Rudolph and A. Grbic, "Broadband, low-loss negative-permeability and negative-index media for free-space applications," *Microwave Symposium Digest, 2009. MTT '09. IEEE MTT-S International*, pp. 113 –116, jun. 2009.

[49] D. Banerjee, J. Lee, E. M. Dede, and H. Iizuka, "Kilohertz magnetic field focusing in a pair of metallic periodic-ladder structures," *Applied Physics Letters*, vol. 99, no. 9, p. 093501, 2011.

[50] E. M. Dede, J. Lee, Y. Guo, L. Q. Zhou, M. Zhang, and D. Banerjee, "Kilohertz magnetic field focusing and force enhancement using a metallic loop array," *Applied Physics Letters*, vol. 101, no. 2, p. 023506, 2012.

[51] A. Sakitani, S. Egashira, "Simplified expressions for the near fields of a magnetic frill current," *IEEE Transactions on Antennas and Propagation*, vol. AP-34, p. 1059, 1986.

[52] J. Durnin, "Exact solutions for nondiffracting beams. i. the scalar theory," *J. Opt. Soc. Am. A*, vol. 4, no. 4, pp. 651–654, Apr 1987.

[53] J. Durnin, J. J. Miceli, and J. H. Eberly, "Diffraction-free beams," *Phys. Rev. Lett.*, vol. 58, no. 15, pp. 1499–1501, Apr 1987.

[54] A. J. Cox and D. C. Dibble, "Nondiffracting beam from a spatially filtered fabry-perot resonator," *J. Opt. Soc. Am. A*, vol. 9, no. 2, pp. 282–286, Feb 1992.

[55] A. Vasara, J. Turunen, and A. T. Friberg, "Realization of general nondiffracting beams with computer-generated holograms," *J. Opt. Soc. Am. A*, vol. 6, no. 11, pp. 1748–1754, Nov 1989.

[56] R. M. Herman and T. A. Wiggins, "Production and uses of diffractionless beams," *J. Opt. Soc. Am. A*, vol. 8, no. 6, pp. 932–942, Jun 1991.

[57] M. Lapointe, "Review of non-diffracting bessel beam experiments," *Optics and Laser Technology*, vol. 24, no. 6, pp. 315–321, 1992.

[58] W. B. Williams and J. B. Pendry, "Generating bessel beams by use of localized modes," *J. Opt. Soc. Am. A*, vol. 22, no. 5, pp. 992–997, May 2005.

[59] T. Grosjean, D. Courjan, and D. V. Labeke, "Microscopy with self-reconstructing beams," *Journal of Microscopy*, vol. 210, pp. 319–323, 2003.

[60] F. G. Mitri, "Arbitrary scattering of an electromagnetic zero-order bessel beam by a dielectric sphere," *Optics letter*, vol. 36, pp. 766–768, 2011.

[61] Z. Bouchal, J. Wagner, and M. Chlup, "Self-reconstruction of a distorted non-diffracting beam," *Optics Communications*, vol. 151, no. 4-6, pp. 207 – 211, 1998.

[62] F. O. Fahrbach, P. Simon, and A. Rohrbach, "Microscopy with self-reconstructing beams," *Nature Photonics*, vol. 4, pp. 780–785, 2010.

[63] Z. Bouchal, R. Horak, and J. Wagner, "Propagation-invariant electromagnetic fields: theory and experiment," *Journal of Modern Optics*, vol. 43, no. 9, pp. 1905–1920, 1996.

[64] T. Cimr, V. Kollrov, Z. Bouchal, and P. Zemnek, "Sub-micron particle organization by self-imaging of non-diffracting beams," *New Journal of Physics*, vol. 8, p. 43, 2006.

[65] S. Ruschin and A. Leizer, "Evanescent bessel beams," *J. Opt. Soc. Am. A*, vol. 15, no. 5, pp. 1139–1143, May 1998.

[66] Q. Zhan, "Evanescent bessel beam generation via surface plasmon resonance excitation by a radially polarized beam," *Opt. Lett.*, vol. 31, no. 11, pp. 1726–1728, Jun 2006.

[67] W. Chen and Q. Zhan, "Realization of an evanescent bessel beam via surface plasmon interference excited by a radially polarized beam," *Opt. Lett.*, vol. 34, no. 6, pp. 722–724, Mar 2009.

[68] G. Rui, Y. Lu, P. Wang, H. Ming, and Q. Zhan, "Evanescent bessel beam generation through filtering highly focused cylindrical vector beams with a defect mode one-dimensional photonic crystal," *Optics Communications*, vol. 283, no. 10, pp. 2272 – 2276, 2010.

[69] ——, "Generation of enhanced evanescent bessel beam using band-edge resonance," *Journal of Applied Physics*, vol. 108, no. 7, p. 074304, 2010.

[70] M. Salem, A. Kamel, and E. Niver, "Microwave bessel beams generation using guided modes," *IEEE Transactions on Antennas and Propagation*, vol. 59, no. 6, pp. 2241 –2247, June 2011.

[71] Y. Matsuoka, Y. Kizuka, and T. Inoue, "The characteristics of laser micro drilling using a bessel beam," *Applied Physics A*, vol. 84, pp. 423–430, 2006.

[72] M. K. Bhuyan, F. Courvoisier, P. A. Lacourt, M. Jacquot, R. Salut, L. Furfaro, and J. M. Dudley, "High aspect ratio nanochannel machining using single shot femtosecond bessel beams," *Applied Physics Letters*, vol. 97, no. 8, p. 081102, 2010.

[73] A. Sommerfeld, "ber die ausbreitung der wellen in der drahtlosen telegraphie," *Ann. Physik*, vol. 28, p. 665736, 1909.

[74] K. A. Norton, "The propagation of radio waves over the surface of the earth and in the upper atmosphere: Part i," *Proc. IRE*, vol. 24, no. 10, p. 13671387, Oct 1936.

[75] ——, "The propagation of radio waves over the surface of the earth and in the upper atmosphere: Part ii," *Proc. IRE*, vol. 25, no. 9, p. 12031236, Sept 1937.

[76] A. Banos, *Dipole Radiation in the Presence of a Conducting Half-Space.* Pergamon, 1966.

[77] W. Fernando and H. Barlow, "An investigation of the properties of radial cylindrical surface waves launched over flat reactive surfaces," *Proceedings of the IEE - Part B: Radio and Electronic Engineering*, vol. 103, no. 9, pp. 307 –318, May 1956.

[78] H. E. M. Barlow and A. L. Cullen, "Surface waves," *Proceedings I.E.E.*, vol. 100, Part III, no. 1482 R, p. 329, April 1953.

[79] D. Brick, "The radiation of a hertzian dipole over a coated conductor," *Proceedings of the IEE - Part C: Monographs*, vol. 102, no. 1, pp. 104 –121, March 1955.

[80] ——, "The excitation of surface waves by a vertical antenna," *Proceedings of the IRE*, vol. 43, no. 6, pp. 721 –727, June 1955.

[81] Y. T. Lo, "Electromagnetic field of a dipole source above a grounded dielectric slab," *Journal of Applied Physics*, vol. 25, no. 6, pp. 733 –740, Jun 1954.

[82] K. Sarabandi, M. Casciato, and I.-S. Koh, "Efficient calculation of the fields of a dipole radiating above an impedance surface," *Antennas and Propagation, IEEE Transactions on*, vol. 50, no. 9, pp. 1222 – 1235, Sep 2002.

[83] W. C. Chew, *Waves and Fields in Inhomogeneous Media*. Van Nostrand, 1990.

[84] G. M. Lerman, A. Yanai, and U. Levy, "Demonstration of nanofocusing by the use of plasmonic lens illuminated with radially polarized light," *Nano Letters*, vol. 9, no. 5, pp. 2139–2143, 2009.

[85] T. Cheng, D. Lin, J. Yeh, J. Liu, C. Yeh, and C. Lee, "Propagation characteristics of silver and tungsten subwavelength annular aperture generated sub-micron non-diffraction beams," *Optics Express*, vol. 17, pp. 5330–5339, 2009.

[86] M. Ettorre, S. Rudolph, and A. Grbic, "Generation of propagating bessel beams using leaky-wave modes: Experimental validation," *Antennas and Propagation, IEEE Transactions on*, vol. 60, no. 6, pp. 2645 –2653, june 2012.

[87] A. Grbic, R. Merlin, E. M. Thomas, and M. F. Imani, "Near-field plates: Metamaterial surfaces/arrays for subwavelength focusing and probing," *Proceedings of the IEEE*, vol. PP, no. 99, pp. 1 –10, 2011.

[88] H. Yagi, "Beam transmission of ultra short waves," *Proceedings of the Institute of Radio Engineers*, vol. 16, no. 6, pp. 715–740, June.

[89] L. Gomez, L. Hernandez, A. Grbic, and E. Michielssen, "A simulation of focal brain stimulation using metamaterial lenses," in *Antennas and Propagation Society International Symposium (APSURSI), 2010 IEEE*, 2010, pp. 1–4.

[90] L. Hernandez-Garcia, T. Hall, L.Gomez, and E. Michielssen, "A numerically optimized active shield for improved transcranial magnetic stimulation targeting," *Brain Stimulation*, vol. 3, no. 4, pp. 218 – 225, 2010.